Matrin3 is a Critical Splice Factor
for Cardiac and Lymphvascular Development

Inaugural Dissertation

zur Erlangung des akademischen Grades

Doktor der Naturwissenschaften

doctor rerum naturalium (Dr. rer. nat.)

Angefertigt am Max-Planck-Institut für Herz- und Lungenforschung, Bad Nauheim

Vorgelegt beim Fachbereich 08 Biologie und Chemie der Justus-Liebig-Universität, Gießen

von

M.Sc. Silke Kreher

2022

Arbeitstitel

Investigating the Role of Matrin3 in Cardiovascular Development and Disease

Prüfer

Erstgutachter: Prof. Dr. Dr. Thomas Braun

Zweitgutachterin: Prof. Dr. Sandra Hake

Weitere Prüfer: Prof. Dr. Thomas Böttger, Prof. Dr. Lienhard Schmitz

Dekan

Prof. Dr. Thomas Wilke

Tag der Disputation

06.12.2022

_____

Eidesstattliche Erklärung

Ich erkläre: Ich habe die vorgelegte Dissertation selbstständig und ohne unerlaubte fremde Hilfe und nur mit den Hilfen angefertigt, die ich in der Dissertation angegeben habe. Alle Textstellen, die wörtlich oder sinngemäß aus veröffentlichten Schriften entnommen sind, und alle Angaben, die auf mündlichen Auskünften beruhen, sind als solche kenntlich gemacht. Ich stimme einer evtl. Überprüfung meiner Dissertation durch eine Antiplagiat-Software zu. Bei den von mir durchgeführten und in der Dissertation erwähnten Untersuchungen habe ich die Grundsätze guter wissenschaftlicher Praxis, wie sie in der „Satzung der Justus-Liebig-Universität Gießen zur Sicherung guter wissenschaftlicher Praxis" niedergelegt sind, eingehalten.

Gießen, den _____

Silke Kreher

Danksagung

Ich möchte mich zu aller erst herzlich bei meinem Doktorvater Prof. Dr. Dr. Thomas Braun bedanken, der mir die Möglichkeit gab, meine Doktorarbeit in seinem Department anzufertigen.

Zudem danke ich meiner Zweitgutachterin Prof. Dr. Hake und den weiteren Prüfern dieser Dissertation Prof. Dr. Böttger und Prof. Dr. Schmitz.

Mein Dank gilt zudem meinem direkten Supervisor Dr. Andre Schneider für zahlreiche, lebhafte Diskussionen. Meinem TAC Mitglied Dr. Oliver Rossbach danke ich für die externe Betreuung während meiner Zeit in der IMPRS.

Mein besonderer Dank gilt zudem allen technischen Assistent*innen und Kolleg*innen der Arbeitsgruppe Braun und den Servicegruppen am MPI in Bad Nauheim – ohne den regulären Austausch wäre diese Arbeit nicht möglich gewesen. Marion Wiesnet gilt es namentlich zu erwähnen und danken - nicht nur für den fachlichen und privaten Austausch, sondern auch für das Stricken der zahlreichen „Mützen".

Danke zudem an die Mitarbeiter*innen des Tierstalls des MPIs, die meine Mäuse versorgten. Und um einen Buchtitel zu zitieren: „Thank you, Mouse!"

Darüber hinaus gilt mein Dank allen Kollaborationspartnern, welche zu dieser Arbeit betragen konnten - insbesondere den Arbeitsgruppenleitern Dr. Kathi Zarnack und Dr. Michael Gotthardt. Dem DHZK möchte ich für die zeitweise Förderung meiner Arbeit danken.

Prof. Dr. Kerstin Wilhelm-Jüngling und Dr. Mareike Pötsch möchte ich für die Einarbeitung in zahlreiche Methoden und regen Erfahrungsaustausch, sowie viele schöne, private Erinnerungen danken.

Zu guter Letzt geht mein größter und besonderer Dank an meine Mama, meine Familie und Lieblingsmenschen, die mich während der letzten Jahre begleitet und unterstützt haben. Ohne euch wäre diese Arbeit nicht möglich gewesen. Danke und auf zu neuen Abenteuern.

For Those Who Can't Be Here.

Content

List of Figures

List of Tables

Summary in German – Zusammenfassung auf Deutsch

RNA-bindende Proteine regulieren posttranskriptionelle Prozesse wie alternatives Spleißen und tragen damit zur Proteomdiversität bei. Fehlerhaftes, kardiales alternatives mRNA-Spleißen kann zu Herzinsuffizienz beim Menschen führen, wobei das Zusammenspiel der involvierten RNA-bindenden Proteine bisher nicht vollständig aufgeklärt ist. Bisherige Studien befassten sich überwiegend mit der Funktion des Muskel-spezifischen RNA-bindenden Proteins RBM20 als essenziellem Spleißfaktor in Herzmuskelzellen. Die vorliegende Arbeit identifiziert das zu RBM20 paraloge MATR3 (Matrin3) als weiteren, kritischen alternativen Spleißregulator des Herzens, da sich der Verlust von MATR3 aufgrund von dilatativen Kardiomyopathie in einer Herzinsuffizienz manifestiert. MATR3 bindet an herzspezifische Transkripte und reguliert alternatives prä-mRNA-Spleißen einiger dieser RNAs. Der Verlust von MATR3 *in vivo* führt zum Fehlspleißen oder reduzierten Konzentrationen physiologisch wichtiger Zieltranskripte. Interessanterweise teilen sich hierbei die beiden Paraloge RBM20 und MATR3 eine Gruppe von Transkripten mit herzspezifischen Isoformen wie Titin, Cypher und Calcium/Calmodulin-abhängige Proteinkinasen, was überschneidende Funktionen in Bezug auf alternatives Spleißen offenbart. Titin stellt dabei ein wichtiges prä-mRNA-Target von sowohl MATR3 als auch RBM20 dar, wobei der Verlust von MATR3 zu einer Verschiebung des Verhältnisses der Titinvarianten N2BA und N2B führt. Im Gegensatz hierzu induziert der Verlust von RBM20 die Bildung einer größeren, bereits bekannten Titin-Variante. Die vorliegende Studie zeigt zudem durch den Einsatz einer Kombination von konstitutivem und gewebespezifischen Knockout-Mausmodellen, dass MATR3 für die Lymphangiogenese wichtig ist. Lymphgefäße reagieren mit Hyperplasie auf den Verlust von MATR3 in der Zellkultur und *in vivo*, wohingegen Blutgefäße ihr Netzwerk und ihre Funktion aufrechterhalten. Als Folge des Verlustes von MATR3 in Mäusen entwickeln sich Lymphödemen und es zeigt sich eine embryonale Letalität aufgrund von erweiterten, dysfunktionalen dermalen Lymphgefäßen und jugulären Lymphsäcken. Neben der gewebsspezifischen Funktion von MATR3 als Spleißfaktor zeigt diese Studie erstmalig eine heterogene, zelldichteabhängige Expression von Matrin3 in Herzmuskel- und Endothelzellen. Da Veränderungen der Zelldichte mit der Lokalisierung von YAP sowie dem Vorkommen von MATR3-Protein korrelieren, weisen die Resultate auf MATR3 als ein potentiell neues, YAP nachgeschaltetes Zielgen hin. Dies wird auch durch die Beobachtung gestützt, dass eine erhöhte konstitutiv-kernständige YAP-Aktivität in Herzmuskelzellen neben der Expression von bekannten YAP-Zielgenen die Expression von Matrin3 erhöht. Zusammengefasst demonstriert die vorliegende Studie eine wesentliche Rolle von MATR3-vermitteltem alternativen Spleißens für das Herz-Kreislauf-System, da ein Verlust zu pathophysiologischen Veränderungen des Herzes und von Lymphgefäßen führt. Zukünftig

sollen diese Beobachtungen mit Krankheitsbildern wie dilatativer Kardiomyopathie oder primärem Lymphödem verknüpft werden.

Summary in English

RNA binding proteins regulate post-transcriptional processes such as alternative splicing, thereby contributing to the overall proteome diversity. Cardiac alternative mRNA splicing is involved in the pathophysiology of heart failure in humans; however, the complexity of involved RNA-binding proteins remains unsolved. In the heart, extensive research revealed the function of the muscle-restricted RNA-binding protein RBM20 as an essential cardiac splice factor. In this study, the broadly expressed RBM20-paralogue MATR3 (Matrin3) was identified as an alternative splicing regulator, critical for cardiac function. Loss of MATR3 loss results in heart failure due to dilated cardiomyopathy, most likely due to defects in alternative splicing of cardiac-specific transcripts (identified by the TRIBE method). Absence of MATR3 results in mis-splicing or downregulation of physiological important target transcripts *in vivo*. Remarkably, paralogous RBM20 and MATR3 share a subset of commonly spliced transcripts and even local splice sites within targets such as Titin, Cypher, and Calcium/Calmodulin-dependent Protein Kinases, revealing partial overlapping functions in respect to alternative splicing in cardiomyocytes. Titin was found to be a major pre-mRNA target of MATR3 and RBM20, since the loss of MATR3 leads to an elevated N2BA/N2B ratio, whereas loss of RBM20 results in a giant Titin variant as described previously. Furthermore, this study demonstrates that MATR3 is important for lymphangiogenesis, since lymphatic vessels become hyperplastic in response to loss of MATR3 in cell culture and *in vivo*, whereas blood vessels maintain their network and function. Consequently, constitutive and tissue-specific Matrin3 knockout mice models develop lymphedema and embryonic lethality due to dilated, malfunctional dermal lymphatic vessels and jugular lymph sacs. In addition to the function of MATR3 as a splicing factor within cardiomyocytes and the lymphatic endothelium, we shed light on the heterogeneous, cell-density-dependent expression and protein abundance of Matrin3 in cardiac and endothelial cells. Density-dependent changes in the localization of YAP correlate with the abundance of MATR3 protein. In addition, increased constitutive nuclear YAP activity in cardiomyocytes enhances Matr3 expression with concomitant upregulation of canonical targets, identifying MATR3 as a potential new downstream target of YAP. In conclusion, our results elucidate the essential role of MATR3-mediated alternative splicing for the cardiovascular system, since loss of MATR3 promotes pathophysiological alterations of the lymphatic network and the heart. In the future, we aim to link our current results with human disease conditions such as dilated cardiomyopathy and primary lymphedema.

Introduction

Post-transcriptional mechanisms of pre-mRNA processing

The central dogma of molecular biology is the directional flow of genetic information from DNA to RNA (via transcription) and from RNA to protein (via translation). However, pre-mRNA processing is a key intermediate step between transcription and translation, comprising multiple processes such as 5′-capping, pre-mRNA splicing, and 3′-polyadenylation. The regulation of RNA processing is mediated by RNA-binding proteins (RBPs) [1], which can bind to single- or double-stranded RNA via RNA-binding domains such as RNA recognition motifs (RRMs) [2] or zinc finger domains (ZnF) [3]. Thereupon, RBPs assemble with target RNAs forming dynamic complexes named ribonucleoproteins (RNPs).

Within the listed processes, pre-mRNA splicing is crucial for protein diversity and comprises two modes: constitutive and alternative splicing. Constitutive pre-mRNA splicing is the post-transcriptional process in which non-coding segments (introns) are spliced out from the pre-mRNA, followed by the joining of exons to form mature mRNA (**Figure 1**A). The core spliceosome is a dynamic multi-subunit ribonucleoprotein complex that catalyzes splicing in a two-step reaction and is composed of approximately 100 proteins [4]–[6]. The recognition of the pre-mRNA by the spliceosome requires three conserved regions in the intron: the 5′ splice site (5′ss), the 3′ splice site (3′ss), and the intronic branch-point sequence. Cis-acting splicing regulatory elements (SREs) recruit trans-acting factors to either promote or inhibit the use of adjacent splice sites [7]. These SREs are conventionally classified as exonic splicing enhancers (ESEs) or silencers (ESSs), as well as intronic splicing silencers (ISSs) or enhancers (ISEs). Here, splicing enhancer sequences promote the recognition and usage of a particular splice site, whereas splicing silencers restrict it.

The differential usage of splice sites in pre-mRNAs can result in the production of structurally and functionally distinct RNA isoforms in a process known as alternative splicing (AS, **Figure 1**B-F). In contrast to constitutive splicing, AS requires cis-regulatory elements located in the pre-mRNA and corresponding trans-acting factors displaying dynamic and tissue-specific expression profiles. Different types of events can occur during AS, for example, cassette exon inclusion or exon skipping (**Figure 1**B), which represent the most common forms of differential splicing. In addition, AS events include alternative 3′ and 5′ splice sites (**Figure 1**C+D), mutually exclusive exons (**Figure 1**E), intron retention (**Figure 1**F), and the usage of alternative polyA sites. Furthermore, circular RNAs (circRNAs) can be formed through back-splicing of an upstream splice acceptor to a downstream splice donor [8]. During AS, alternative splicing factors are spatiotemporally recruited to restricted regions of the pre-mRNA, thereby regulating the cell-type-specific or developmental-stage-specific AS network.

Moreover, the combination of alternative splice events adds another layer of complexity to modulate transcriptome diversity.
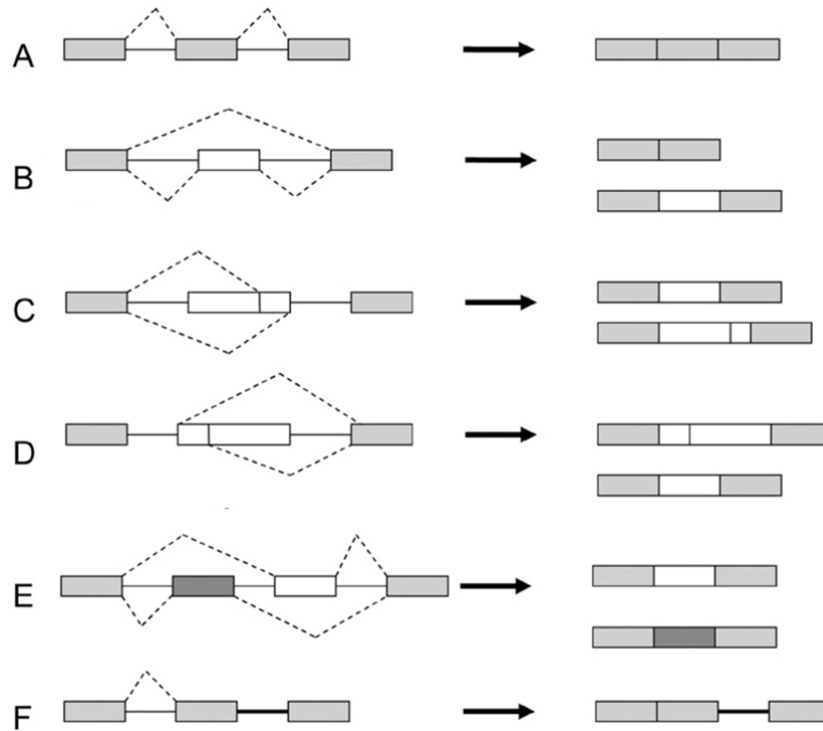
Figure 1 Types of constitutive and alternative pre-mRNA splicing

Schemes of **A** constitutive splicing, **B** cassette alternative exon, **C** alternative 3′ and **D** alternative 5′ splice site, **E** mutually exclusive exons and **F** intron retention. Grey box: exon, white box: intron, dashed lines: splicing event. Adapted from: [9].

In addition to splicing, RNA editing represents another important form of post-transcriptional modification, increasing the diversity of transcripts. The most frequent and common form of RNA editing is mediated by adenosine deaminases (ADARs), which deaminate adenosine (A) residues to inosine (I) [10]. Thereby, ADARs change the information of transcripts in respect to splicing [11], RNA stability, and translation [12], [13]. Due to AS and RNA editing, one single coding gene can give rise to multiple, functionally diverse protein isoforms, thereby increasing the complexity and diversity of the proteome [14], [15].

Detecting alternative splicing events from RNA sequencing data

Next generation sequencing enables the identification of annotated as well as novel isoforms (generated by AS) either by generating full-length transcripts or by aligning short reads. Methods to generate long-read, full-length transcript sequences comprise PacBio Isoform Sequencing (Iso-Seq, reviewed in [16], [17]) and Oxford Nanopore Technologies (ONT, reviewed in [17]) that both circumvent the assembly of short single reads. In the case of read alignment, common bioinformatics tools are DEXSeq [18] and derivates such as MAJIQ [19], enabling to capture local splice variation (LSV) of multiple replicates for different conditions.

LSVs are defined as either single-source (5′ split) or single-target (3′ join, **Figure 2**A) and thereby capture (non-)classical binary splicing events (**Figure 2**B) and complex events (defined by two or more junctions, **Figure 2**C), reflecting the complexity of ASE [20]. In this study, we applied conventional RNA-Seq and read alignment followed by bioinformatic analysis with MAJIQ combined with Voila to identify ASE in the different conditions. MAJIQ uses .bam files from RNA-Seq with transcriptome annotation to define LSV (**Figure 2**D) and thereafter VOILA package creates gene splice graphs (**Figure 2**E).
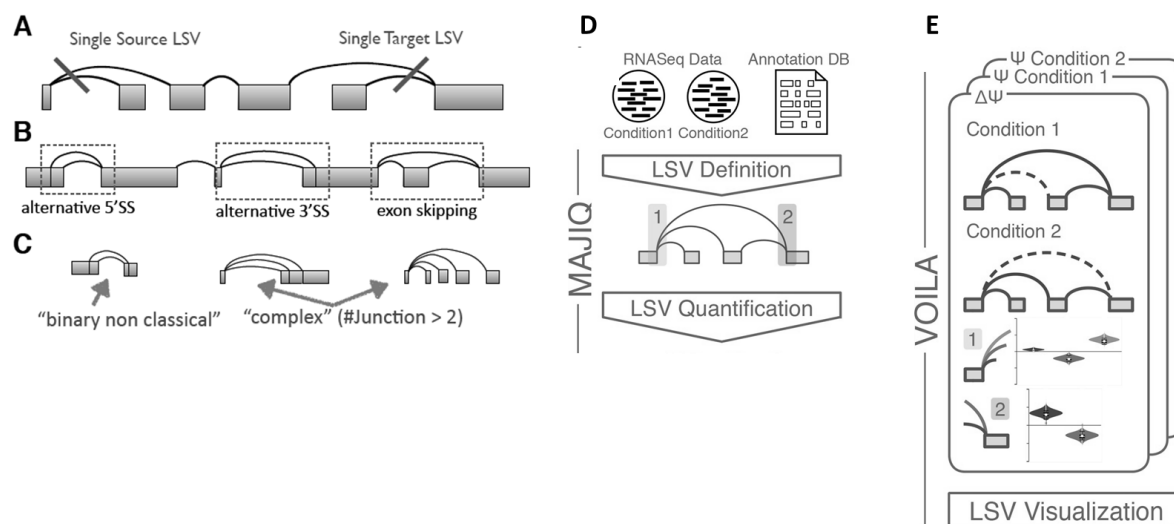
Figure 2 Identification of local splice variations with MAJIQ and VOILA

A-C Definition of local splice variations (LSV). Adapted from [20]. **D+E** Schematic representation of MAJIQ pipeline combined with VOILA visualization tool to identify LSV from RNA-Seq data. Adapted from [19].

Identification of RNA transcripts targeted by RNA-binding proteins

RNA-binding proteins (RBPs) are the key players in post-transcriptional processing of pre-mRNA while identifying *in vivo* target RNAs is still challenging. Both UV-cross-linking and immunoprecipitation (CLIP, [21]) and RNA editing (TRIBE, [22]) are widely used to identify bona fide targets of RBPs. Comparative studies for CLIP and TRIBE are limited so far, although recent reports claim that TRIBE extends and complements targets identified by CLIP [23], [24]. In brief, CLIP is based on UV-crosslinking proteins and bound RNAs within cells, followed by immunoprecipitation and subsequent RNA sequencing [21]. CLIP-based methods require a specific antibody directed against the RBP of interest and a huge amount of input material, which is often not available when working with primary cells.

In contrast, TRIBE (Targets of RNA-binding proteins Identified By Editing) is an antibody-independent approach, which is based on fusing the RBP of interest to the ADAR-RNA editing domain, thereby depositing editing marks on RBP-specific RNA targets [22]. HyperTRIBE (HT) is the improved version of this previously developed technique, carrying a

hyperactive mutation (E488Q) of the ADAR catalytic domain, thereby increasing editing efficiency and reducing sequence bias [25]. In detail, HT fusion protein couples an RBP to the RNA editing domain of *Drosophila* ADAR (dmADAR*), thereby mediating A-I editing in target RNAs. Since only the editing domain of dmADAR is used, the fusion protein lacks the RNA recognition features of ADAR [22]. By this approach, the HT fusion protein marks target RNA transcripts by adenosine-to-inosine (A-to-I) conversions, which are subsequently identified as guanosine (G) in total RNA sequencing. In contrast to CLIP, TRIBE offers the opportunity to identify RBP-specific targets from a limited amount of RNA input [23], [24], [26] and is therefore predestinated for *in vivo* studies.

RNA-binding proteins are key players in the circulatory system

In recent years, several RBPs were found to play important roles in the circulatory system. Mutation of such RBPs often leads to the onset of cardiovascular diseases [27], [28]. In brief, the circulatory system consists of the cardiovascular and the lymphatic system, both transporting fluid through the body. Within the cardiovascular system, the heart pumps blood via the blood vessels towards the organs to supply them with oxygen and nutrients. In parallel, the lymphatic system acts as a waste-disposal system and passively transports lymph fluid back towards the blood circulatory system. While the function of RBPs in the heart has been extensively investigated in recent years, RBPs have not played a major role in vascular research so far.

Since the circulatory system comprises multiple cell types, cell-type-specific RBPs are required for the development and for maintaining functionality. In the heart, almost 400 unique cardiomyocyte-expressed RBPs have been uncovered within the RNA-binding proteome of cardiac HL-1 cells [29]. Besides uncharacterized RBPs, many of those candidates have already been linked to heart failure. During heart development, distinct RBPs are involved in cardiogenesis (reviewed in [27], [30]), and loss or dysfunction of certain RBPs has far-reaching consequences in animal models as well as patients. For example, the loss of cardiac AS factors such as RBFOX1 [31, p. 1], RBM20 [32], or RBM24 [33] causes mis-splicing of key sarcomeric genes, which subsequently impairs cardiomyocyte function.

In comparison to the heart, the relevance of RBPs involved in (lymph-) angiogenesis is poorly studied but has gained increasing attention in recent years ([34], [35]). So far, the cellular effects of alternatively spliced angiogenic genes such as tyrosine kinase receptors and ligands have been investigated in the context of the endothelium (reviewed in [36]), although the corresponding splice factors remain largely unknown. Notably, the loss of selected RBPs leads to profound phenotypes (reviewed in [37]), highlighting the impact of post-transcriptional mRNA processing in endothelial cell subtypes including lymphatic

endothelial cells (LECs). For example, the RBP ZFP36l1 is required for normal vascularization by negatively regulating vascular endothelial growth factor (VEGF)-A expression [38] and *Zfp36l1*-deficient mice die at embryonic day E10.5 due to vascular abnormalities and cardiac defects [38]. However, the relevance of AS in the lymph endothelium remains unknown with some notable exceptions such as NOVA2, which is modulating AS of components of MAPK/ERK signaling pathways and phosphoproteins during lymphatic endothelial cell fate specification in zebrafish and adult human LECs [39].

Development and malformation of the lymphatic system

The mammalian circulatory system encompasses both the cardiovascular and lymphatic system, which are closely connected but maintain distinct functions. In contrast to blood vessels that build a closed circulatory system, the lymphatic system is an open system, allowing the return of lymph fluid and containing components to the blood system and maintaining overall fluid homeostasis. Consequently, lymph vessels are part of the immune system and transport lymph, containing fluid, macromolecules, and white blood cells. Blind-ending lymphatic capillaries absorb these components from the interstitium, which are subsequently transported to the larger collecting vessels via pre-collecting lymphatic vessels. Here, lymphatic valves prevent backflow of the lymph. Finally, collecting vessels transport the lymph fluid back to the bloodstream.

The development of the murine lymphatic systems initiates at E10, via transdifferentiation and sprouting of venous endothelial cells from the cardinal vein (**Figure 3**A). Around E11, bilateral jugular lymph sacs (JLS) are formed in the neck region, sharing a lymphatic-venous cell layer with the adjacent jugular vein [40], [41]. From these JLS, lymph vessels spread across the entire embryo. At E12, the dermal lymph vessels sprout from the lateral side of the embryo and grow towards the dorsal midline of the back skin region. In parallel, non-venous derived progenitor cells originate and migrate towards the lymphatic network [42]. Finally, the lymph vessels from the contralateral sides anastomose at the midline around E17 [42]. The entire mature lymphatic system comprises lymph fluid, lymphatic vessels as well as collecting ducts, lymph nodes, and lymphoid organs (e.g., spleen and thymus).

The developing lymphatic network can be continuously visualized by whole-mount imaging of the dorsal back skin [43] (**Figure 3**B). In this model, several specific markers discriminate lymphatic (LECs) from blood endothelial cells (BECs), including the transcription factor *Prox1* (Prospero-related homeobox-1). *Prox1* acts as an essential driver for the lymphatic vasculature [44], although it is expressed in various tissues [45]. In addition, LECs are characterized by the expression of marker genes including *Lyve1* (lymphatic vessel endothelial hyaluronic acid receptor-1, [46, p. 1]), *Pdpn* (podoplanin, [47]), *Vegfr-3* (vascular

endothelial growth factor receptor 3, [48]) and *Nrp2* (nonkinase receptor neuropilin-2, [49]). BECs and LECs constitutively express the pan-endothelial marker *Cd31* (*PECAM1*), although expression levels are lower in LECs [50], [51].

In general, malformation of blood and lymphatic vessel network can lead to insufficient drainage of lymphatic fluid from the interstitium, resulting in lymphedema formation, characterized by subcutaneous swelling [52]. In humans, mutations in FOCX2 [53], ANGPT2 [54, p. 2] and VEGFR-3 [55] cause lymph vessel dysfunction. *Chy* mouse mutants, which harbor heterozygous inactivating VEGFR-3 missense mutations, display an abrogated lymphatic fluid transport and edema formation in the limbs due to hypoplastic cutaneous lymphatic vessels [49], resembling human lymphatic diseases. Nevertheless, additional non-surgical animal models for lymphedema are still limited.
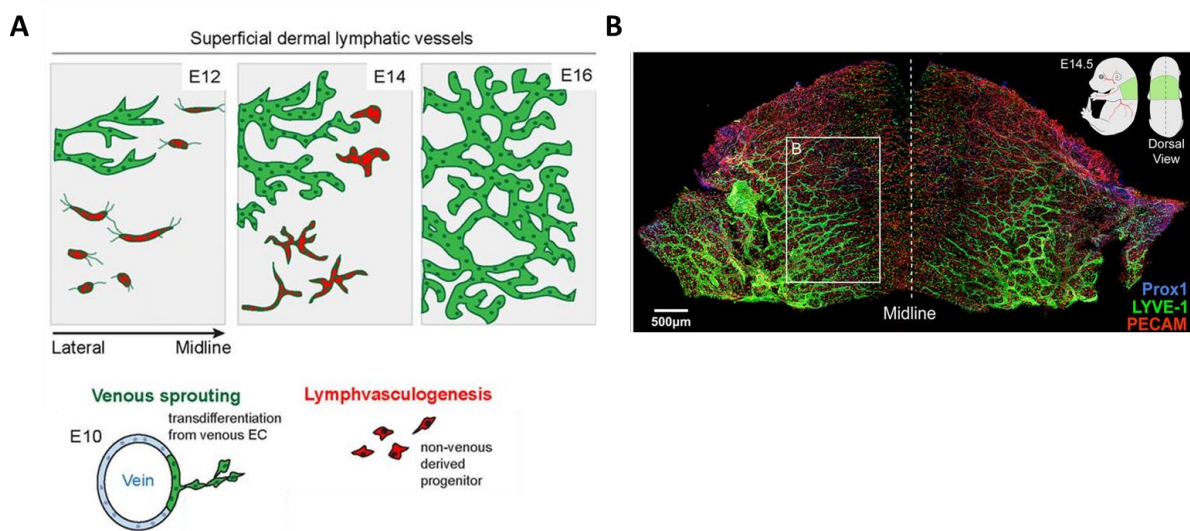
Figure 3 Development of the dermal lymphatic vasculature

A Both, venous sprouting (lymphangiogenesis, in green) and non-venous progenitors (lymphvasculogenesis, in red) contribute to the formation of dermal lymphatic vessels. Thereupon, dermal lymph vessels grow towards the dorsal midline, where they anastomose. Adapted from [42]. **B** Dorsal back skin as model for visualization of lymphatic network dynamics during embryonic development. The green region in the schematic diagram (upper right corner) is selected for confocal tile scan imaging. Here, co-staining of PROX1 (blue) and LYVE1 (green) discriminates LECs from BECs. Adapted from [43].

Cardiomyocyte sarcomeres constitute the contractile units of the myocardium

Depending on the developmental stage, the heart consists of approximately 35-50 % of cardiac muscle cells (cardiomyocytes) [56], whereas endothelial cells and fibroblasts represent the largest population within the cardiac non-muscle cells [56], [57]. The ultrastructure of cardiomyocytes is characterized by the alignment of striated myofibrils, which are composed of sarcomeres representing the smallest contractile subunit of the

myofibril [58]. Within each sarcomere, actin and myosin filaments align and overlap with titin (TTN, **Figure 4**A). Contraction is achieved by sliding of actin filaments along the myosin filaments, leading to sarcomere shortening. During the subsequent relaxation, myosin and actin filaments detach and slide back to their original position, allowing lengthening of the sarcomeres.

The ultrastructure of a sarcomere, as well as pathological alterations, can be visualized by electron microscopy (**Figure 4**B). Here, myosin-containing A-band (thick filaments) appears as dark stained region in the middle of relaxed sarcomere, which is surrounded by two lighter I-bands. These I-bands are composed of a complex formed by actin and tropomyosin (thin filaments). The M-band appears dark in electron microscopy due to the overlap of thick filaments in the center of the sarcomere. Remarkably, a single TTN molecule spans half of the sarcomere length from Z-disk to M-band, where they overlap with contralateral TTN molecules [59]. Titin filaments anchor to Z-disks via α-actinin and telethonin, whereas the contralateral filament end is attached to myosin filaments. Under pathophysiological conditions, changes in ultrastructure results in an impairment of cardiomyocyte contractility.
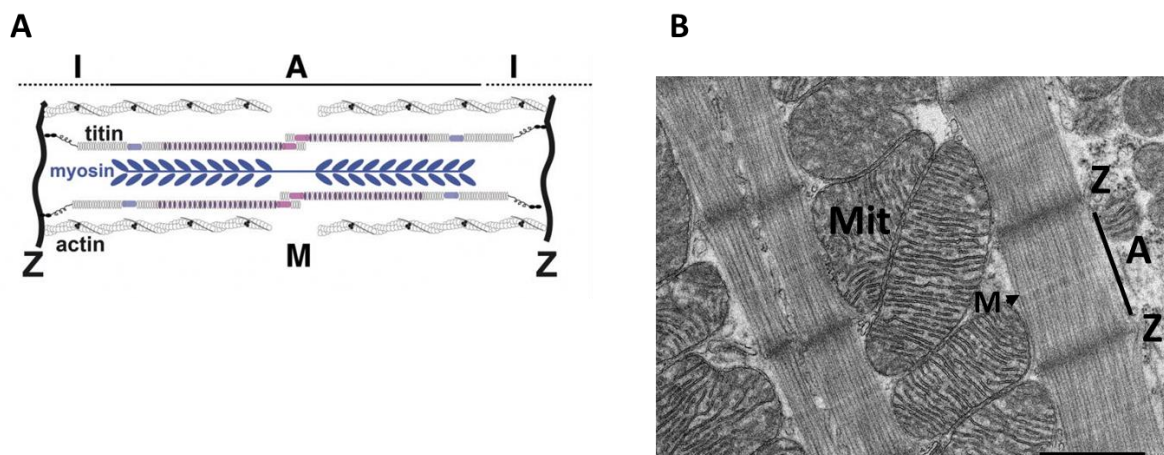
Figure 4 Ultrastructure of cardiomyocyte sarcomeres

A Schematic representation of the sarcomere with indicated positions of the thick myosin-containing filaments (in blue) and the thin actin-containing filaments. Titin spans half a sarcomere from Z-disk to M- band. Scheme adapted from [60]. A= A-band, I= I band, M= M-band, Mit= mitochondrion, Z= Z-disk. **B** Electron microscopy of sarcomere ultrastructure. Electron microscopy image from this study.

Titin is the molecular spring of sarcomeres

Titin (TTN) is the largest identified protein, exclusively expressed in cardiac and skeletal myocytes. Here, TTN is the third most abundant protein following actin and myosin [61]. As part of the contractile machinery, it is involved in muscle assembly, force transmission, and maintenance of resting tension. In detail, TTN centers myosin heads between the actin filaments and restores the contractile apparatus after stretching, thereby maintaining elastic

stabilization and positions of myosin and actin filaments. Since Titin spans the entire distance from the Z-disk to the M-band [59], it exerts its function throughout the length of each half sarcomere [62], [63]. Titin is composed of four major domains (**Figure 5**A). The N-terminus embeds Titin to the sarcomeric Z-disk [64], [65], whereas the C-terminus connects to the M line of sarcomeres [66]. The elastic region of Titin is located in the elastic I-band region, which acts as the main determinant of passive tension in cardiac muscles [67]. Titin filaments in the I-band region are composed of repetitive, extensible tandem immunoglobulin (Ig)-like domains and the PEVK domain, acting as an elastic connector and molecular spring [68]. The A-band domain binds to myosin [69], serving as a semi-rigid region during contraction.
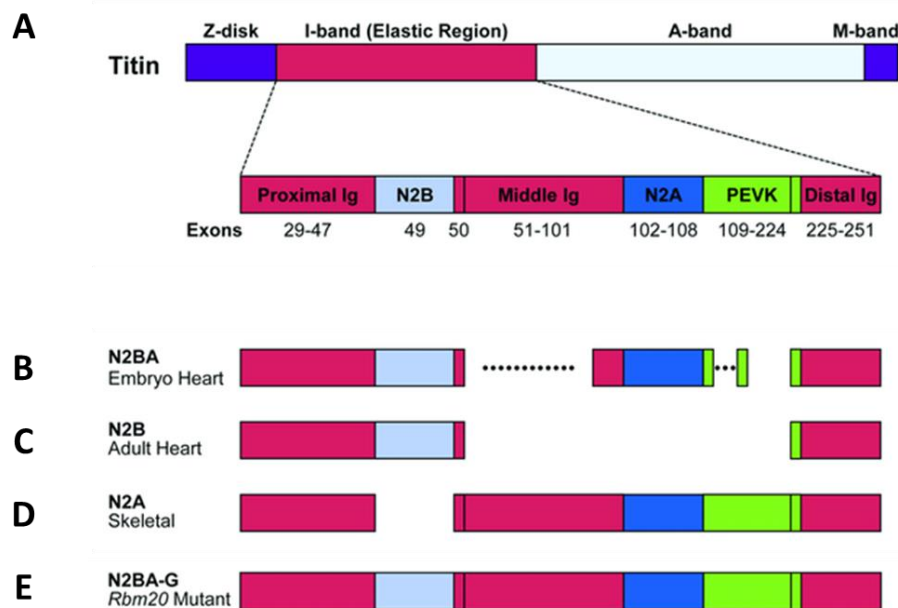
Figure 5 Titin splice isoforms in heart and skeletal muscle cells.

A Domain structures of TTN. **B-E** Schematic representation of titin splice isoforms including embryonic, cardiac N2BA isoforms (**B**) to the adult cardiac N2B (**C**). In skeletal muscle, N2A isoform is expressed (**D**). The giant titin variant N2BA-G is mutually exclusive in *Rbm20*-deficient myocytes (**E**). Adapted from [70].

Titin isoforms are expressed in a developmental and tissue-specific manner, accompanied by extensive alternative splicing events resulting in multiple isoforms from the single gene, which contains 363 coding exons [71], [72]. Two main isoforms are abundant in cardiomyocytes: fetal N2BA (3.7 MDa, **Figure 5**B) and adult N2B (3.0 MDa, **Figure 5**C). The size differences of Titin isoforms occur predominantly due to differential splicing of the tandem Ig and the PEVK segment that comprises the molecular spring. Replacement of the more compliant N2BA to the stiffer N2B form occurs around birth and is completed three weeks after birth [73]. Thereupon, N2B remains the predominant isoform in the adult heart. Titin isoform switching results in stiffening of the titin springs in adult cardiac sarcomeres [73], [74].

Maladaptive alterations in the N2BA:N2B ratio are observed in patients with coronary artery disease [75] or dilated cardiomyopathy (DCM) [76]. In DCM, the N2BA:N2B ratio is increased with an impact on the diastolic filling accompanied by lowering left ventricular myocardial passive stiffness and function [76]. Notably, patients harboring *hRBM20* mutations express a giant titin isoform called N2BA-G (3.9 MDa, **Figure 5**E), which has also been identified in a rat strain encoding an autosomal dominant *Rbm20* mutation [77]. This N2BA-G isoform contains IG and PEVK domains, which are normally skipped by the splice repressor RBM20. Therefore, N2BA-G represents the largest isoform of Titin and is exclusively expressed under pathophysiological conditions in *Rbm20*-deficient myocytes [77].

Pathological alterations and genetic determinants in hypertrophic and dilated cardiomyopathy

Cardiomyopathies comprise a heterogeneous group of heart diseases [78], categorized into primary and secondary cardiomyopathies. Primary cardiomyopathies predominantly affect the heart muscle and have either a genetic or an acquired cause. In contrast, secondary cardiomyopathies occur much more frequently, although multiple organs including the heart muscle are affected. The most common types of primary cardiomyopathies comprise hypertrophic and dilated cardiomyopathy [78].

Hypertrophic Cardiomyopathy (HCM) is characterized by prominent thickening of the left ventricular (LV) wall (and septum), thereby resulting in diastolic heart failure with normal or reduced LV ejection fraction (LVEF). So far, multiple gene mutations are associated with HCM, including *Myh7* [79] and *MYBPC3* [80]. The predominant cardiomyopathy subtype is dilated cardiomyopathy (DCM), which is defined by a dilation of the left (or both) ventricles, accompanied by ventricular wall thinning and increased LV mass. DCM is often coupled with impaired systolic function and arrhythmia, leading to premature death. Here, dilation is a compensatory mechanism to improve diastolic filling, reduce stroke volume, thereby maintaining blood flow in the failing heart [81], [82]. Almost 50% of DCM cases are familial and DCM-associated mutations have been uncovered in approximately 100 genes (reviewed in [60]), mostly encoding cytoskeletal or sarcomeric proteins. Truncating mutations in the *TTN* gene are predominant [83] and impair cardiac elasticity. In addition, defects in the AS machinery can lead to mis-splicing of essential cardiac genes. Along with RBM24 [33] and RBFOX1 [31], RBM20 is by far the most prominent regulator of AS in the mammalian heart [32]. Here, missense mutations in the *hRBM20* gene contribute to a subset of familial DCM cases [84], [85] and result in mis-splicing of at least 30 myocardial transcripts, including *TTN*, *CAMK2D*, and *LDB3* [32].

Clinical and laboratory diagnosis of heart failure

In clinical diagnostics, non-invasive tests such as cardiac magnetic resonance imaging (MRI) and electrocardiography (ECG) are widely used to diagnose impaired heart function or heart failure. MRI measurements enable the visualization of myocardial contraction allowing assessment of heart geometry and function. Heart contraction is defined by two phases, the diastole, and the systole. During the diastole, the heart muscle relaxes and chambers are filled with blood, whereas the systole represents the phase of heart muscle contraction and blood ejection. The ejection fraction (EF) represents the percentage of blood that is pumped out from the left ventricle with each heartbeat, normally ranging from 50-70%. The left ventricular stroke volume (SV) indicates the blood volume, which is ejected from the left ventricle into the aorta during each systolic contraction. Furthermore, the cardiac output (CO) indicates the volume of blood that is ejected per unit of time, calculated by the product of heart rate and SV. Cardiac MRI of patients with DCM typically reveals reduced EF, SV, and CO.

In contrast to MRI, ECG is commonly applied to monitor heart rate and rhythm. The phases of an electrocardiogram trace the atrial (P wave) as well as ventricular (QRS complex) depolarization, followed by ventricular repolarization (T-wave). In cardiomyopathies, changes in the ECG are often only observed in advanced stages without characteristic features and are more likely to indicate the onset of heart failure. In this study, we applied both techniques to record the progression of heart failure in animal models.

In addition to MRI and ECG, molecular biomarkers are used to diagnose heart diseases. Upon cardiac stress, cardiomyocytes become hypertrophic and produce cardiac stress response markers such as atrial (ANP) and B-type (BNP) natriuretic peptides, which are encoded by the natriuretic peptide A (*Nppa*) and -B (*Nppb*) gene cluster [85]. ANP secretion is induced through increased stretching of the right atrium [86], whereas BNP is released from ventricular cardiomyocytes (and infiltrating cells) upon ventricular expansion [87]. Both natriuretic peptides have antifibrotic and antihypertrophic effects and are used as diagnostic or prognostic biomarkers in clinical cardiology. In this study, we made use of these markers to indicate cardiac stress on the transcriptional level.

Similarities and differences between the splice factor paralogs MATR3 and RBM20

Based on homology comparison, MATR3 groups in a family of RNA binding proteins comprising MATR3, RBM20, and ZNF638. All three family members are characterized by highly conserved RRM-motifs, but also show significant differences e.g., concerning the number of RRMs and additional domains (**Figure 6**A) [88]. RBM20 and MATR3 possess

highly similar RNA recognition motifs. MATR3 as well as RBM20 and ZNF638 share the same overall domain organization (**Figure 6**A, [89]), including two zinc finger domains each. A major difference is the number of RRMs, MATR3 contains two RRMs, whereas RBM20 encompasses only one RRM.

The RNA recognition motif of MATR3 (experimental evidence: UUUCUXUUU [90] and predicted: AUCUU [91]) and RBM20 (UCUU [92]) are highly similar but not identical. All three RBPs differ in their tissue-specific expression profiles (**Figure 6**B). RBM20 is predominantly expressed in striated muscle cells (cardiomyocytes and skeletal muscle cells), whereas *Matr3* and *Znf638* are ubiquitously expressed. All three paralogs are co-expressed in the heart and for *Rbm20* and *Matr3* a tight regulation during cardiogenesis has already been reported [93], [94]. Interestingly, RBM20 interacts physically with MATR3 in an RNA-dependent manner, at least in cardiomyocytes [92], raising the question about co-processed splicing targets. Although RBM20 is one of the most intensively investigated RBPs in the heart, a potential overlapping function between both paralogs has not been addressed so far.
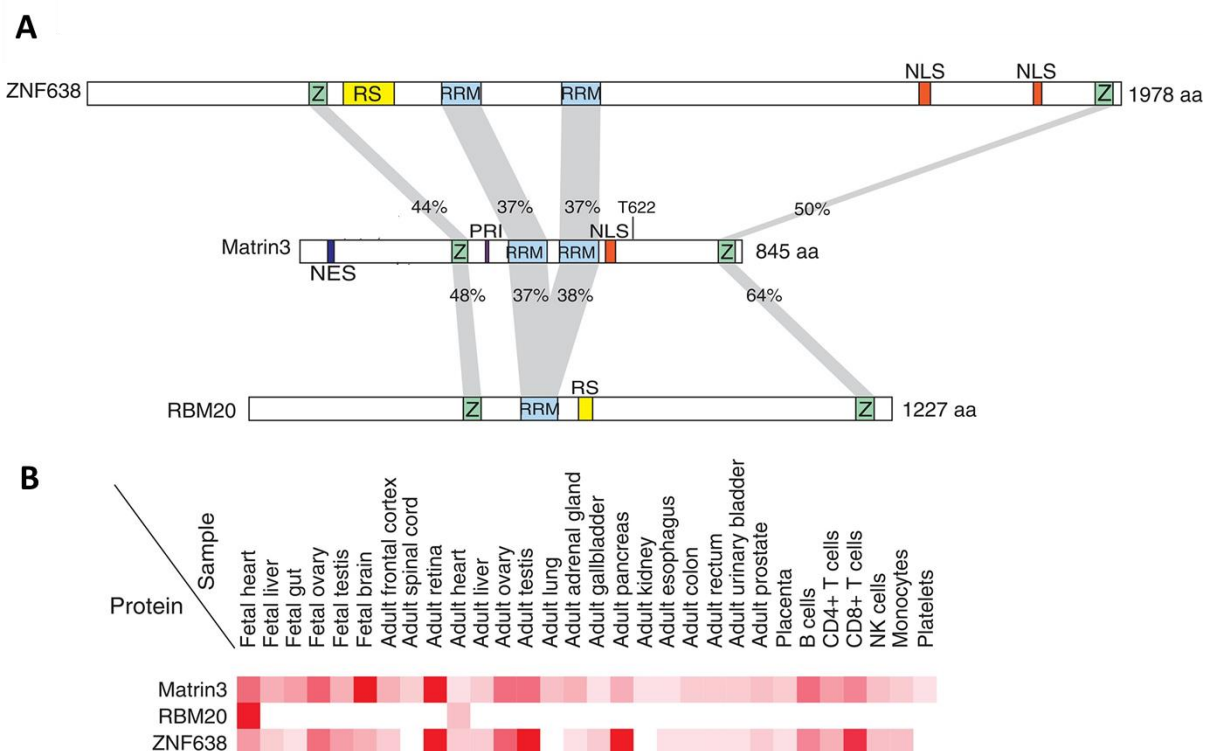
Figure 6 Domain organization of Matrin3 and related paralogs RBM20 and ZNF638

A Schematic diagram of domains from ZNF638, MATR3 and RBM20. RRM: RNA recognition motif, Z: zinc-finger (ZF) domain, NLS: nuclear localization sequence, NES: nuclear export sequence, PRI: PTBP1 RRM interaction motif. Amino acid similarities are presented in percentage. **B** Expression profiles of MATR3, RBM20 and ZNF638. Here, red color intensity correlates with expression level. Adapted from [88].

RBM20 dominates alternative splicing in cardiomyocytes

Muscle-restricted RBM20 acts as a major regulator of mRNA splicing in the mammalian heart by repressing cassette exons and regulating mutually exclusive exon splicing [92]. RBM20 predominantly binds to introns, flanking alternative exons that correlate with splicing repression [92]. At nucleotide-resolution, the RRM domain of RBM20 binds to UCUU-containing RNA sequence [95], [96]. Direct binding of RBM20 to the cardiac-specific target splice sites was revealed by CLIP in HL-1 cells [32] and HITS-CLIP in primary rat cardiomyocytes [92]. Initially, RBM20 was reported to control an alternative splicing network of more than 30 genes common in humans and rats, including sarcomeric and calcium-handling genes [95] (**Figure 7**A). Recently, additional downstream candidates have been identified based on the analysis of alternative splicing in *hRBM20* mutant DCM human induced pluripotent stem cells (hiPSC)-derived cardiomyocytes [97] or human embryonic stem cells (hESC)-derived cardiomyocytes [98].
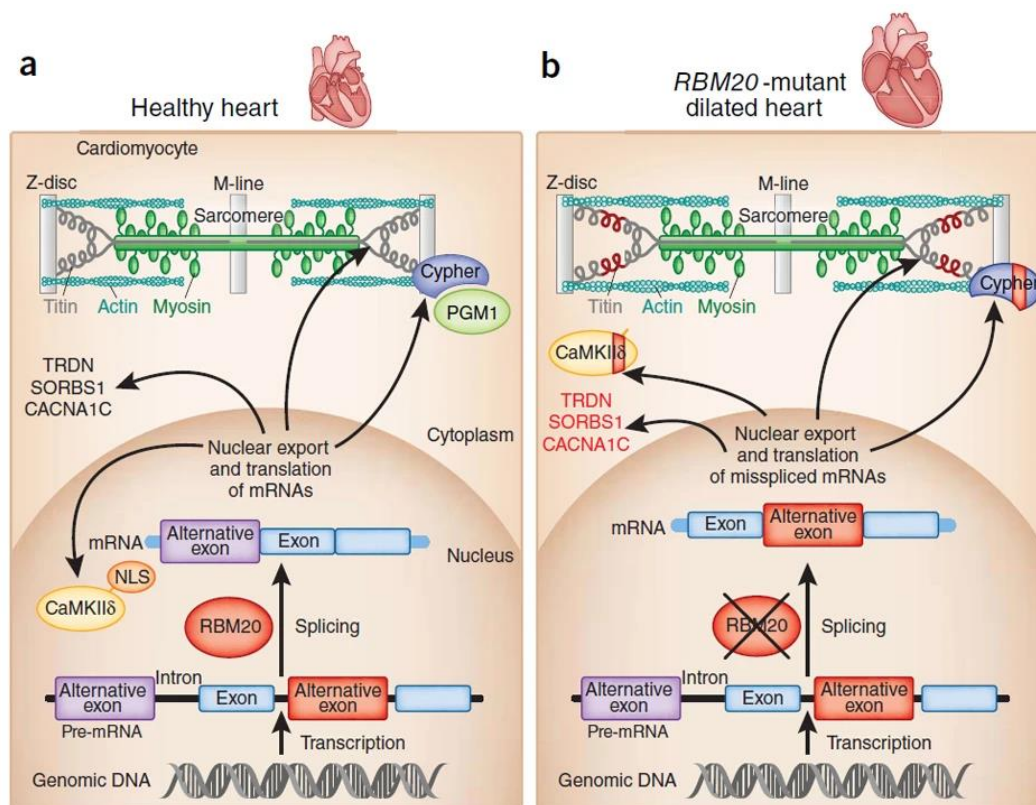
Figure 7 Mis-splicing of cardiac transcripts in the RBM20-mutant dilated heart

Loss-of-function mutations in the splicing factor RBM20 cause dilated cardiomyopathy via the pathological splicing of cardiac genes such as *Ttn*, *CamkIId* and *Ldb3*. Adapted from [99].

Of note, TTN is by far the most prominent mRNA target of RBM20 and in addition the most extensively mis-spliced target after RBM20 loss-of-function. Alternatively spliced exons reside in the elastic PEVK- and the immunoglobulin-rich region within the I band, leading to the giant N2BA titin isoform type, known as N2BA-G [77]. As a result, *Rbm20*-deficient

sarcomeres are characterized by a short and stiff I-band with increased passive tension, resulting in decreased cardiac contractility [32]. RBM20 regulates both linear [32] as well as circular [100] RNA splicing, originating from the titin gene. Besides Titin, loss of RBM20 results in mis-splicing of other cardiac transcripts such as *CamkIId*, *Ldb3* (also known as Cypher), and *Cacna1c* (**Figure 7**B), which are critical drivers for RBM20-dependent cardiomyopathy [101].

This RBM20-dependent pathology has been observed across species e.g., in humans [32], rats [32], [102], and mice [103] with remarkable differences. In humans, multiple *hRBM20* loss-of-function mutations have been linked to familial dilated cardiomyopathy [103]–[105] and left ventricular non-compaction cardiomyopathy [32]. The majority of *hRBM20* loss-of-function mutations missense mutations cluster in the RS domain of exon 9 (out of 14 coding exons; summarized in [101]). These mutations result in defective splicing and thereby trigger the expression of aberrant titin isoforms, as well as of a network of additional myocardial proteins that are concomitantly regulated by RBM20 [99]. RBM20-associated DCM is characterized by a decreased LVEF, dilation of the LV, and an increased risk of arrhythmias and premature death [32].

In *Rbm20*-deficient rats, electron microscopy of the left ventricle revealed altered ultrastructure including myofibril disarray, Z line streaming, and lipofuscin deposits, whereas the skeletal muscle ultrastructure appeared normal [102]. Furthermore, gene expression analysis of left ventricles from *Rbm20*-deficient rats compared to wild types showed an increased cardiac stress response [102]. In mice, the global loss of *Rbm20* does not result in premature death but induces characteristics of DCM such as fibrosis and arrhythmia [103]. This arrhythmia is caused by aberrant mis-splicing of affected Ca^{2+}- and ion-handling genes such as *Camk2d*, resulting in an increased L-type calcium current, intracellular Ca^{2+} overload, and increased sarcoplasmic reticulum Ca^{2+} content in *Rbm20*-deficient cardiomyocytes [103].

A previous report investigating an RBM20 mouse mutant strain indicate ECG abnormalities starting at the age of 6 weeks, including a prolonged PR and heart rate–corrected QT [103]. Recently, a missense mutation in a Arginine-Serine-Arginine-Serine-Proline stretch (not in the RNA-binding domains) of *hRBM20* has been linked to atrial fibrillation, which was recapitulated in *Rbm20*-mutant mice harboring the same missense mutation [106]. Taken together, *Rbm20*-deficient rats phenocopy the DCM phenotype of hRBM20 patients including premature death [102], whereas *Rbm20*-KO mice are viable and exhibit a rather mild phenotype [103].

Matrin3 is a widely expressed and multifunctional RNA-binding protein

Matrin3 is highly conserved through evolution. The amino acid sequence of human (h) *hMATR3* is 96% identical to the rat sequence [107] and 98.5% identical to the murine sequence [108]. Murine *Matr3* is broadly expressed, showing expression peaks in the embryonic brain, heart, and limb, with a gradual decline from newborn to adult stages [94]. Within the brain, *Matr3* is strongly expressed in the brain including the cortex, hippocampus, cerebellum, and spinal cord [109]. In the heart, MATR3 is highly abundant in the nuclei of neonatal mouse cardiomyocytes, as well as in the nuclei of cardiac valve interstitial cells and endocardial cells [94]. Furthermore, MATR3 is also abundant in both arterial smooth muscle cells as well as (arterial and venous) vascular endothelial cells [94], where it exerts essential functions in endothelial cell survival [110]. So far, most functional studies related to MATR3 focus on neuronal cells, since mutations have been linked to the neurological disease amyotrophic lateral sclerosis (ALS).

Domains of MATR3

MATR3 is a nuclear matrix protein, which is predominantly localized in the nucleoplasm, encoding both a bipartite NLS (nuclear localization signal) as well as a NES (nuclear export signal) sequence [111]. Within the nucleoplasm, MATR3 is localized throughout extranucleolar regions of the nucleus, showing diffuse labeling [112]. In addition to NLS and NES sequences, MATR3 harbors two RNA Recognition Motifs (RRM) and two zinc finger (ZnF) domains, which enables RNA and/or DNA binding. The functions of both ZnF domains are less investigated compared to the RRM domains. Several cell culture studies indicate that truncated versions of MATR3 lacking RRM domains facilitate self-assembly of nuclear [113], [114] or cytoplasm [115] granules. The subcellular localization as well as the interaction networks of MATR3 are mainly modulated by the second RRM domain (RRM2) [114], [116], which is mediating the interaction with RNA [117].

MATR3-dependent posttranscriptional regulations

Several studies have emphasized the role of MATR3 in regulating post-transcriptional processes such as alternative splicing (AS) and RNA stability, indicating that MATR3 is involved in multiple steps of RNA processing. Among these, the function of nuclear MATR3 acting as a splicing factor has been examined in depth. *hMATR3* knockdown in SH-SY5Y [90] and HeLa cells [89] significantly changes cassette exon usage, indicating a function as global regulator of AS. More specifically, MATR3 acts as an intronic splicing suppressor, since it binds to an extended region of the pre-mRNA within the repressed exons and the flanking introns [89]. Transcripts that are alternatively spliced by MATR3 are not altered in gene expression [90]. In the context of RNA stability, MATR3 binds mRNA via the RRM2

domain, regulating transcript levels as well as mRNA stability of bound mRNAs [117]. In addition to the previously described nuclear functions, a cytoplasmic C-terminally truncated, cytoplasmic MATR3 variant colocalizes to mRNA processing bodies in stressed cells [115].

MATR3 CLIP data uncovered binding to pyrimidine-rich sequence motifs in regions of repressed exons and adjacent introns [89], [90]. However, contradictory results are published regarding the MATR3 consensus sequence. A global analysis of RNA-binding motifs predicted AUCUU [91], whereas experimental evidence identified UUUCUXUUU [90] as a binding sequence for MATR3. In the context of AS regulation, both RRMs of MATR3 are required [89], even though it has recently been reported that MATR3's DNA-binding activity may antagonize its functions in RNA splicing and stability [118]. The loss of MATR3 might either directly lead to nonsense-mediated mRNA decay (NMD) of target splice mRNA [89] or indirectly influence the mRNA levels due to MATR3-regulated AS events in chromatin-related proteins [119].

The RNA-(in)dependent protein interaction network of MATR3

Various protein-protein interaction studies identified several RNA-(in)dependent binding partners of MATR3 (reviewed in [88]). As part of the nuclear matrix, the C'-terminus of Matrin3 binds directly to Lamin A [120], which is required for nuclear stability and nuclear distribution of MATR3. This interaction is presumably RNA-*in*dependent since Lamin A depletion does not affect MATR3-mediated AS events in U2OS cells [121]. Further reports indicate several nuclear interaction partners of MATR3, in particular several heterogeneous nuclear ribonucleoproteins (hnRNPs), including global splicing regulators hnRNP-K [117], hnRNP-L [112], and hnRNP-M [116], which interact in an RNA-dependent manner. In the process of alternative splicing, MATR3 interacts with PTBP1 via the PRI motif of MATR3 and the second RRM of PTBP1 [89]. Remarkably, some targeted alternative splice events of MATR3 are co-regulated by PTBP1, indicating that both RBPs form overlapping regulatory networks [89].

In cardiomyocytes, RBM20 binds to spliceosomal proteins as well as to MATR3 [92], indicating a physical interaction of both paralogous RBPs. In addition to the interaction with splice factors, MATR3 maintains an RNA-dependent association with proteins involved in RNA processing, such as the DNA and RNA helicase DHX9 [117]. MATR3 also interacts with nuclear-associated RNA-binding proteins such as TARDBP [122] and FUS [123] that have been linked to amyotrophic lateral sclerosis (ALS). In addition, ALS-linked *hMATR3* mutations impair nuclear export of mRNA and alter protein-protein interactions under disease conditions [114], highlighting the impact of the MATR3 protein interaction network.

Matrin3 in human diseases and deduced mouse models

So far, MATR3 has been associated with congenital heart defects and most importantly with the neurodegenerative disorder ALS. In respect to the heart, analysis of patients with congenital disorders of the outflow tract identified disruption of the MATR3 3' UTR as the cause of cardiac left ventricular outflow tract (LVOT) defects [94]. In order to gain further mechanistic insights, a heterozygous Matrin3 mouse gene trap allele (Matr3(Gt-ex13)) was established, mimicking LOVT defects of human patients, although overall MATR3 protein levels remained unaltered in the heart [94]. Several ALS studies demonstrated that mutations and mislocalization in RNA-binding proteins including TARDBP [124], FUS [125], and MATR3 [122] are causative for ALS pathogenesis (reviewed in [126]). So far, a dozen missense mutations in the human *MATR3* gene have been associated with the onset of ALS, in particular, MATR3 variants S85C, F115C, P154S, or T622A [122], [127]–[132]. Patients with the S85C *hMATR3* mutation display no additional pathogenic mutations of ALS-associated genes such as TARDBP or FUS [132].

Unexpectedly, mice overexpressing wild-type human MATR3 display muscle atrophy [133], but the phenotype is milder compared to transgenic mice harboring the missense mutation F115C, which shows severe muscle atrophy, resulting in a shorter life span [133]. Transgenic mice that overexpress mutant S85C MATR3 display myopathic features including fiber-size variations [134], whereas MATR3 S85C knock-in mice mimic early-stage ALS symptoms and exhibit progressive motor deficits including neuroinflammation, loss of Purkinje cells, and neuromuscular junction defects [109]. Overall, S85C mutation of MATR3 recapitulates both myogenic and neurogenic components of ALS [118].

Previous studies have primarily dealt with the function of MATR3 in the nervous system and studies focusing on the function of MATR3 in other cell types are not available. In this study, we addressed the function of MATR3 in the cardiovascular system, particularly in relation to its paralogue RBM20.

Aim of Dissertation

The main aim of this project was to address the impact of MATR3 in splicing processes during cardiovascular development and diseases. To identify affected cell types, germ line as well as cell-type-specific MATR3 knockout mice models were used. In particular, this study focuses on the function of MATR3 as a splice factor in heart muscle cells by analyzing cardiac mRNA targets and mis-spliced transcripts, as well as by phenotypic analysis of MATR3-deficient cardiomyocytes.

Results

Loss of *Rbm20* in the C57BL/6J genetic background does not result in dilated cardiomyopathy and premature death

To assess the cardiac phenotypes upon loss of muscle-restricted *Rbm20*, a germ line *Rbm20* knockout mouse model was generated by targeted deletion of exons 4 and 5 of the *Rbm20* gene. *Rbm20* mutant mice were maintained in the inbred C57BL/6J genetic background. Notably, the identical gene-targeting strategy was applied in previous studies to mice in a FVB genetic background [103], [106]. C57BL6J/RBM20KO hearts showed a complete loss of the RBM20 transcript (**Figure 8**A) and protein (**Figure 8**B), indicated by the loss of both murine isoforms. *Rbm20*-deficiency did not affect the expression or protein level of its paralog Matrin3 (**Figure 8**A, B).
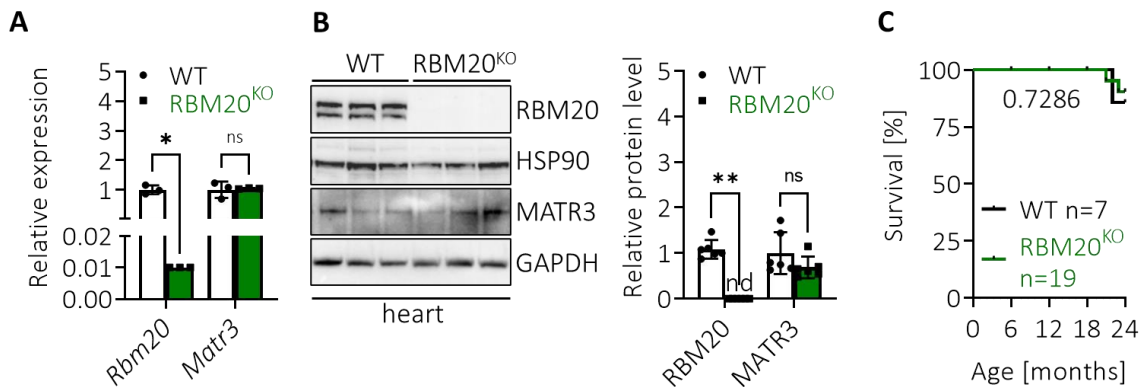
Figure 8 Knockout validation of RBM20KO hearts

A qRT-PCR analysis for *Rbm20* and *Matr3* transcripts in RBM20KO hearts compared to WT samples (n=3). **B** Representative Western blotting (n=3) and quantification (n=6) of heart lysate from 1-year-old RBM20KO and WT. GAPDH and HSP90 were used as loading control. Nd= not detected. **A+B** Data represent the mean ± SD. Two-way ANOVA with Bonferroni's multiple comparisons test. Ns= not significant, * P < 0.05, **P < 0.01. **C** Kaplan-Meier survival curves with Gehan-Breslow-Wilcoxon test for RBM20KO mice and littermate controls. There is no significant (p-value = 0.7286) difference between the two groups regarding the survival within the follow-up time of 24 months.

Remarkably, homozygous RBM20KO mutant mice are viable (**Figure 8**C), consistent with previous reports [103], [106]. By one year, the morphology of RBM20KO heart did not exhibit obvious abnormalities or left ventricular dilatation (**Figure 9**A). In contrast to a previous study using 25-week-old *Rbm20*-deficient mice [103], our 1-year-old KO hearts did not show fibrosis, as demonstrated by Sirius Red/Fast Green Collagen (**Figure 9**B) and Masson's Trichrome (data not shown) staining. Concomitant with this observation, transcript levels of collagen 1a1 and collagen 4a1 as well as most cardiac stress markers were not significantly increased in *Rbm20*-deficient hearts (**Figure 9**E). The overall ultrastructure of the left

ventricle (**Figure 9**C) and *Musculus tibialis anterior* (TA, **Figure 9**D) did not differ between RBM20^{KO} and age-matched controls. In particular, electron microscopy did not uncover any collagen deposition in the left ventricle of 1-year-old KO hearts.
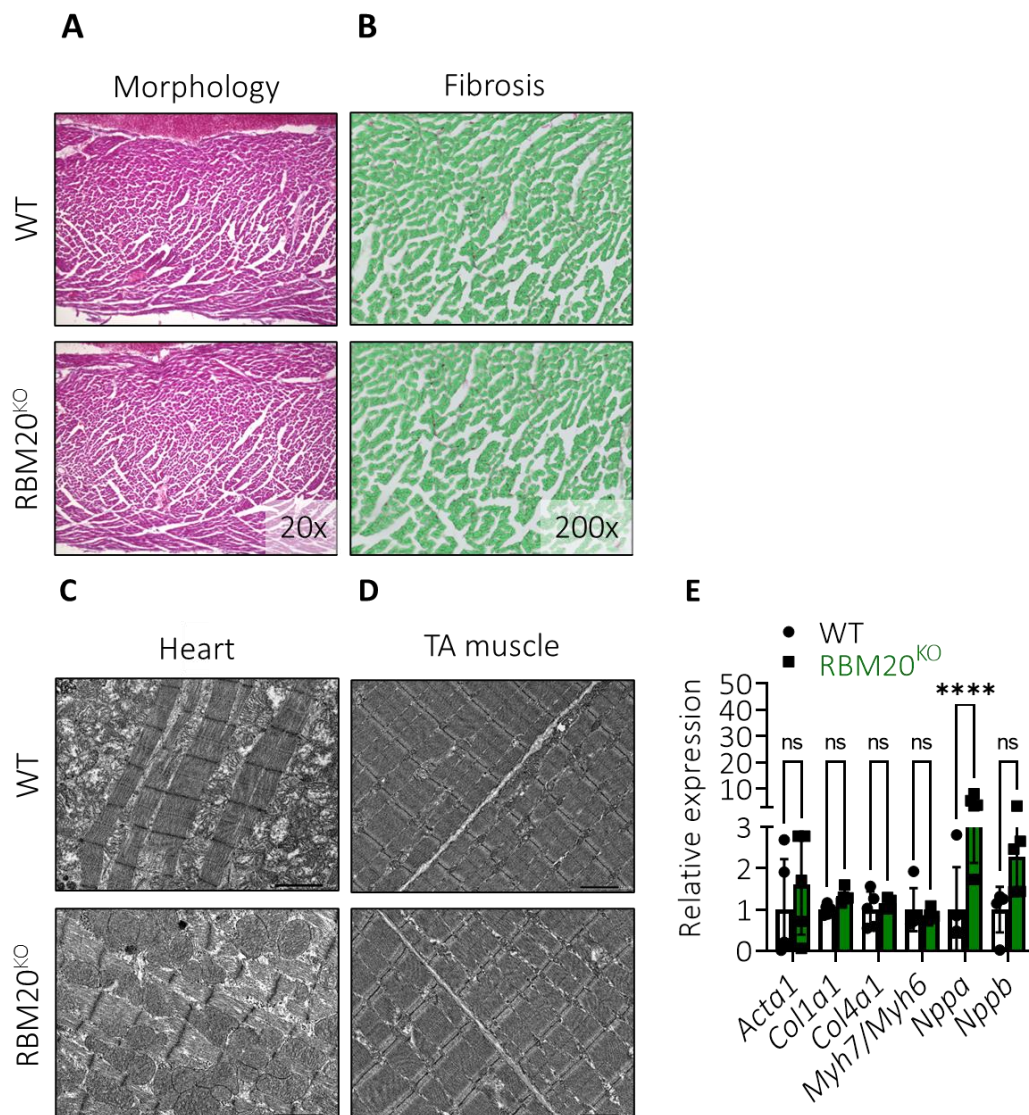
Figure 9 Characterization of 1-year-old RBM20^{KO} mice

A HE and **B** Sirius Red/Fast Green Collagen staining of WT and homozygous RBM20^{KO} heart sections show normal morphology without fibrosis. **C+D** Normal ultrastructure of wild type and homozygous RBM20^{KO} left ventricle (D) and *Musculus tibialis anterior* (TA). Scale bar: 2μm. **E** qRT-PCR reveals cardiac stress response but not increased collagen synthesis in RBM20^{KO} hearts (n=5). Data represent the mean ± SD. Two-way ANOVA with Bonferroni's multiple comparisons test. ns= not significant, ****$P < 0.0001$.

The cardiac function of the KO heart was evaluated by both cardiac magnetic resonance imaging (MRI) and echocardiography (ECG). The left ventricular ejection fraction (LVEF) of *Rbm20*-deficient hearts is not significantly reduced over time, when compared to age-matched littermate controls (**Figure 10**A), indicating that the loss of RBM20 on the C57BL/6J genetic background does not impair cardiac function. However, mutant Titin N2BA-G occurs

on C57BL6J as well as on the FVB background (see **Figure 46**, page 56) and hence cannot be the critical driver for the pathological alterations.

In addition, the normalized LV mass was not significantly changed in RBM20[KO] (**Figure 10**B), complementing that they do not develop DCM. Nonetheless, ECG measurements of 1-year-old RBM20[KO] mice revealed the absence of the P wave (representing atrial depolarization) and a prolonged ST segment (interval between ventricular depolarization and repolarization; **Figure 10**C). The absent P waves partially combined with irregular RR intervals concomitant with normal QRS complexes in the ECG indicate atrial fibrillation in our RBM20[KO] mice, which has already been described for human and rodents with RBM20 mutations [103], [106], [135], [136]. Further studies are required to classify this electrophysiological phenotype and to evaluate whether *Rbm20*-deficient mice have a predisposition to arrhythmia. Taken together, the RBM20[KO] mouse line reported here does not exhibit obvious characteristics of dilated cardiomyopathy although arrhythmias might occur in aged animals. Given that the constitutive depletion of *Rbm20* did not result in a DCM-like heart phenotype, we raised the question whether MATR3, the paralog of RBM20, is essential for the murine heart development and maturation.
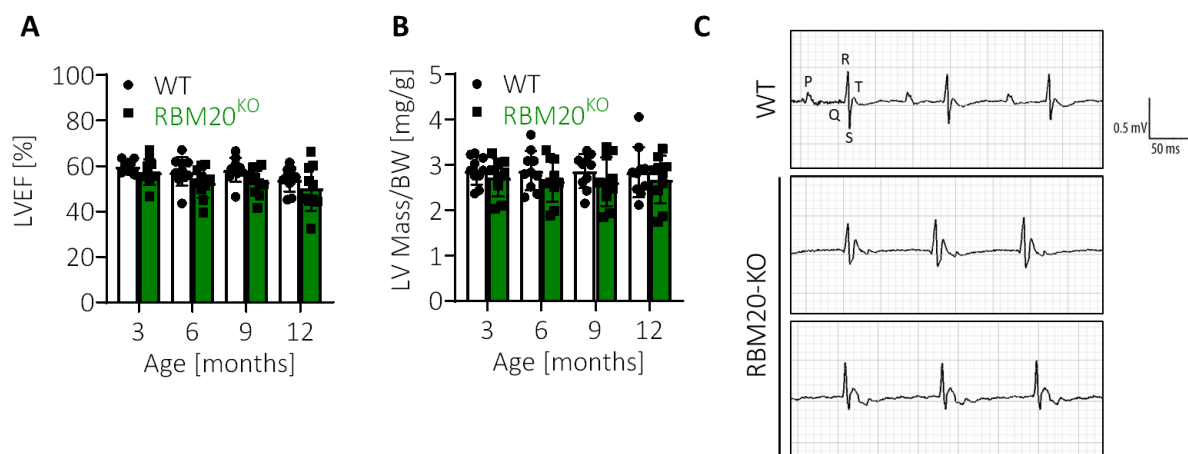
Figure 10 Cardiac function of *Rbm20*-deficient hearts

A Left ventricular ejection fraction (LVEF) of control and RBM20[KO] hearts were assessed by cardiac MRI examination (n=10). **B** Left ventricular (LV) mass quantification using cardiac MRI, which was normalized to the bodyweight (n=10). **A+B** Data represent the mean ± SD. Two-way ANOVA with Bonferroni's multiple comparisons test. No statistically significant difference between the genotypes and time points. **C** Representative surface echocardiography (ECG) from 1-year old wild type and RBM20[KO] mice.

Constitutive deletion of *Matr3* in mice leads to subcutaneous edema and embryonic lethality

Matr3 is widely expressed in various tissues and particularly enriched in the brain, neural crest, developing heart, and great vessels [94]. To determine the predominant *in vivo* function of Matrin3, constitutive (global) *Matr3* knockout mice were generated. Homozygous Matr3^{KO} (Matr3$^{KO/KO}$) mice were obtained from Matr3$^{+/-}$ (heterozygous) intercrosses resulting in a mendelian inheritance of 25%. This expected Mendelian ratio was observed from E12.5 until E16.5, but the percentage of Matr3^{KO} embryos dropped to 0% at E17.5 and no Matr3^{KO} pups were born (**Figure 11**A), indicating late embryonic lethality. Matr3^{KO} embryos exhibited various degrees of subcutaneous edema around the back regions from E14.5 to E16.5 (**Figure 11**B, arrow). Edema occurred in 20% of E14.5, 70% of E15.5 and, 77% of E16.5 Matr3^{KO} embryos (**Figure 11**C). In conclusion, global deletion of *Matr3* in mice causes embryonic lethality around E17, indicating that MATR3 is essential for embryonic viability.
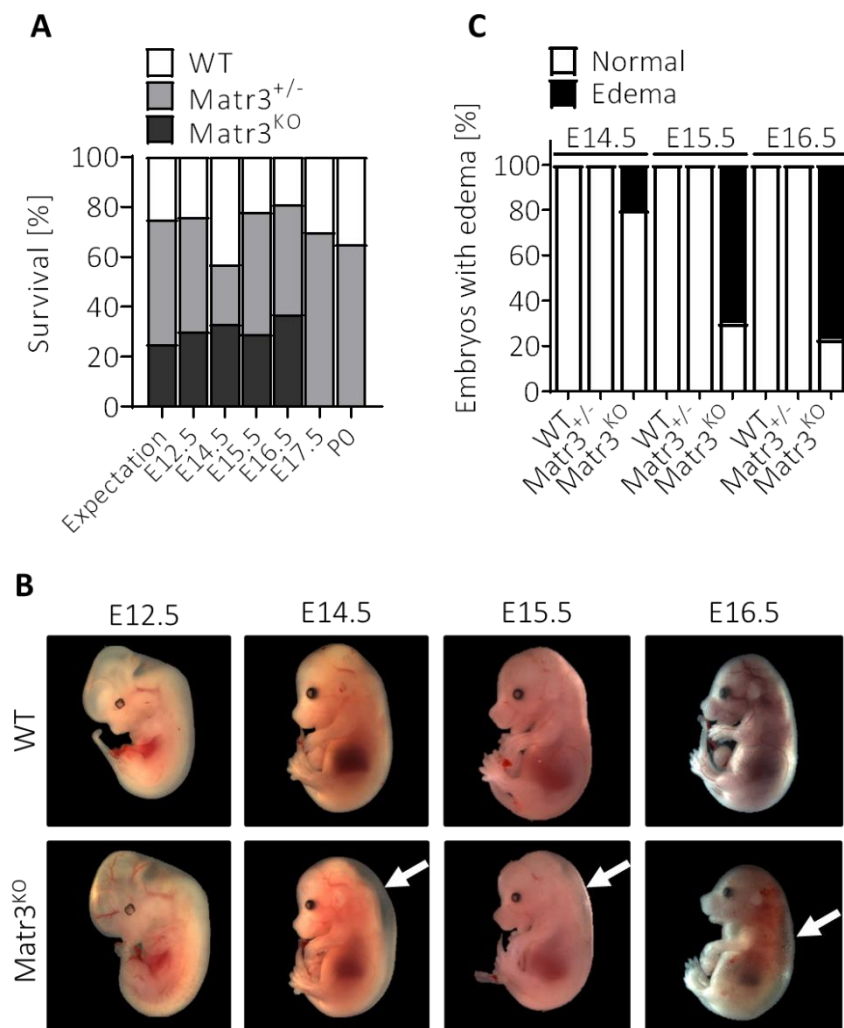
Figure 11 Global *Matr3* knockout mice are embryonically lethal and exhibit edema

A Viability of constitutive Matr3^{KO}, obtained from heterozygous (Matr3$^{+/-}$) intercrosses (n=5 litters per time point).
B Representative images showing the lateral view of whole-mount embryos at different embryonic stages of

development. White arrows indicate subcutaneous swelling in the back region of Matr3[KO] embryos. Not to scale. **C** Percentage of E14.5 to E16.5 embryos with subcutaneous lymph edema, which were restricted to Matr3[KO] embryos (n=5 litters per time point).

Matr3-null embryos display defects in blood and lymphatic network development
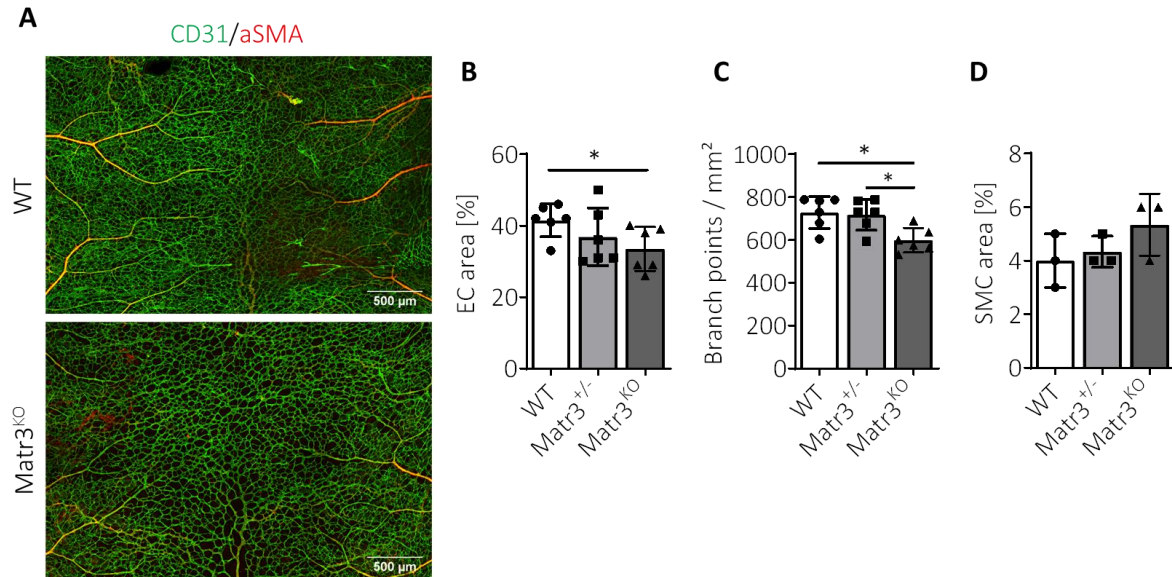
Figure 12 Slight reduction of blood vessel connectivity in constitutive Matr3[KO] skins

A Whole mount confocal images of anterior dorsal skin dissected from E15.5 mouse embryos with indicated genotypes, which were immunolabeled with anti-CD31 (green) and smooth muscle α-actin (αSMA, red). Quantification of **B** area covered by endothelial cells (CD31^{pos}; n=6), **C** branch points per mm² (n=6) and **D** area covered by smooth muscle cells (ACTA2^{pos}; n=3). **B-D** Data represent the mean ± SD. Two-way ANOVA with Tukey's multiple comparisons test. * $P < 0.05$.

To determine the underlying reasons for the edema, we examined the blood and lymphatic vascular network formation in the back skin of Matr3[KO] embryos by immunofluorescence staining. In general, the lymphatic network migration follows blood vessel remodeling within the dermis [43]. Both, the distribution and connectivity of blood vessels were visualized in the embryonic back skin of E15.5 Matr3[KO] and littermate controls with the endothelial marker CD31 and the smooth-muscle marker αSMA (**Figure 12**A). The coverage with CD31^{pos} endothelial cells in the dermis of Matr3[KO] was slightly diminished compared to WT littermates (**Figure 12**B). In addition, the number of endothelial branch points per mm² was diminished, indicating an impaired blood vessel connectivity in Matr3[KO] skins (**Figure 12**C). However, the area covered with αSMA[pos] smooth muscle cells was not significantly altered (**Figure 12**D). Taken together, the global loss of *Matr3* exhibits only a minor effect on the blood vasculature.

Given that constitutive Matr3[KO] embryos exhibit lymphedema, the lymph vasculature attracted our attention. Whole-mount immunostaining of E15.5 embryonic skins with LEC

marker Neuropillin-2 (NRP2) demonstrated reduced migration of dermal LECs in Matr3[KO] compared to littermate controls (**Figure 13**A). During normal lymphangiogenesis, a complex lymphatic network covers the majority of the dorsal skin in E15.5; however, migratory LECs have not yet reached the dorsal midline [42]. In Matr3[KO] embryos, the extension of the dermal lymphatic vessel frontline toward the dorsal midline was delayed (**Figure 13**B). In addition, the average lymph vessel width was increased by 2-fold (**Figure 13**C), whereas the number of dermal lymphatic branch points was diminished in Matr3[KO] (**Figure 13**D). Taken together, these results demonstrate a decreased complexity of the lymphatic network due to lymph vessel hypertrophy in *Matr3*-null skins.
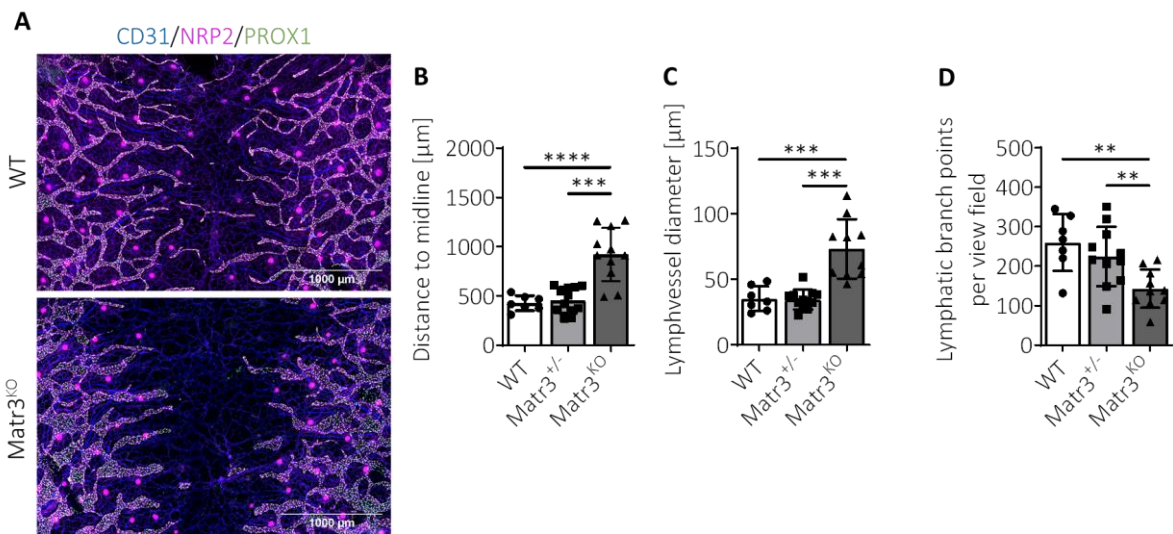
Figure 13 *Matr3*-null embryos exhibit dermal lymphatic defects

A Confocal images of E15.5 whole-mounted, anterior dorsal skins with indicated genotypes. Skins were immunolabeled with CD31 (blue), PROX1 (green) and NRP2 (red) antibodies. Of note, NRP2 labels also hair follicles. **B** Length of the distal migration front, measured as the distance from the lymphatic tip cells to closure starting laterally (n≥7). **C** Quantification of the average lymph vessel diameter in μm (n≥7). **D** Quantification of lymphatic network branching analysis, given as lymphatic branch points per mm vessel length (n≥7). **B-D** Data represent the mean ± SD. Two-way ANOVA with Tukey's multiple comparisons test. **P < 0.01; ***P < 0.00; ****P < 0.0001.

Further analysis revealed a significant increase in Prox1^{pos} LECs per vessel length (**Figure 14**A, B), indicating hyperplasia of *Matr3*-deficient dermal LECs. To further characterize this hyperplastic phenotype, the number of proliferating, dermal LECs was determined by co-staining for nuclear LEC marker PROX1 and proliferation marker Ki67 (**Figure 14**C). Here, the proportion of proliferating LECs (Ki67/PROX1 double-positive nuclei) is increased 2-fold in E15.5 Matr3[KO] mice compared to littermate controls (**Figure 14**D). Taken together, the decreased branching complexity coupled with hyper-proliferation of LECs results in dermal lymphatic vessel hyperplasia, suggesting an essential role of MATR3 during dermal lymphatic network morphogenesis.
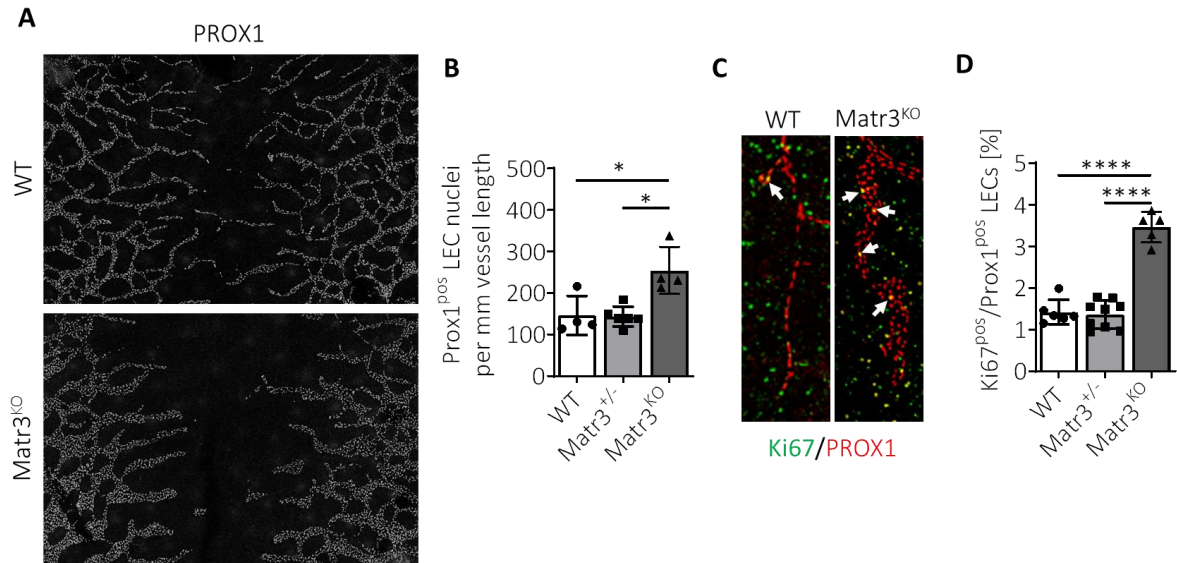
Figure 14 Loss of *Matr3* promotes hyperproliferation of lymphatic endothelial cells

A Whole mount confocal images of the dorsal skin shown in **Figure 13** A, here depicted only for the lymphatic nuclei marker PROX1. Scale bar: 1000μm. **B** Quantification of PROX1^{pos} LEC nuclei per mm lymph vessel length in the dorsal skin of embryos with indicated genotypes (n≥4). **C+D** Representative image of PROX1 (red) and Ki67 (green) co-staining of embryonic dorsal skins and corresponding quantification of proliferative LECs (PROX1^{pos}/Ki67^{pos}, see arrows) in Matr3[KO] compared with littermate controls. **B+D** Data represent the mean ± SD. Two-way ANOVA with Tukey's multiple comparisons test. * P < 0.05; ****P < 0.0001.

To determine whether the loss of MATR3 also affects additional lymphatic structures, bilateral jugular lymph sacs (JLS) of E14.5 Matr3[KO] and littermates were examined. The JLS of E14.5 *Matr3*-null embryos are significantly dilated compared to wild type littermates (**Figure 15**A+B). In contrast, the area of the jugular veins (JV) remains unchanged, resulting in an increased JLS:JL ratio (**Figure 15**C). Our findings underline, that lymphatic abnormalities arise already in early structures of lymphatic development and are not restricted to the skin upon MATR3 loss.
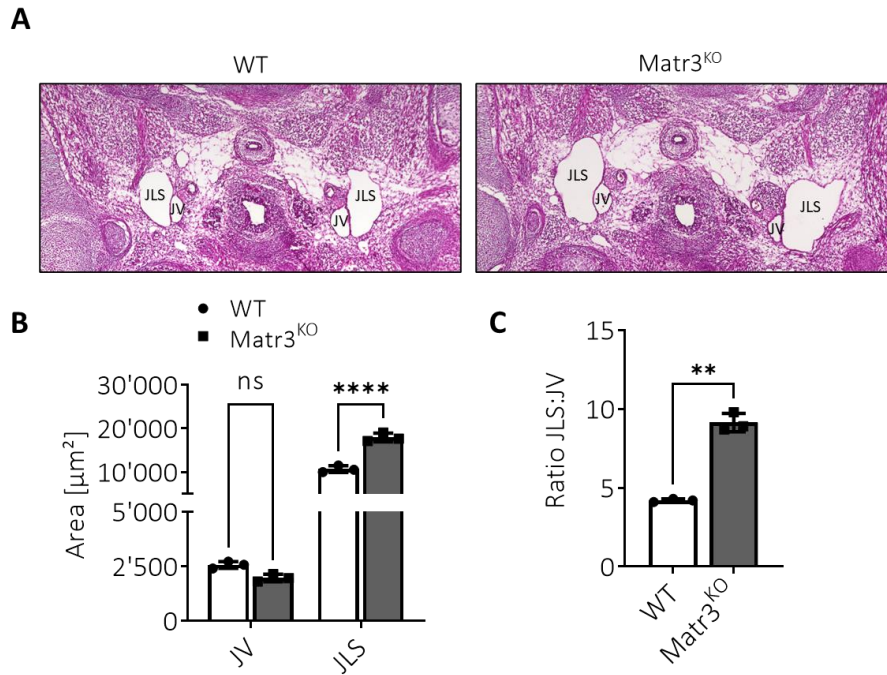
Figure 15 Jugular lymph sacs are enlarged in E14.5 Matr3[KO] embryos

A HE staining of cryo-sections showing paired jugular lymph sacs (JLS) and jugular veins (JV) from wild type and Matr3[KO] at E14.5 (n=3). **B** Quantification of JLS and JV areas. Data represent the mean ± SD. Two-way ANOVA with Bonferroni's multiple comparisons test. ****$P < 0.0001$. **C** Ratio from JLS to JV. Data represent the mean ± SD. Two-tailed paired t-test. **$P < 0.01$.

Endothelial-specific knockout of *Matr3* has no obvious effects on angiogenesis

A previous cell culture study proposed Matrin3 as a key regulator of endothelial cell survival since siRNA-mediated knockdown of *hMATR3* reduced proliferation and led to necrosis of human endothelial cell line EA.hy926 [110]. To determine effects of *Matr3* deletion on blood angiogenesis *in vivo*, a Tie2-Cre [137] mediated vascular endothelial-restricted Matr3[EC-cKO] knockout (Tie2-Cre[pos/wt];Matr3^{fl/fl}) mouse strain was generated. For this purpose, male Tie2-Cre[pos/wt];Matr3^{fl/+} were bred with female Matr3^{fl/fl}, avoiding recombination in the female germline.

In contrast to the proposed function in cultured human endothelial cells [110], Matr3[EC-cKO] mice were viable and fertile with a normal lifespan. Notably, no edema formation was observed in Matr3[EC-cKO] at E15.5 (data not shown). Immunofluorescence staining of developing blood vessels in embryonic dorsal skin visualized normal vasculature formation (**Figure 16**A) and confirmed the endothelial cell-specific knockout (**Figure 16**B) in Matr3[EC-cKO]. The area covered by endothelial cells as well as the number of branch points were not significantly changed (**Figure 16**C), indicating that MATR3 is not crucial for angiogenesis. Taken together, these data indicate that the loss of *Matr3* in vascular endothelium is not causative for embryonic lethality of *Matr3*-null embryos.
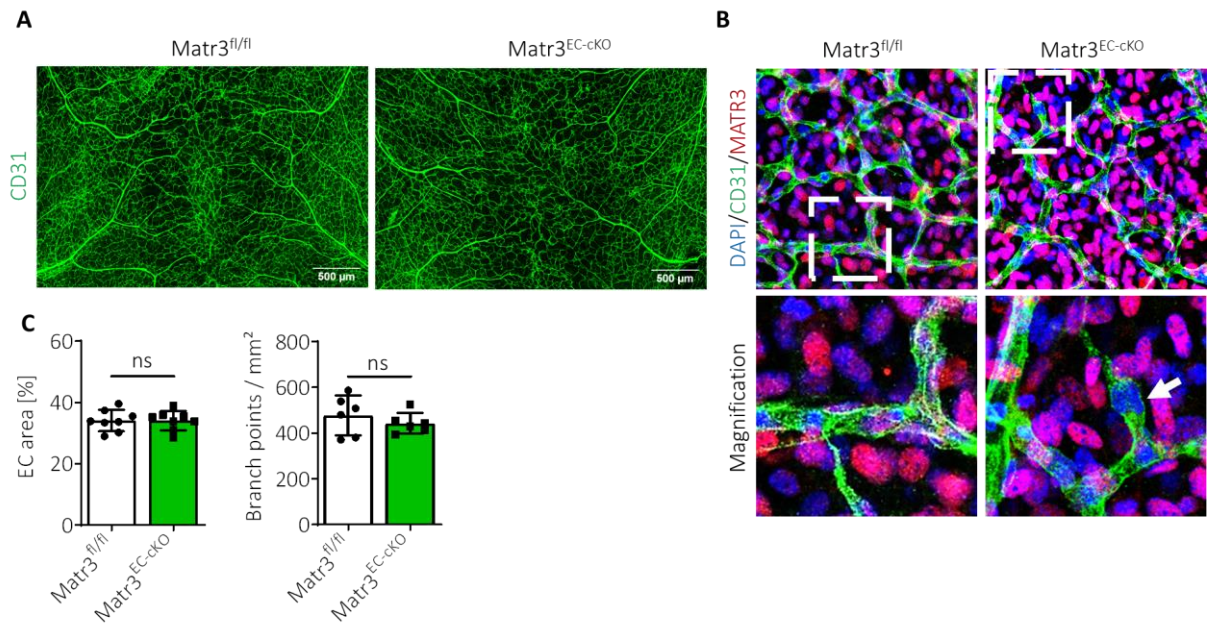
Figure 16 Vascular endothelial cell (EC)-specific *Matr3* knockout mice do not exhibit a phenotype

A Representative confocal tiled z-stack images of a whole-mount anterior dorsal skin dissected from E15.5 mouse embryos with indicated genotypes, which were immunolabeled with anti-CD31 (green). Scale bar: 500µm. **B** Confocal z-stack image (63×) of vessels from E15.5 dorsal skin stained with anti-MATR3 (red), anti-CD31 (green) and DAPI (blue). Arrow labels representative *Matr3*-depleted endothelial cells in Matr3[EC-cKO]. **C** Quantification of endothelial (CD31^{pos}) area per 10x view field (n=8) and quantification of branch points per mm² (n=6). Data represent the mean ± SD. Two-tailed paired t-test. ns: not significant.

Conditional loss of *Matr3* in lymphatic endothelial cells resembles the phenotype of *Matr3*-null embryos
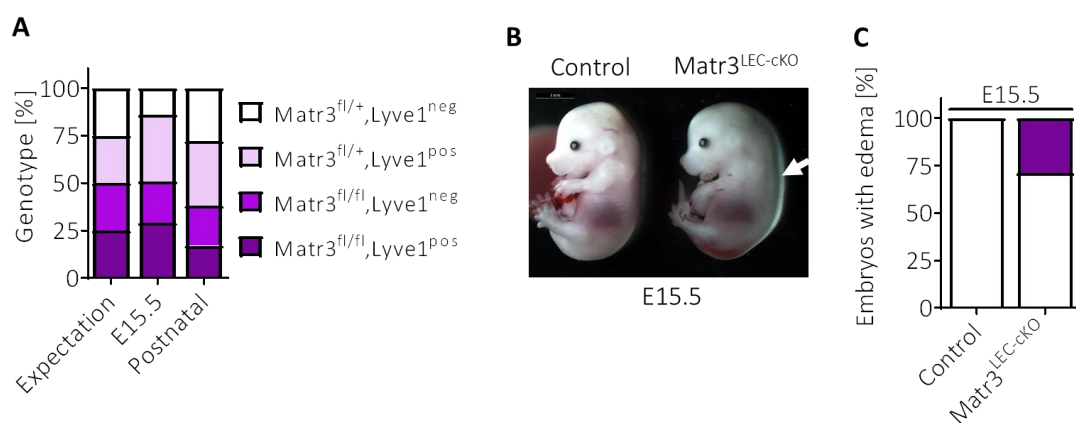
Figure 17 LEC-specific knockout of *Matr3* leads to edema formation and embryonic lethality

A Viability of Matr3[LEC-cKO] and littermate controls with indicated genotypes at E15.5 and postnatal pups (n=5 litters for each time point). **B** Representative image of control and knockout embryo at E15.5. Note the edema at the back of the Matr3[LEC-cKO]. **C** Percentages of edematous embryos with indicated genotypes at E15.5.

To investigate the effect of MATR3 depletion in the developing lymphatic vasculature, a lymphatic endothelial cell (LEC)-specific *Matr3* conditional knockout was analyzed. Therefore, Lyve1[Cre] mice were bred with Matr3^{fl/fl} mice to obtain conditional Matr3[LEC-cKO] mice (Lyve1-eGFP-hCre[pos/wt]; Matr3^{fl/fl}). Lyve1[Cre] mice express eGFP-hCRE from the *Lyve1* locus and exhibit efficient recombination of loxP-flanked genes in LECs and macrophages [138], [139]. Matr3[LEC-cKO] are viable but born at lower Mendelian frequencies (17% instead of the expected 25%), indicating a partial embryonic lethality (**Figure 17**A). At E15.5, one-third of Matr3[LEC-cKO] embryos exhibit subcutaneous edema (**Figure 17**B+C), which might result in abortion.

The inconsistent occurrence of embryonic lymphedema and lethality of Matr3[LEC-cKO] mice might be caused by an insufficient Cre-mediated recombination rate in LECs. To confirm this hypothesis, the expression of the Lyve1-eGFP-hCre was determined in heterozygous Lyve1[Cre] skins (Lyve1-eGFP-hCre[pos/wt]). eGFP serves as a viewer to monitor Cre expression driven by the endogenous Lyve1 promoter for the actual expression at the indicated time point and GFP/PROX1 double-positive nuclei marked Lyve1-driven expression of Cre recombinase monitored by eGFP. The analysis of E15.5 Lyve1[Cre] skins revealed a mosaic pattern of the GFP positive nuclei of both PROX1^{pos} LECs (**Figure 18**A, in yellow) and dermal PROX1^{neg} macrophages (**Figure 18**A, in green). In LECs, the percentage of GFP/PROX1 double-positive nuclei varies between approximately 70% to 90% (**Figure 18**B), suggesting an incomplete recombination rate. Subsequently, we hypothesized that embryos with high recombination efficiency display edema, in contrast to non-edematous embryos with less recombination.
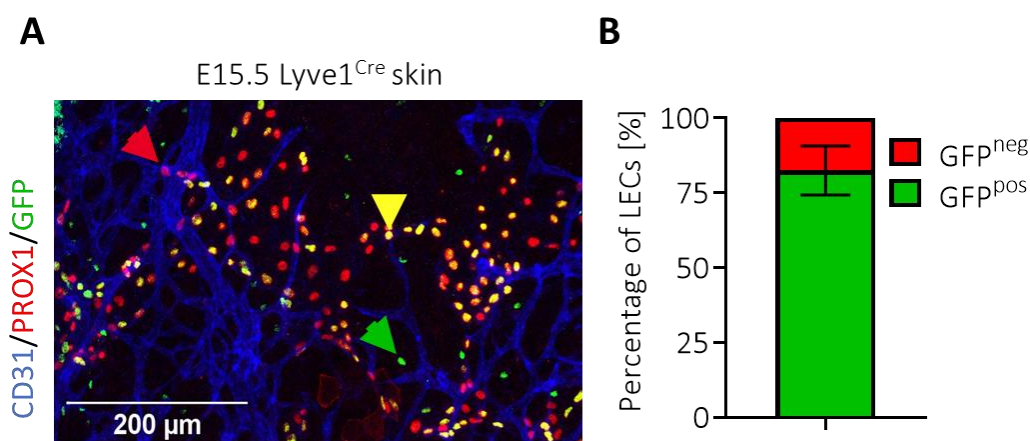
Figure 18 Mosaic pattern of Lyve1-eGFP-hCre in embryonic skins

A Representative image of E15.5 Lyve1[Cre] skin, co-stained with CD31 (blue), PROX1 (red) and GFP (green). GFP staining indicates Cre expression in LECs (PROX1^{pos}, yellow arrowhead) and macrophages (PROX1^{neg}, green arrowhead). **B** Percentage of dermal GFP[pos] LEC in E15.5 Lyve1[Cre] (n=4) ranging from 71 to 90%.

The developing lymphatic network of E15.5 Matr3[LEC-cKO] and littermate controls was investigated in the back skin by IF staining using antibodies against LYVE1 and PROX1 (**Figure 19**A). Remarkably, all examined E15.5 knockouts (with or without edema) displayed an abnormal lymphatic network, characterized by delayed extension of the front tip of lymphatic vessels towards the dorsal midline (**Figure 19**B). In addition, *Matr3*-depleted lymphatic vessels are thinner (**Figure 19**C) and shape fewer branch points (**Figure 19**D). On average, the blood vessel patterning (coverage with CD31^{pos} BECs) was not impaired upon LEC-specific MATR3 inactivation (**Figure 19**E), but shows a high variability within the examined triplicate. Taken together, these results indicate that MATR3 is essential for lymphangiogenesis and LEC-specific loss of MATR3 manifests in subcutaneous edema. Further experiments are required to analyze whether the LEC-specific KO of MATR3 recapitulates LEC hyper-proliferation observed in constitutive MATR3[KO].
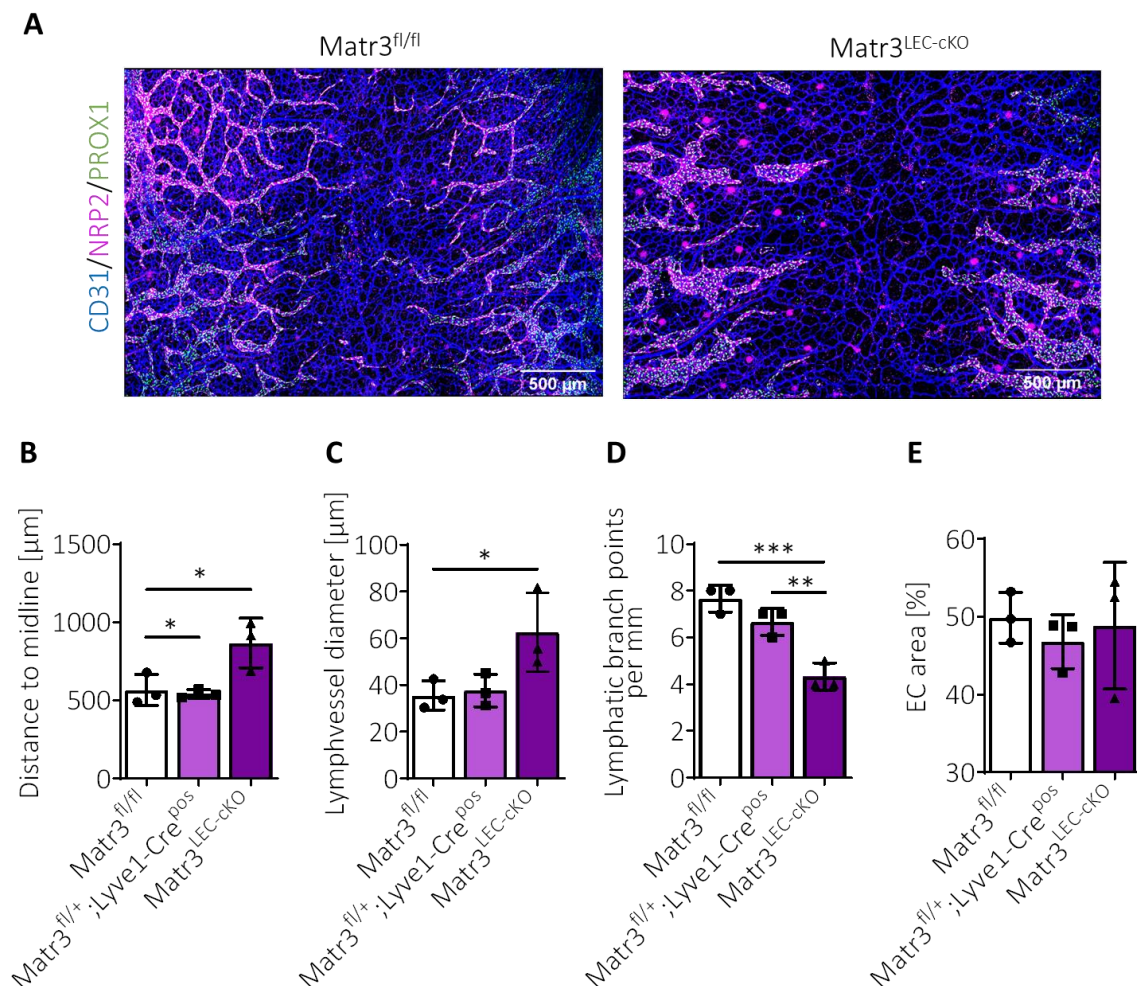
Figure 19 Matr3[LEC-cKO] embryos exhibit an abnormal dermal lymphatic vessel formation

A Confocal images of E15.5 whole-mounted, anterior dorsal skin with indicated genotypes. Skins were immunolabeled with CD31 (blue), PROX1 (green) and NRP2 (magenta) antibodies. **B** Quantification of the distal migration front, defined as the distance to closure starting laterally from the lymphatic tip cells (n=3). **C** Quantification of the average lymph vessel diameter in μm (n=3). **D** Lymphatic network branching analysis,

assessed as lymphatic branch points per mm vessel length (n=3). **E** Coverage in percentage of the skin area covered by CD31^{pos} BECs. **B-E** Data represent the mean ± SD. Two-way ANOVA with Tukey's multiple comparisons test. * P < 0.05; **P < 0.01; ***P < 0.001.

Interestingly, postnatally surviving Matr3$^{LEC-cKO}$ maintain a lymphatic phenotype. The postnatal remodeling of the lymphatic vasculature in surviving Matr3$^{LEC-cKO}$ was examined in the outer ear skin of 21-day-old pups (P21). Whole-mount IF staining with LYVE1 revealed a diminished lymphatic vessel coverage in Matr3$^{LEC-cKO}$ ears (**Figure 20**A+B). Similar to the embryonic time point, LEC-specific loss of Matrin3 results in a reduced branching of juvenile lymphatic vessels, in comparison to the highly branched lymphatic network in littermate controls (**Figure 20**C). In contrast to the embryonic state, the diameter of lymphatic vessels of juvenile Matr3$^{LEC-cKO}$ is not enlarged compared to littermate controls (**Figure 20**D). Taken together, the LEC-specific loss of MATR3 reduces the density of lymphatic vessels in embryonic and postnatal Matr3$^{LEC-cKO}$ skin models, demonstrating that Matrin3 plays a crucial role in embryonic and postnatal lymphangiogenesis.
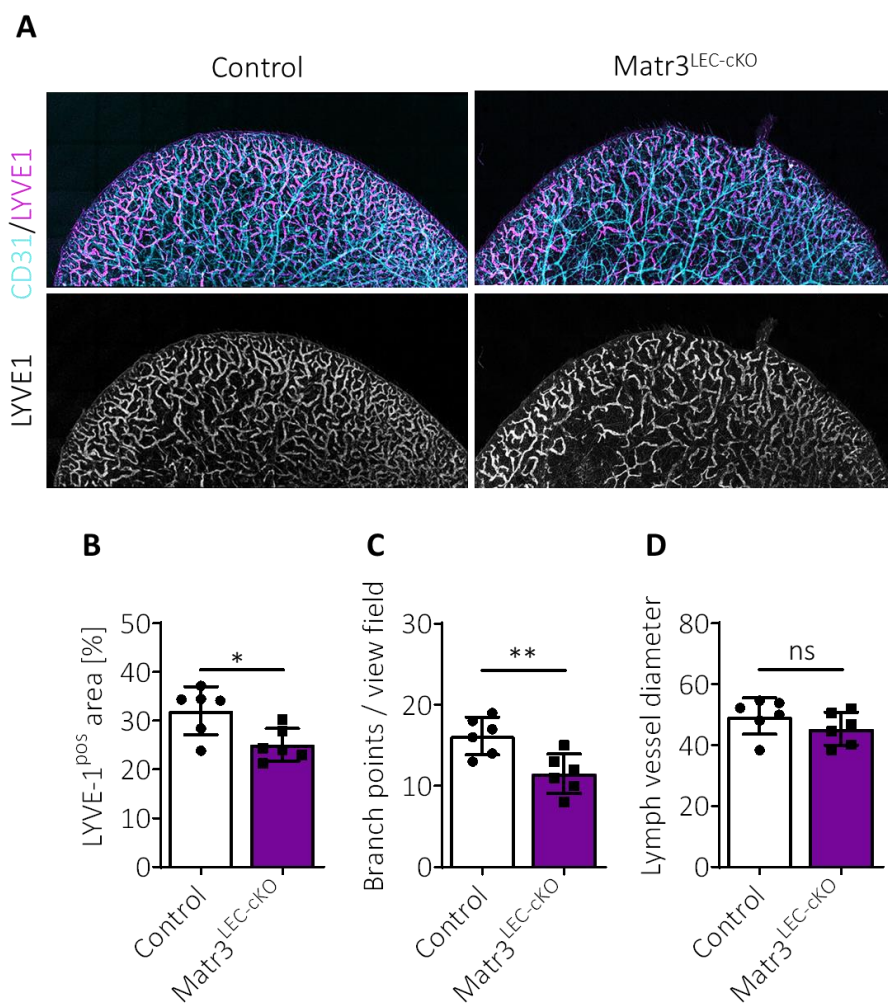
Figure 20 Juvenile Matr3$^{LEC-cKO}$ mice maintain a lymphatic phenotype

A Whole-mount IF staining with LYVE1 and CD31 of outer ear skin from P21 Matr3[LEC-cKO] and littermate controls. Ear skin immunolabeled with CD31 (cyan) and LYVE1 (magenta) antibodies. Single channel in grey shows LYVE1 staining only. **B-D** Quantitative analysis for Lyve[pos] area (B) lymphatic branch points (C) and the lymphatic vessel diameter (D) in the outer ear skin of P21 Matr3[LEC-cKO] and littermates (n=6). Data represent the mean ± SD. Two-tailed paired t-test. * P < 0.05; **P < 0.01; ns: not significant.

Knockdown of *Matr3* in human primary lymphatic endothelial cells elevates proliferation

Since the number of primary embryonic, dermal BEC and LEC is limited, we established a cell culture model enabling us to conduct further assays. Both, human primary BECs (HUVEC) and LECs (HDLEC) are widely used for cell culture studies. To prove that both human cell lines resemble the endothelial cell-subtype specific phenotypes from MATR3-deficient mice, siRNA-mediated *hMATR3* knockdown was performed. The knockdown efficiency over time was determined by IF staining (24h, 48h, 72h; data not shown), revealing that hMATR3 protein was nearly undetectable 72h post transfection (**Figure 21**A). Therefore, this time point was selected for further analysis. Interestingly, siRNA-mediated *hMATR3* knockdown results in an elevated proliferation rate in HDLECs indicated by Ki67 staining, whereas proliferation of HUVECs remains unaltered. (**Figure 21**B+C). This result reinforces the conclusion that loss of Matrin3 increases proliferation of LECs but not BECs.
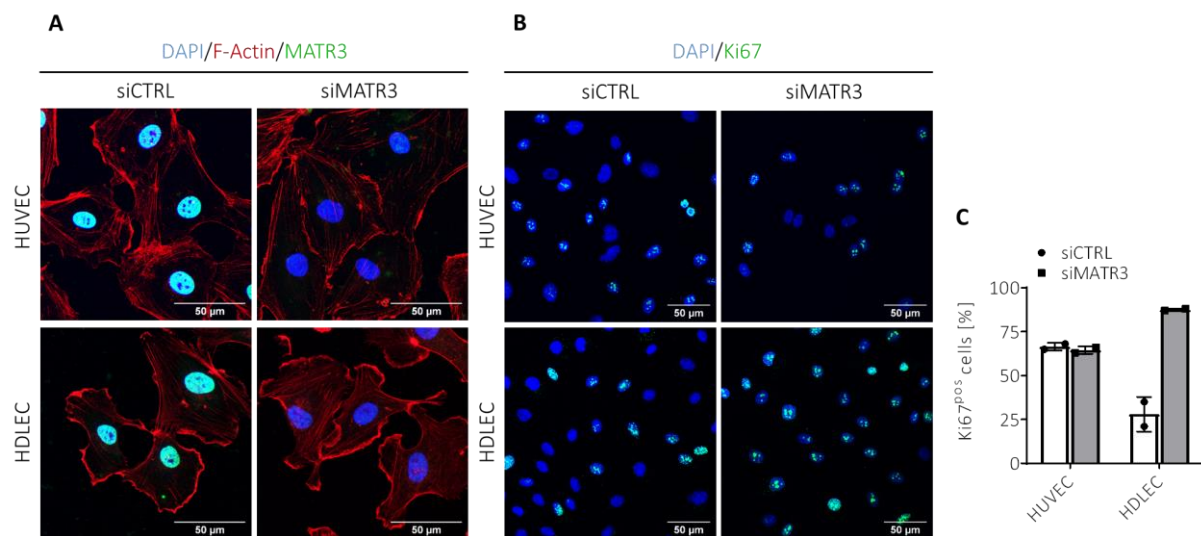
Figure 21 siRNA-mediated knockdown of *hMATR3* leads to increased proliferation in HDLEC but not HUVEC

IF stainings of HUVEC and HDLEC 72h after transfection with either siCTRL or sihMATR3. Co-staining with **A** DAPI (blue), F-Actin (red) and either anti-MATR3 (green) or **B** the proliferation marker anti-Ki67 (green). **C** Proliferation rate of HUVEC and HDLEC upon siRNA-mediated knockdown of *hMATR3*, *given* as the percentage of Ki67^{pos} cells. Preliminary result (n=2).

Global loss of *Matr3* does not affect dermal pericyte coverage of blood vessels

Blood vessels are composed of two interacting cell types*:* endothelial cells and pericytes. Pericytes cover a majority of the endothelial cell surface and play an important role in maintaining cell vessel integrity. In the developing skin, pericytes exhibit various shapes resulting in a semicircular geometry at E15.5 [140]. Co-staining with smooth muscle α-actin (αSMA) and Neural/glial antigen 2 (NG2) allows discrimination of pericytes and vascular smooth muscle cells (vSMC). Pericytes are positive for NG2 (NG2 single-positive; **Figure 22**, see arrows) whereas vSMC are marked by both, NG2 and αSMA.
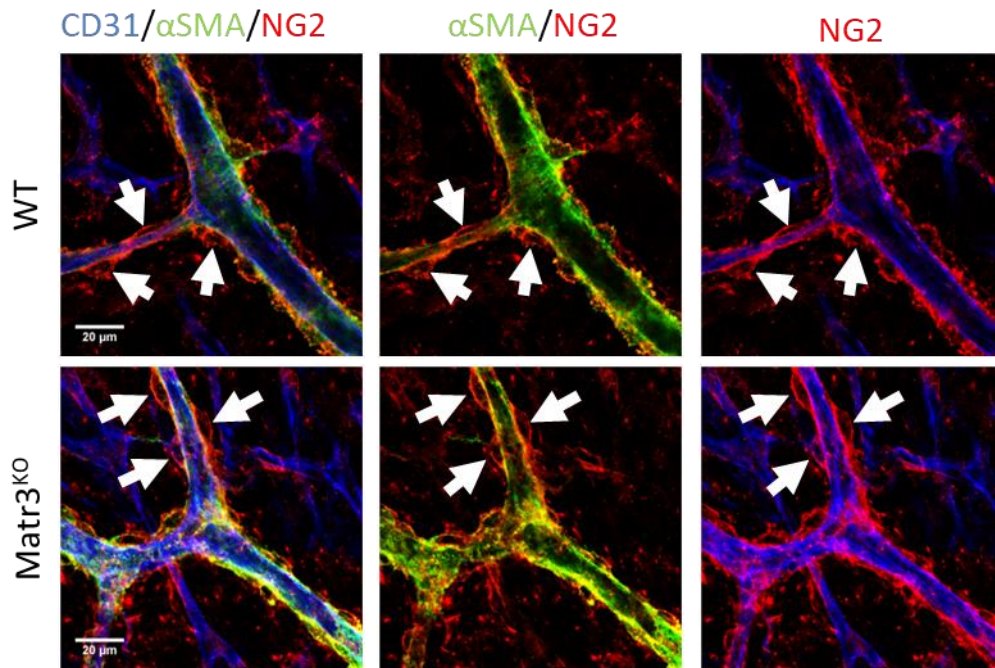
Figure 22 Antibody staining to discriminate smooth muscle cells and pericytes

Counterstaining of embryonic back skins with CD31 (blue), αSMA (green) and NG2 (red). Pericytes are stained by NG2 but not αSMA (see arrows). Scale bar: 20µm.

To examine whether developing pericytes are affected upon *Matr3* depletion, whole-mount embryonic dorsal skins of MATR3^{KO} and littermate controls were stained with the previously described antibody combination (**Figure 23**A). Quantification revealed comparable numbers of three to six pericytes per 100µm vessel length in E15.5 skins of MATR3^{KO} and littermate controls (**Figure 23**B), indicating an unaffected pericyte coverage at this embryonic stage.
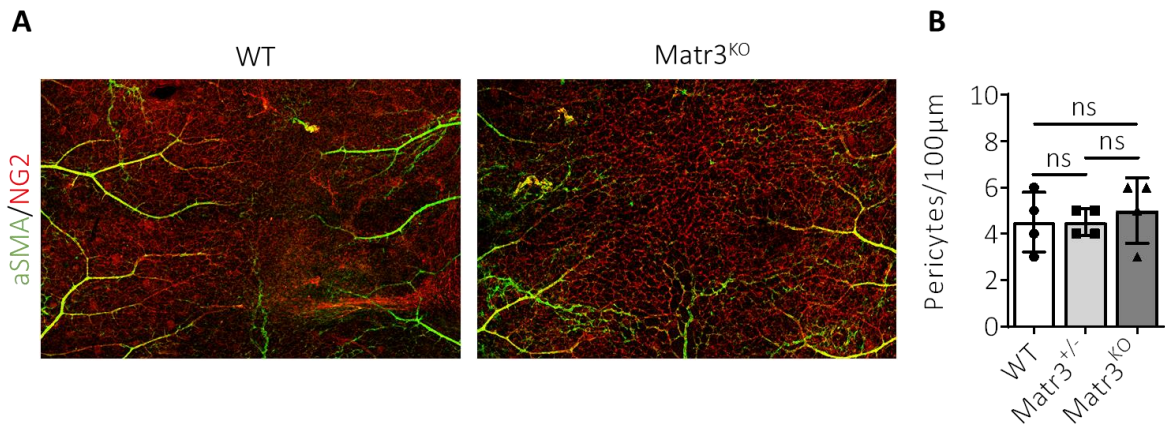
Figure 23 Pericyte coverage is unaffected in MATR3[KO] skins

A Whole mount confocal images of embryonic skins from WT and Matr3[KO] stained with antibodies against smooth muscle α-actin (αSMA, green) and NG2 (red). **B** Average number of pericytes per 100μm vessel length from no less than 3 capillaries of Matr3[KO] and littermate controls (n=4). Data represent the mean ± SD. Two-way ANOVA with Tukey's multiple comparisons test. ns = not significant.

Global loss of *Matr3* results in diminished trabeculation and increased cardiac stress response
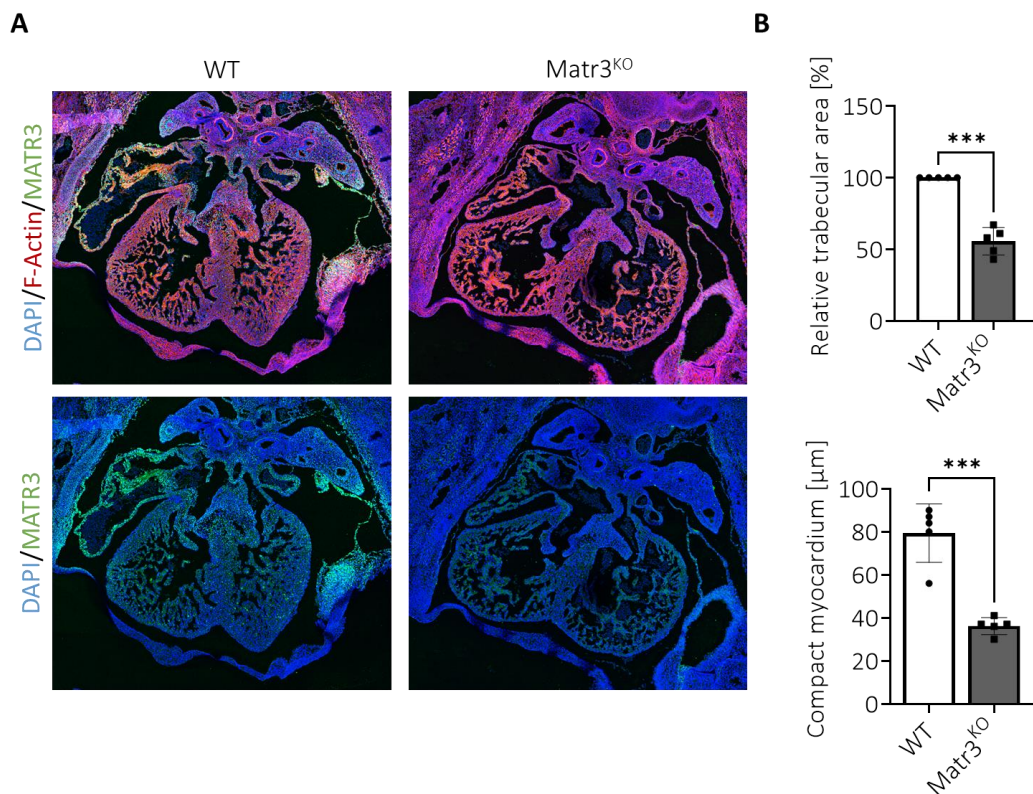
Figure 24 Decreased ventricular trabeculation and compaction in embryonic Matr3[KO] hearts

A Representative IF staining showing cryo sections of E14.5 hearts from wild type and global Matr3[KO]. Sections were stained for DAPI (blue), F-Actin (red) and anti-MATR3 (green). **B** Quantification of the relative trabecular

area and the thickness of the compact myocardium using H&E-stained cryo heart sections (images not shown, n=5). Data represent the mean ± SD. Two-tailed paired t-test. ***P < 0.001.

Although loss of *Matr3* in endothelial cells results in malformation of the lymphatic vasculature and edema formation, we cannot completely rule out a contribution of heart failure to edema formation. Therefore, the potential contribution of the heart phenotype was subsequently assessed. The constitutive loss of MATR3 (**Figure 24**A) manifests in diminished ventricular trabeculation, concomitant with a reduced thickness of the compact myocardium at E14.5 (**Figure 24**B).

Global *Matr3* inactivation was further confirmed on RNA and protein level using total hearts, which comprise multiple cell types such as cardiomyocytes, smooth muscle, and endothelial cells, pericytes and others. *Matr3* expression in Matr3^{KO} hearts was barely detectable by qRT-PCR (**Figure 25**A) and MATR3 protein is completely absent shown by Western blotting (**Figure 25**B). Notably, Matr3^{KO} hearts display increased levels of cardiac stress response genes such as the natriuretic peptide precursor A (*Nppa*) and B (*Nppb*) as well as skeletal α-actin (*Acta1*; **Figure 25**A). To assess whether loss of *Matr3* results in an altered expression of the paralog *Rbm20* in the heart, qRT-PCRs as well as Western blots were performed. However, we observed no significant upregulation of *Rbm20* expression (**Figure 25**A) or RBM20 protein levels (**Figure 25**B) in Matr3^{KO} hearts.
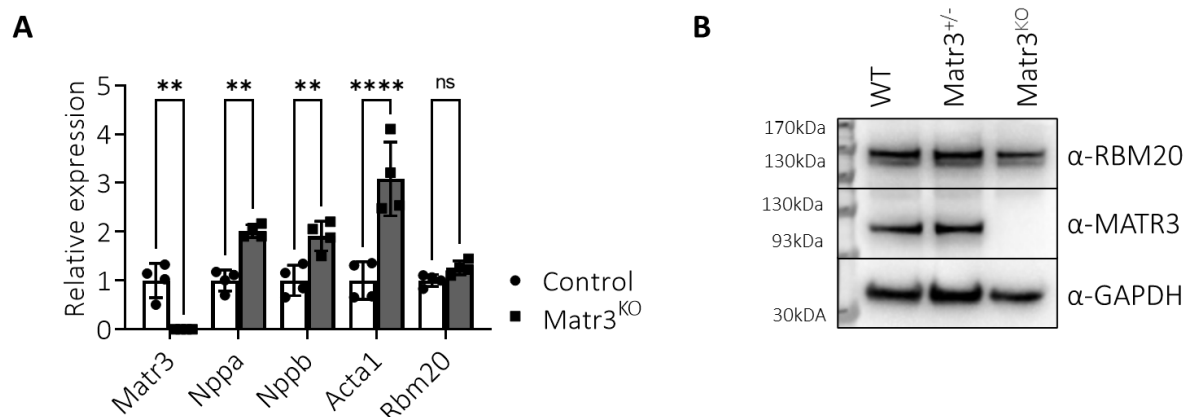
Figure 25 Knockout validation using Matr3^{KO} hearts

A qRT-PCR analysis of cardiac stress response genes in Matr3^{KO} and control hearts (n=4). Data represent the mean ± SD. Two-way ANOVA with Bonferroni's multiple comparisons test. **P < 0.01; ****P < 0.0001. ns = not significant. **B** Representative Western blotting of heart lysate of E15.5 embryos with indicated genotypes.

To gain deeper insights into the underlying mechanisms of the embryonic heart phenotype, whole transcriptome sequencing of E14.5 wild type and Matr3^{KO} hearts (n=2) was performed. In total, transcriptome profiling identified 585 differentially expressed genes (DEGs), including 438 upregulated genes and 147 downregulated genes in Matr3^{KO} hearts (log2FC

Matr3-KO/WT). *Matr3* levels are significantly reduced in Matr3[KO] hearts (**Figure 26**A), whereas both predicted paralogs *Zfpn638* and *Rbm20* are not dysregulated (**Figure 26**A).

The identified DEGs were further analyzed using GO and KEGG enrichment to determine their potential functions and pathways. The top 10 significantly enriched GO terms and KEGG pathways contain collagen fibril organization and extracellular matrix-receptor interaction, including multiple upregulated genes related to collagens (**Figure 26**B), indicating increased collagen deposition in Matr3[KO] hearts. In addition, loss of *Matr3* leads to dysregulation of several genes encoding ion channels (**Figure 26**C), which might cause cardiac conduction abnormalities. The KEEG Pathway for dilated cardiomyopathy (DCM) revealed changes in differential gene expression, e.g., for several sarcomeric proteins such as Titin, MYH6/MYH7, TNNT2, MYBPC3, and Desmin (**Figure 26**D, see arrows). Taken together, embryonic hearts of constitutive *Matr3* knockout hearts exhibit altered expression of multiple genes related to numerous aspects of heart failure, resulting in reduced cardiac trabeculation. Since in a global Matr3[KO] multiple cardiac cell types might contribute to the observed heart phenotype, a cardiomyocyte-specific (conditional) knockout model was subsequently analyzed.
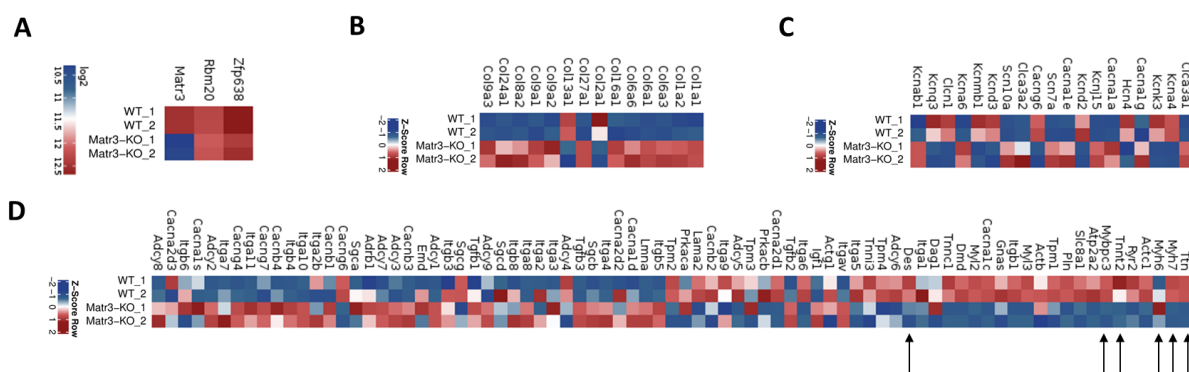
Figure 26 Transcriptome profile of embryonic Matr3[KO] hearts

Heatmaps showing the expression of **A** the predicted paralogs, **B** regulated collagens and **C** regulated ion channels.
D Regulated genes from "DCM" KEEG pathway. Colored bars indicate the expression levels. The red blocks represent increased expression, and blue blocks represent genes with decreased expression levels.

Ablation of *Matr3* in cardiomyocytes leads to dilated cardiomyopathy with impaired systolic function resulting in premature death

To confirm that the cardiac phenotype in Matr3[KO] originated from specific loss of MATR3 in cardiomyocytes, a cell type-specific conditional Matrin3 knockout mouse model (Matr3-cKO) was generated. Matr3^{fl/fl} mice were crossed with cardiomyocyte-specific *Xenopus laevis* myosin light-chain 2 (XMLC2)–Cre transgenic mice [141], which drives Cre recombinase activity exclusively in cardiomyocytes throughout early embryonic development and

adulthood. XMLC2-Cre was chosen, because murine *Matr3* is highly expressed in the developing heart and gradually declined during maturation [94]. Isolated cardiomyocytes from Matr3-cKO hearts display strongly decreased *Matr3* mRNA levels (**Figure 27**A), indicating highly efficient recombination. Western blot analysis of total heart extracts revealed a significant decrease (**Figure 27**B), whereby the remaining MATR3 protein originates from non-cardiomyocytes such as fibroblasts, endothelial cells, and other cell types.
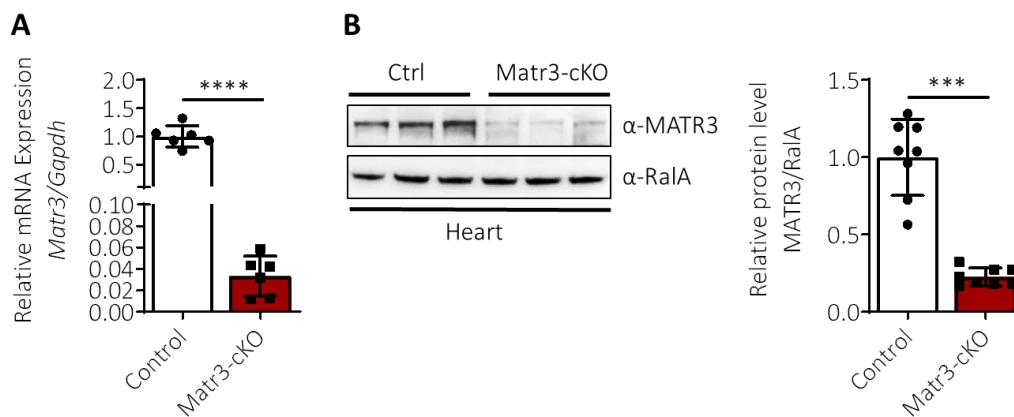
Figure 27 Cardiomyocyte-specific depletion of *Matr3* mediated by XMLC2-Cre is highly efficient

Validation of cardiomyocyte-specific *Matr3* knockout. **A** qRT-PCR of isolated cardiomyocytes from 3-week-old mice with indicated genotypes (n=6). **B** Representative Western blotting (n=3) and quantification using heart lysate of 3-week-old mice (n=8). RalA serves as loading control. **A+B** Data represent the mean ± SD. Two-tailed paired t-test. ***P < 0.001. ****P < 0.0001.

Survival analysis of the conditional knockout mouse line revealed that the majority of Matr3-cKO die within the first month post birth with a median survival of 13 days (**Figure 28**A). Notably, successive backcrossing to the C57/Bl6J background strongly enhances the cardiac phenotype, resulting in premature mortality. To rule out embryonic lethality, E14.5 and E18.5 litters were examined, which showed the expected outcome of approximately 25% cKO embryos at both time points (**Figure 28**B, in red), with an average litter size of 9±1 at E14.5 and 8±2 at E18.5. No edema formation was observed in E14.5 or E18.5 Matr3-cKO, indicating that heart malformations based on cardiomyocyte-restricted *Matr3* ablation are not sufficient to induce subcutaneous edema in embryos. At the age of two weeks, both heart-to-body weight (HW/BW) and heart weight-to-tibial length (HW/TL) ratios were significantly increased in Matr3-cKO mice compared to littermate controls (**Figure 28**C). The body weight-to-tibial length (BW/TL) was highly variable for Matr3-cKO pups.
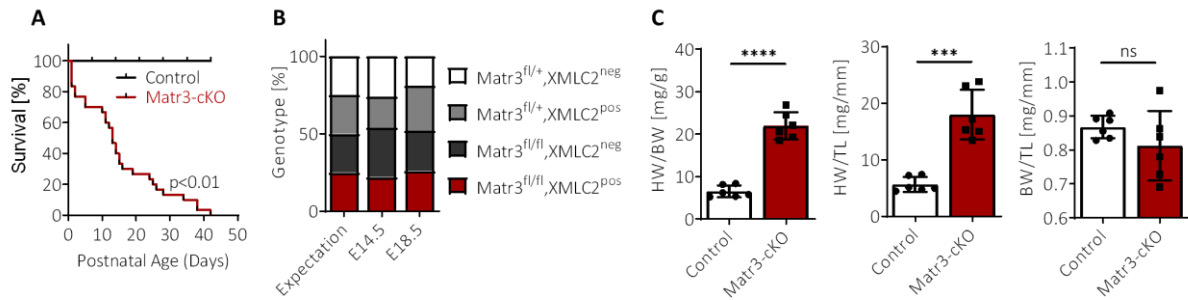
Figure 28 Cardiomyocyte-specific loss of *Matr3* results in postnatal death

A Kaplan-Meier survival curves of Matr3-cKO mice (n=35) and littermates. Matr3-cKO median survival is 13 days (p<0.01). **B** Viability of Matr3-cKO embryos at E14.5 and E18.5 (n=5 litters for each time point). **C** Graphs depicting the BW/TL, HW/TL and HW/BW ratios of 2-week-old Matr3-cKO and control mice (n=6). BW/TL body weight to tibial length ratio, HW/TL, heart weight to tibial length ratio and HW/BW, heart weight to body weight ratio. Data represent the mean ± SD in C. Two-tailed paired t-test. ***P < 0.001; ****P < 0.0001; ns: not significant.

Gross morphological analysis revealed that Matr3-cKO hearts progressively enlarged with age and developed dilated cardiomyopathy. *Matr3*-deficient hearts were morphologically distinguishable from littermate control hearts, e.g. **Figure 29**A shows a representative Matr3-cKO heart at the age of 4 weeks with 315.5mg compared to the control heart with 108.8mg. H&E-stained heart sections depicted ventricular chamber enlargement and reduced ventricular thickness at postnatal day 10 Matr3-cKO heart compared to littermate controls (**Figure 29**B). Approximately 20% of juvenile Matr3-cKO mice had either left atrial or left ventricular thrombi (**Figure 29**B+C). From 10 to 20 days post birth, Matr3-cKO mice display a decrease in left ventricular and septum wall thickness (**Figure 29**D+E). Taken together, these results demonstrate that MATR3 is required for physiological cardiac growth and function.

In addition to the morphological analysis, cardiac MRI was applied to examine cardiac physiology and function of the Matr3-cKO during the postnatal phase. The four-chamber views indicated that Matr3-cKO mice develop progressive cardiomyopathy with left ventricular dilation and ventricular wall thinning (**Figure 29**A+B). At the respective time points, no significant difference in body weight was recorded (**Figure 30**C), whereas an increasing LV mass, as well as LV mass to BW ratio, was observed (**Figure 30**D+E). As a result of the chamber enlargement, ESV and EDV are increased on average (**Figure 30**F+G). By the age of 3 weeks, SV (**Figure 30**H) and CO (**Figure 30**I) of the MATR3-cKO pups are modestly increased, even though it is not statistically significant. In addition, the left ventricular ejection fraction (LVEF, **Figure 30**K) is transiently reduced two weeks post birth, although this is compensated one week later due to the progressive dilation of the ventricles.

Despite this temporary compensatory response through ventricular dilation, the loss of Matrin3 results in heart failure.
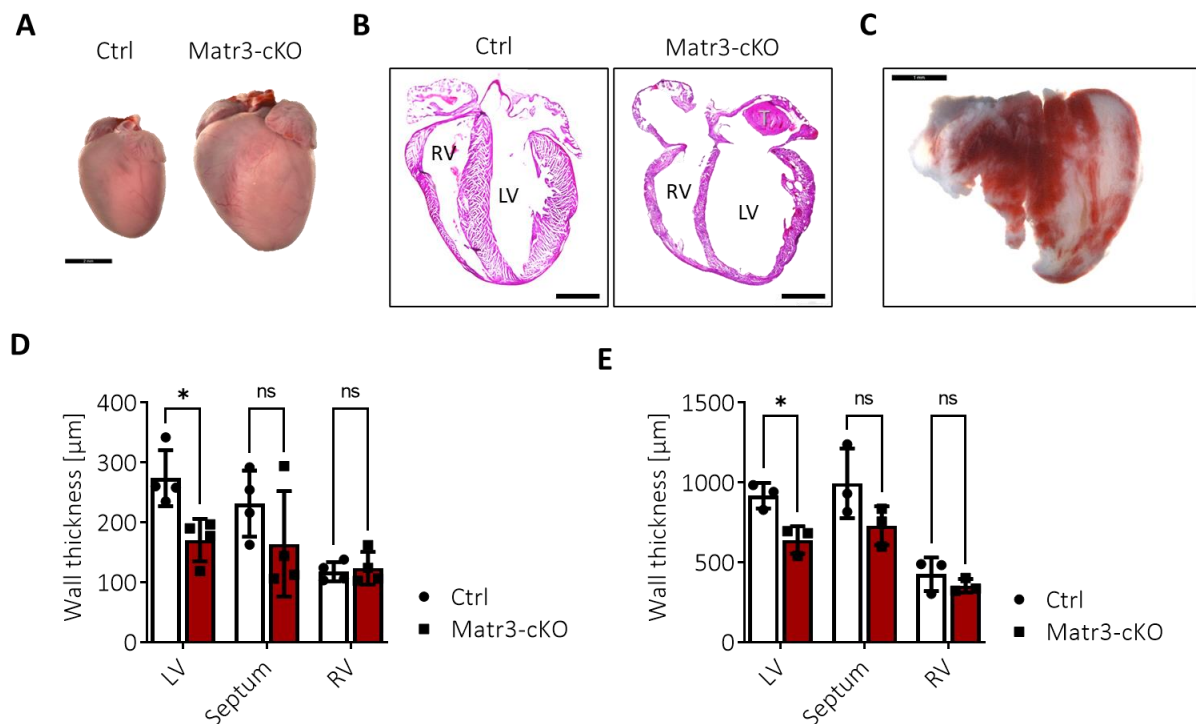
Figure 29 Characterization of ventricular dilation and wall thinning in juvenile Matr3-cKO mice

A Gross morphology of hearts form 1 month-old Matr3-cKO and littermate control. Scale bar: 2mm **B** Representative H&E staining of P10 hearts from control and Matr3-cKO. LV = left ventricle, RV = right ventricle, T = thrombus. Scale bar: 1mm **C** Thrombus isolated from the LV of a 1-month-old Matr3-cKO mutant during enzymatic digestion. Scale bar: 1mm. **D+E** Quantification of wall thickness at P10 (D, n=4) and P20 (E, n=3). Data represent the mean ± SD. Two-way ANOVA with Šídák's multiple comparisons test. ns = not significant, * P < 0.05.
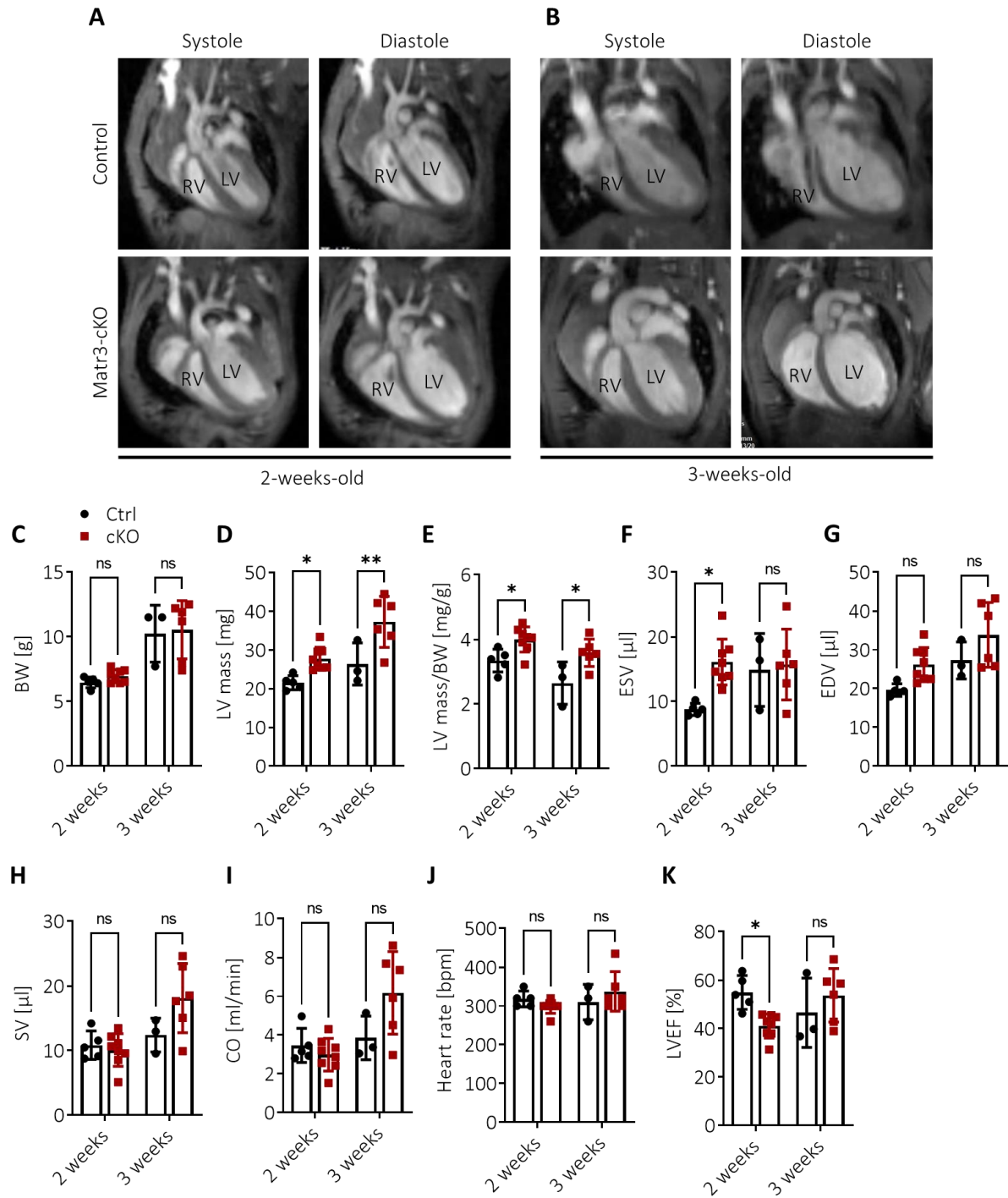
Figure 30 Systolic heart failure of Matr3-cKO hearts

A+B Cardiac MRI images of four-chamber view in end-systole and end-diastole phases of 2- (**A**) and 3-week (**B**) old Matr3-cKO and control littermates. RV: right ventricle, LV: left ventricle. **C-I** Quantification for cardiac magnetic resonance imaging (MRI) of Matr3-cKO and control littermates at the indicated time points: **C** Body weight (BW). **D** LV mass, calculated by the average of end-systolic and end-diastolic mass of the left ventricle. **E** LV mass to body weight ratio. **F+G** End-systolic and end-diastolic volume of the left ventricle. **H** Stroke volume (SV) and **I** Cardiac output (CO), which is the product of the heart rate and SV. J Heart rates in beats per minute. **K** Left ventricular ejection fraction (LVEF). **C-I** Data represent the mean ± SD. Two-way ANOVA with Šídák's multiple comparisons test. ns = not significant, * P < 0.05, **P < 0.01. Comparison only between groups, not within groups of two time points.

Postnatal deletion of *Matr3* does not affect heart morphology and function

In addition to the early ablation of *Matr3* using the XMLC2-Cre, *Matr3* was depleted in postnatal cardiac and skeletal muscle cells (MC) using the MCK-Cre [142]. MCK-Cre/Matr3 mice develop skeletal muscular atrophy (data not shown) and die around 8 weeks after birth (**Figure 31**A). Interestingly, heart morphology (**Figure 31**C+D) and function (**Figure 31**E) are not altered before death, although MCK-Cre-mediated depletion of *Matr3* is highly efficient in cardiomyocytes (**Figure 31**B). These data reveal that MATR3 is mainly required for embryonic cardiogenesis rather than for postnatal cardiomyocyte maturation.
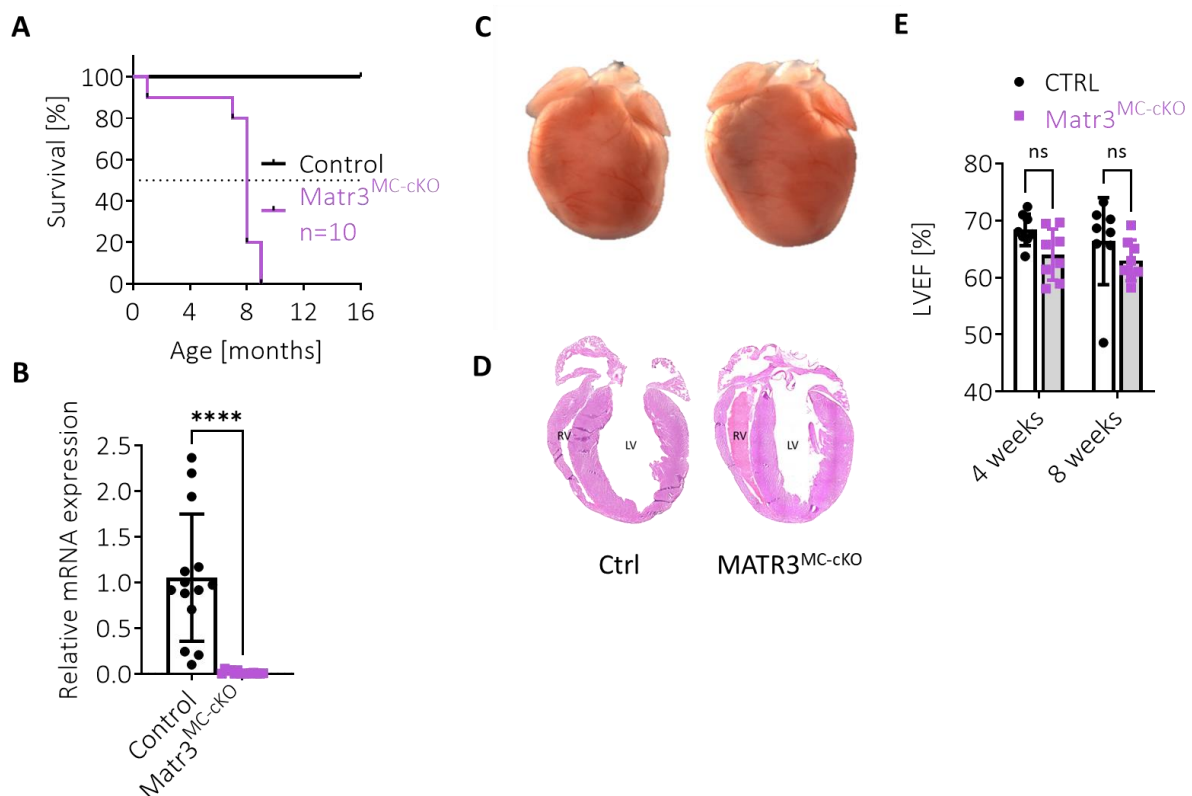
Figure 31 Postnatal *Matr3* knockout does not lead to heart failure

A Kaplan-Meier survival curves of Matr3MC-cKO mice and littermates (n=10), revealing that knockout mice have a median survival of 8 weeks. **B** Validation of MCK-Cre driven *Matr3* knockout in isolated cardiomyocytes using qRT-PCR (n=14). Data represent the mean ± SD. Two-tailed paired t-test. ****P < 0.0001. **C+D** Gross morphology (C) and H&E stained cryosections (D) of hearts form 2-month-old Matr3MC-cKO mice and littermate control. RV: right ventricle, LV: left ventricle. **E** Left ventricular ejection fraction (LVEF) of Matr3MC-cKO mice and littermates 4- and 8-weeks post birth (n=8). Data represent the mean ± SD. Two-way ANOVA with Šídák's multiple comparisons test. ns = not significant.

Matr3-deficient cardiomyocytes are hypertrophic

To assess phenotypic alterations in Matr3-cKO cardiomyocytes, cardiomyocytes isolated from 3-week-old juvenile mice were analyzed in respect to morphology and cellular surface

area in combination with MATR3 and ACTN2 immunostaining. Representative images indicate the complete absence of MATR3 in *Matr3*-deficient cardiomyocytes (**Figure 32**A), confirming highly efficient recombination via the XMLC2-Cre. Quantification of size revealed hypertrophic growth of *Matr3*-depleted cardiomyocytes, since the mean size ± SD was $1983 \pm 406 \ \mu m^2$ in Matr3-cKO compared to $1573 \pm 320 \ \mu m^2$ of control cardiomyocytes (**Figure 32**B). Notably, cardiomyocyte length, as well as width, were extended upon *Matr3* knockout (**Figure 32**C+D). On the molecular level, cardiac hypertrophy marker such as *Nppb*, *Myh6* as well as *Myh7* were significantly upregulated in isolated Matr3-depleted cardiomyocytes (**Figure 32**D). Since *Myh6* levels remained unaffected, the mRNA expression ratio shifts from the adult *Myh6* to the fetal *Myh7* in juvenile Matr3-cKO cardiomyocytes, indicating a prolongation of the fetal gene program in response to pathological hypertrophy.
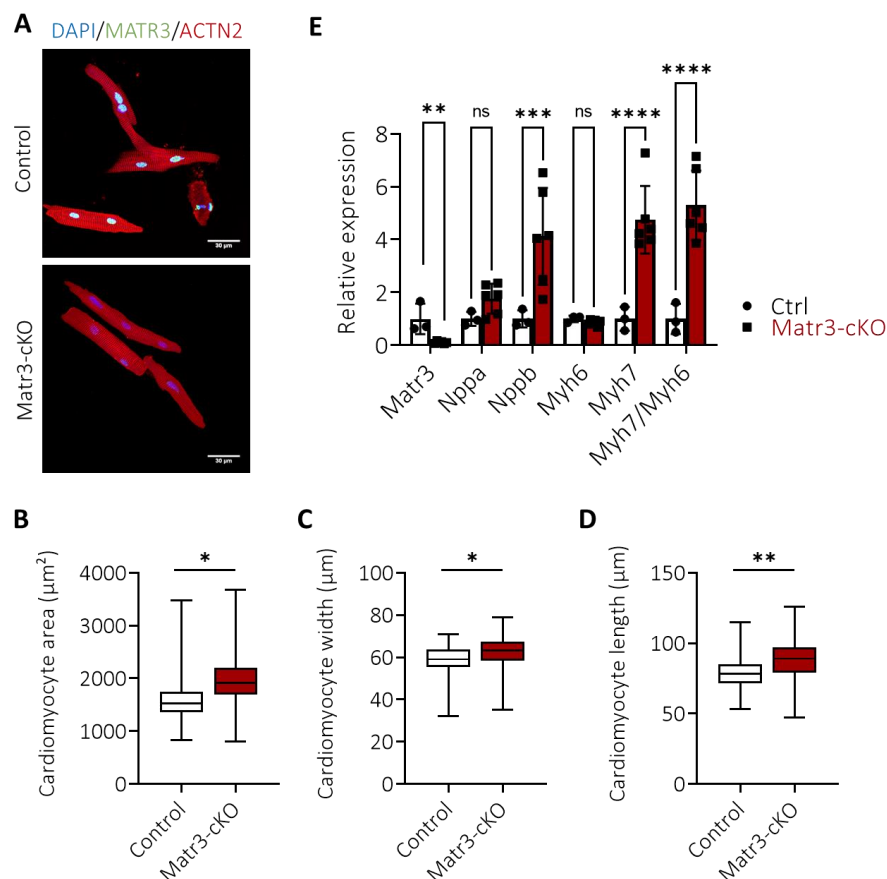
Figure 32 Cardiomyocyte hypertrophy upon *Matr3* loss

A Representative confocal images of isolated cardiomyocytes form control and Matr3-cKO mice (3-week-old) immunolabeled with anti-ACTN2 (red) and anti-MATR3 (green). Note the complete absence of MATR3 staining (in green) in Matr3-cKO cardiomyocytes. Scale bar: 30μm. **B** Quantification of mean areas of isolated cardiomyocytes shown as Box-Whisker-Plot (min to max). Rod-shaped cardiomyocytes (>1500 from four individuals per genotype) were randomly selected for size measurements. **C+D** Quantification of cardiomyocyte width (C) and length (D) from isolated Matr3-cKO and control cardiomyocytes depicted as Box-Whisker-Plot (min to max). **B-D** Two-tailed paired t-test of mean size from n=4 individuals per genotype. * $P < 0.05$; **$P < 0.01$

E Relative mRNA expression levels of the hypertrophy markers determined by qRT-PCR using isolated cardiomyocytes from 3-week-old Matr3-cKO (n=6) and littermates (n=3). Data represent the mean ± SD. Two-way ANOVA with Šídák's multiple comparisons Test. ns = not significant, **P < 0.01; ***P < 0.001; ****P < 0.0001.

Concomitant inactivation of *Matr3* and *Rbm20* results in neonatal lethality due to reduced ventricular trabeculation and compaction

To analyze whether MATR3 and RBM20 exert overlapping functions in cardiomyocytes, dKO mice were generated by combining the constitutive RBM20^{KO} and conditional MATR3-cKO mutant strains. The knockout in total dKO hearts (Rbm20$^{KO/KO}$, Matr3$^{fl/fl}$, XMLC2-Cre^{pos}) was confirmed by qRT-PCR (**Figure 33**A). Again, the remaining *Matr3* mRNA originates from non-cardiomyocytes. dKO embryos were obtained in the expected Mendelian ratios of 12,5% (1 dKO out of 8 embryos) at E14.5 and E18.5 but not P0 (**Figure 33**B), indicating that dKO pups die around birth. In order to get a deeper insight, the heart phenotypes of RBM20^{KO}, Matr3-cKO and double-knockout (dKO) embryos were compared. At E14.5, hearts of Matr3-cKO as well as dKO exhibit hypotrabeculation and ventricular wall thinning (**Figure 33**C); however, trabeculation is still more pronounced in Matr3-cKO hearts compared to dKOs (**Figure 33**D).
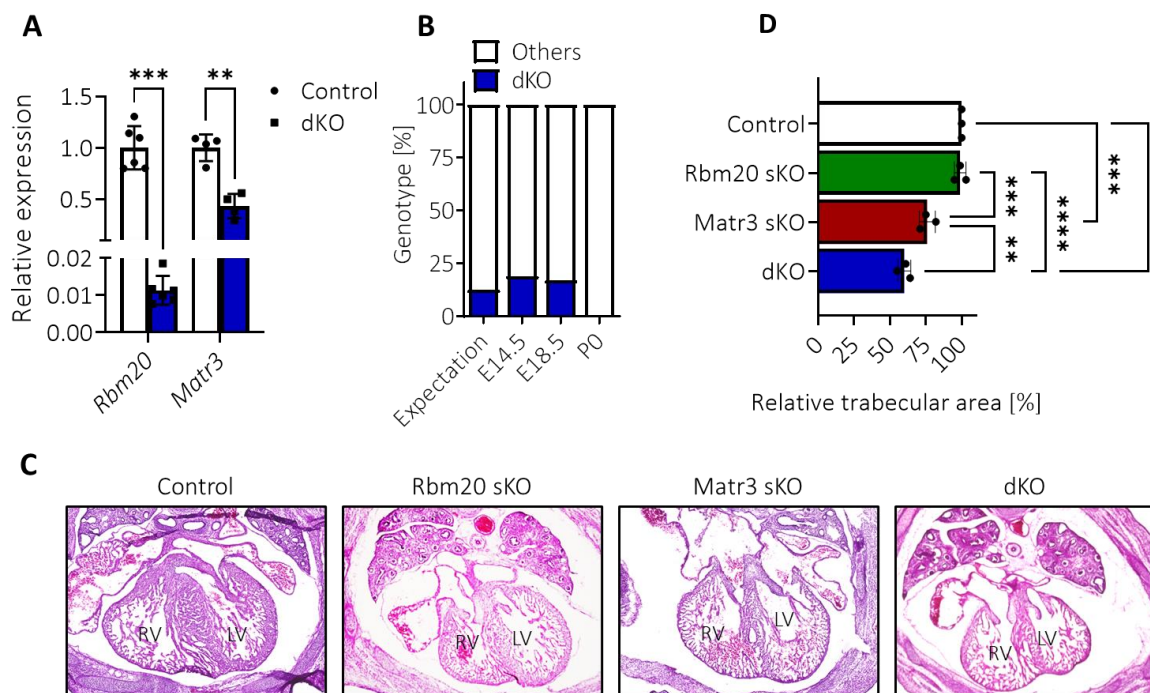
Figure 33 Trabeculation phenotype of dKO hearts in comparison to *Matr3* and *Rbm20* single knockouts

A qRT-PCR for *Rbm20* (n=6) and *Matr3* (n=4) of E14.5 hearts from dKO and control littermates. Data represent the mean ± SD. Two-way ANOVA with Bonferroni's multiple comparisons test. **P < 0.01; ***P < 0.001. **B** Survival of dKO, evaluated from 3 individual litters at E14.5, E18,5 and P0. "Others" include all others genotypes resulting from the breeding including RBM20^{KO} and Matr3-cKO single knockouts. **C** Representative H&E staining of E14.5 hearts from control, *Rbm20* and *Matr3* single as well as double knockout. **D** Quantification

of the relative trabecular area at E14.5 of single and dKO hearts (n=3). Data represent the mean ± SD. Two-way ANOVA with Tukey's multiple comparisons test. **P < 0.01; ***P < 0.001; ****P < 0.0001. *Genotypes:* controls: Rbm20$^{KO/wt}$, Matr3$^{fl/fl}$, XMLC2-Cre^{neg} or Rbm20$^{KO/wt}$, Matr3$^{fl/wt}$, XMLC2-Cre^{pos}; Matr3 sKO: Rbm20$^{KO/wt}$, Matr3$^{fl/fl}$, XMLC2-Cre^{pos}; RBM20 sKO: Rbm20$^{KO/KO}$, Matr3$^{fl/wt}$, XMLC2-Cre^{neg}; dKO: Rbm20$^{KO/KO}$, Matr3$^{fl/fl}$, XMLC2-Cre^{pos};

Transcriptomic changes in *Rbm20* and *Matr3* single and double knockout hearts

To gain further molecular and mechanistic insights, whole transcriptome analysis of single, double KO and C57BL/6J hearts at E14.5 was performed. Heat map (**Figure 34**A) as well as principal components analysis (PCA; **Figure 34**B) of gene expression data indicate variables in this data set, revealing two discrete clusters: First, a cluster comprising WT and RBM20^{KO} and a second cluster encompassing Matr3-cKO and dKO. This analysis indicates that *Rbm20*-deficient and wild type embryonic hearts display similar expression profiles, whereas pronounced changes in the transcription profile were observed in Matr3-cKO and dKO. The RNA-seq analysis confirmed knockout of the respective gene(s) (**Figure 34**C+D).
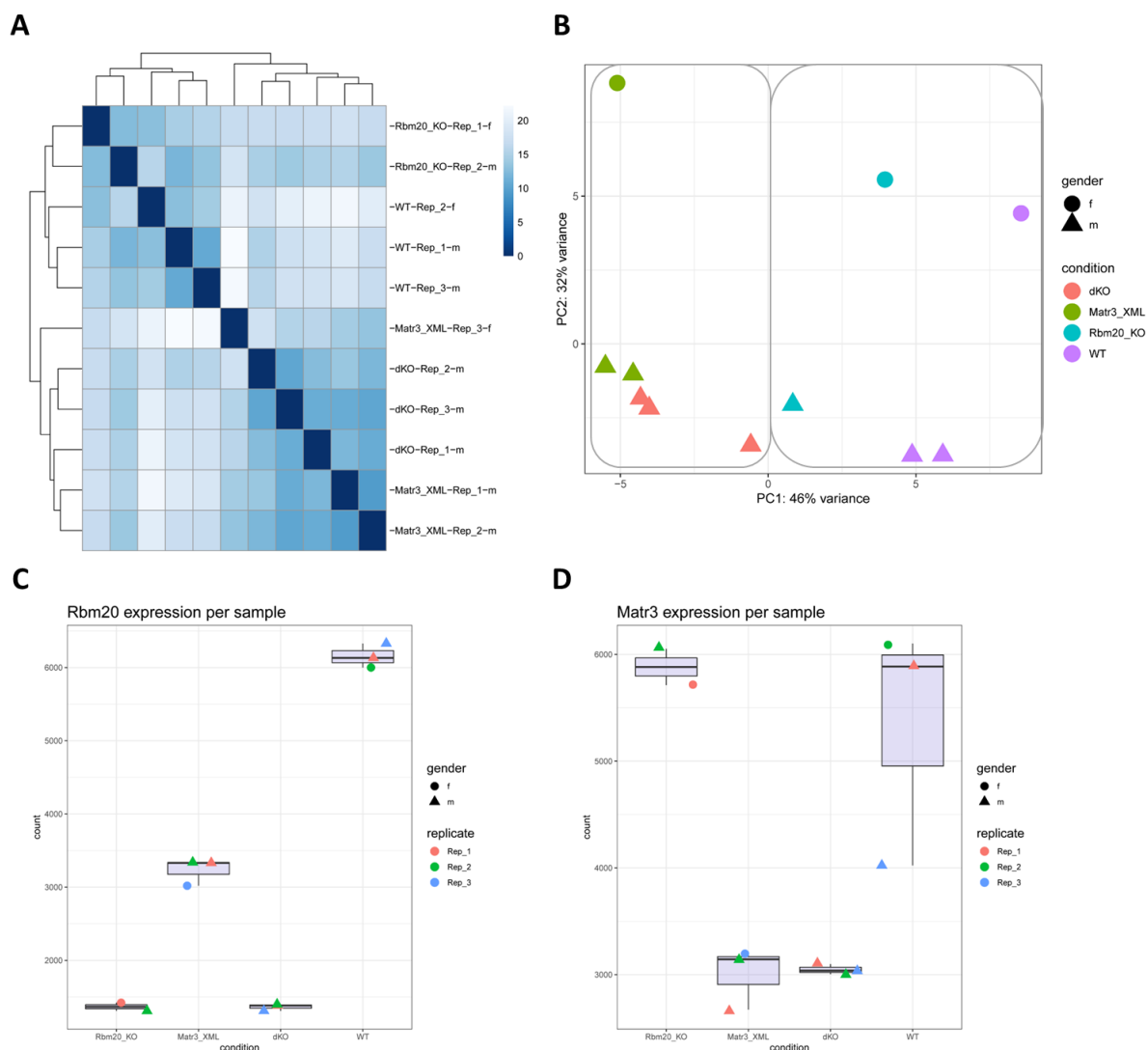
Figure 34 Clustering and principal component analysis of *Rbm20* and *Matr3* single and double knockout samples based on the gene expression data by RNA-Seq.

A Heat map and **B** principal component analysis (PCA) depicting separation of the individual replicates (based on the 500 most deregulated genes). **B** PC1 clusters the samples based on the condition and PC2 separates the samples based on the gender. The gender is determined by the expressions of the *Xist* (X Inactive Specific Transcript) gene and indicated by the shape of data points (dot=female, triangle=male). Data points colored according to the condition. **C+D** Box plots depicting the *Rbm20* and *Matr3* expression (given as count) per sample and condition. Conditions: RBm20^{KO} (n=2), Matr3-cKO (n=3), dKO (n=3), WT= wild type (n=3).

Since neither *Rbm20* nor *Matr3* display altered expression in respect to sex (**Figure 34**C+D), RNA-seq analyzed hearts were not sex-matched. Notably, *Rbm20* was significantly reduced in Matr3-cKO compared to non-littermate WT samples (**Figure 34**C; **Figure 35**B, D) confirming previously reported tight transcriptional regulation during cardiogenesis [93] and highlighting the importance of using littermate controls to determine *Rbm20* gene expression and transcriptomic changes. Additional analysis using proper littermate controls has not proven downregulation of *Rbm20* in neither constitutive Matr3^{KO} (**Figure 25**, page 35 and **Figure 26**, page 36) nor conditional Matr3-cKO hearts (**Figure 35**D).
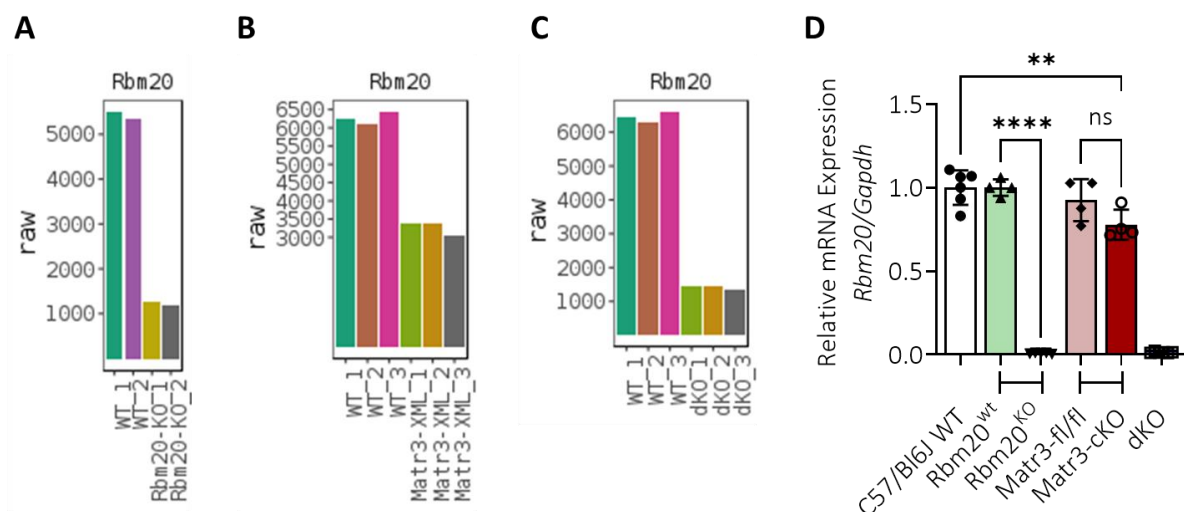
Figure 35 *Rbm20* gene expression in littermate and non-littermate controls

A-C Raw reads for *Rbm20* from RNA-seq data of E14.5 hearts from the indicated KO models: RBM20^{KO} (A, n=2), Matr3-cKO (B, n=3) and dKO (C, n=3). **D** qRT-PCR analysis of *Rbm20* in KO models compared to C57/Bl6J WT hearts (white bar; n≥4). Capped lines indicate littermates: RBM20^{wt} and RBM20 ^{KO} as well as Matr3$^{fl/fl}$ and Matr3-cKO samples were obtained from the same litters. Two-way ANOVA with Dunnett's multiple comparisons test.

The comparison of differentially expressed genes (DEGs) from single and double knockout to wild type hearts revealed major transcriptional differences. Overall, there are major differences between the different mutants in respect to total DEG numbers: Loss of *Rbm20* results in 180 DEGs, whereas Matr3-cKO alters the expression of 2.625 genes and the double knockout results in 1.933 DEGs (**Figure 36**A). A common set of 134 genes was differentially expressed in all KO hearts, whereas Matr3-cKO and dKO share an additional

set of 1438 DEGs. Intriguingly, Matr3-cKO hearts exhibit in total more DEGs than dKOs, which might be explained by higher genetic variability and therefore less significant DEGs. Since MATR3 and RBM20 are splice factors, phenotypes are only partially reflected by alterations in gene expression, but rather by alterations in splice isoforms.
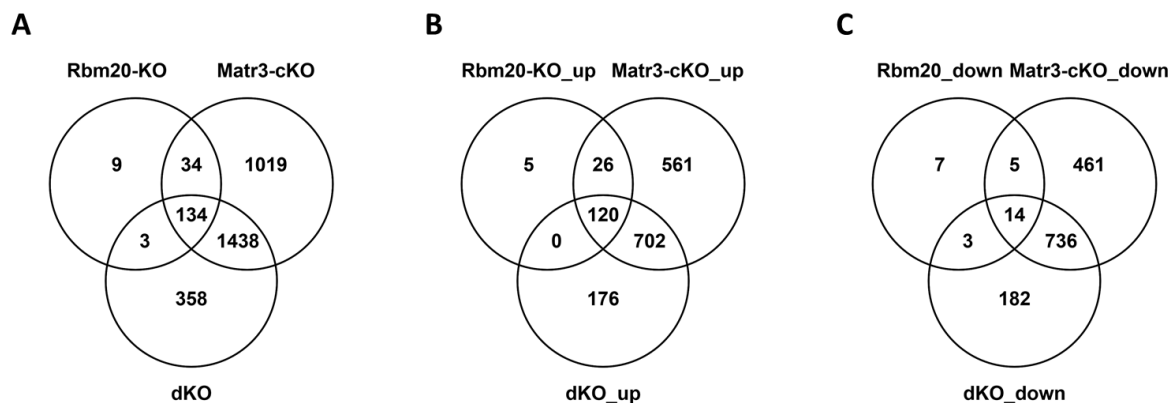
Figure 36 Differentially expressed genes in *Rbm20* and *Matr3* single as well as double knockout hearts

Venn diagram merging differential gene expression sets of the three conditions (Rbm20^{KO}, Matr3-cKO and dKO) for **A** all DEGs as well as **B** up-regulated and **C** down-regulated DEGs. The numbers of exclusively detected and shared differentially expressed genes (DEGs: basemean ≥ 5, log2fc ± 0,585, padj ≤ 0,05) are indicated.

Rbm20 inactivation results in subtle effects on the transcriptome, emphasizing the absence of DCM. In total, only 180 genes were differentially expressed (**Figure 37**A). Gene set enrichment analysis revealed deregulation of genes associated with *collagen fibril organization* (**Figure 37**B). In total, eight collagens are significantly upregulated in RBM20^{KO} hearts and four collagens fall into the category of Top50 DEGs (*Col1a2*, *Col6a3*, *Col6a6*, *Col9a1*; **Figure 37**C). Although increased collagen expression is detected during heart development, no obvious fibrosis is present in adult RBM20^{KO} hearts (see **Figure 9**, page 21).
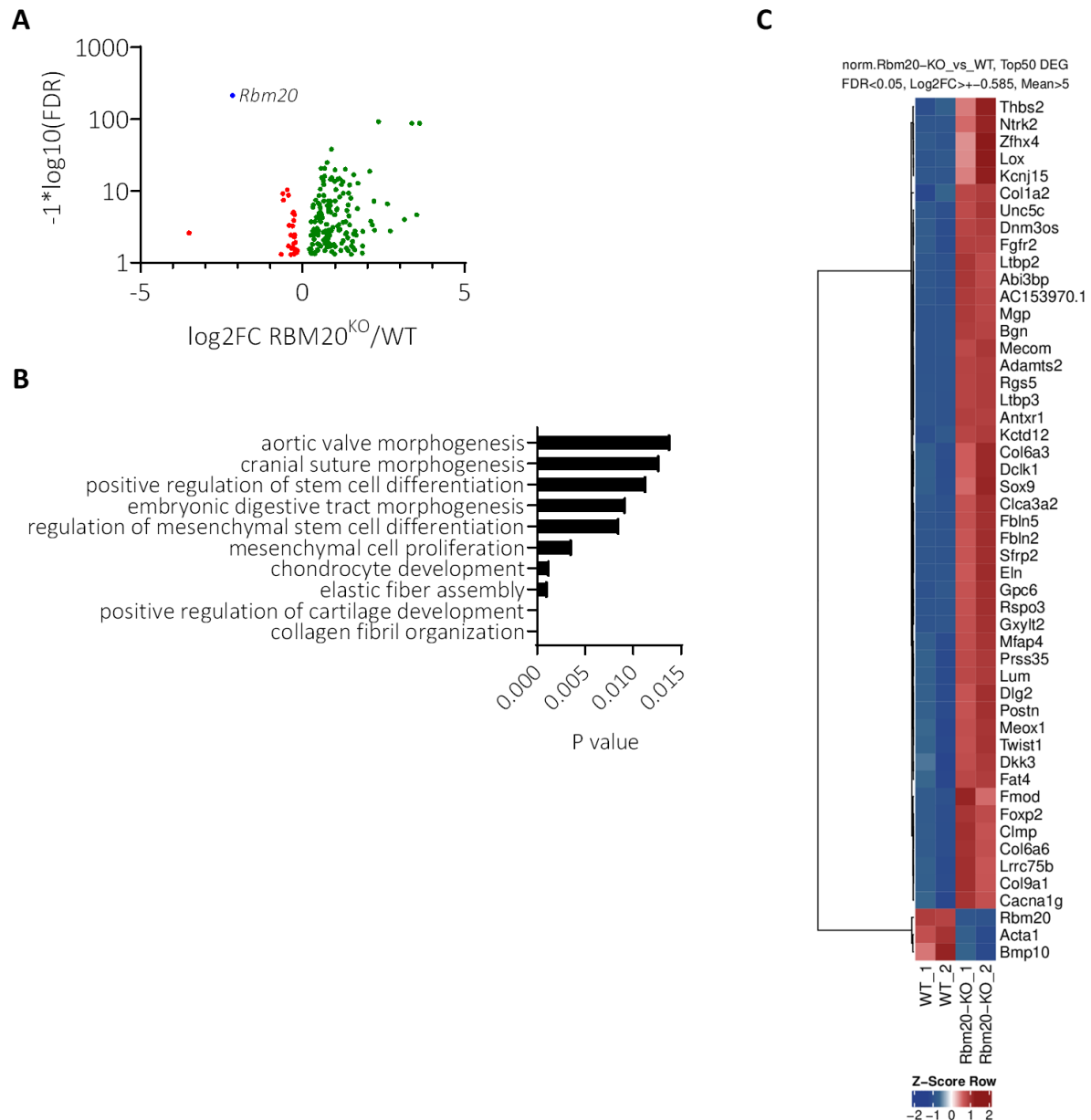
Figure 37 Minor transcriptomic changes in embryonic *Rbm20*-deficient hearts

Transcriptome analysis of RBM20[KO] hearts at E14.5 (n=2). **A** Volcano plot representation of differential expression analysis of genes in wild type versus RBM20[KO]. Values are blotted for statistical significance with FDR (padj) based definition (y-axis) versus magnitude of change (log2FC, x-axis). Regulation is considered when gene exhibit ≥ 5 counts, log2FC <> ± 0,585 and FDR ≤ 0,05. Red points mark genes that are significantly downregulated and green dots are upregulated in RBM20[KO]. *Rbm20* is labeled in blue. **B** Gene set enrichment analysis with Top 10 sets for GO *biological process complete* with Bonferroni-corrected for P < 0.05. **C** Top 50 most significantly differentially expressed DEGs in dKO hearts (sorted by smallest padj). The red blocks represent increased expression, and blue blocks represent genes with decreased expression levels.

A

-1*log10(FDR) vs log2FC Matr3-cKO/WT

Matr3

B

- endocardial cushion formation
- elastic fiber assembly
- aortic valve morphogenesis
- glomerulus vasculature development
- cell communication involved in cardiac conduction
- aorta morphogenesis
- sarcomere organization
- ventricular cardiac muscle tissue morphogenesis
- collagen fibril organization
- cardiac muscle cell development

P value

C

norm.WT_vs_Matr3–XML, Top50 DEG
FDR<0.05, Log2FC>+−0.585, Mean>5

Thbs1, Rpl3–ps1, Gria3, Ano3, Cdkn1a, Gm6166, Synpo, Mthfd2, Eda2r, Sox9, Pdgfra, Col6a6, Prss35, Kctd12, Unc5c, Dnm3os, Ddr2, Lum, Fbln2, Asns, Bgn, Tnc, Ccng1, Postn, Fgfr2, Meg3, Trp53inp1, Enc1, Dkk3, 9030617O03Rik, Ltbp4, Ltbp3, Adamts2, Lox, Mfap4, Antxr1, Col3a1, Col1a2, Itih5, Thbs2, Mrc2, Lrp1, Mmp2, Col1a1, Col5a1, Dcn, Cnn1, Rbm20, Acta2, Bves

WT_1, WT_2, WT_3, Matr3–XML_1, Matr3–XML_2, Matr3–XML_3

Z–Score Row
−2 −1 0 1 2

Figure 38 Early cardiomyocyte-specific deletion of *Matr3* induces major transcriptomic changes

Transcriptome analysis of Matr3-cKO hearts at E14.5 (n=3). **A** Volcano plot representation of differential gene expression analysis in wild type versus Matr3-cKO. Values are blotted for statistical significance with FDR (padj) based definition (y-axis) versus magnitude of change (log2FC, x-axis). Regulation is considered when gene exhibit ≥ 5 counts, log2FC <> ± 0,585 and FDR ≤ 0,05. Red points mark genes that are significantly downregulated and green dots are upregulated in the Matr3-cKO. *Matr3* is labeled in blue. **B** Gene set enrichment analysis with Top 10 sets for GO *biological process complete* with Bonferroni-corrected for P < 0.05. **C** Top 50 most significantly differentially expressed DEGs in dKO hearts (sorted by smallest padj). The red blocks represent increased expression, and blue blocks represent genes with decreased expression levels.
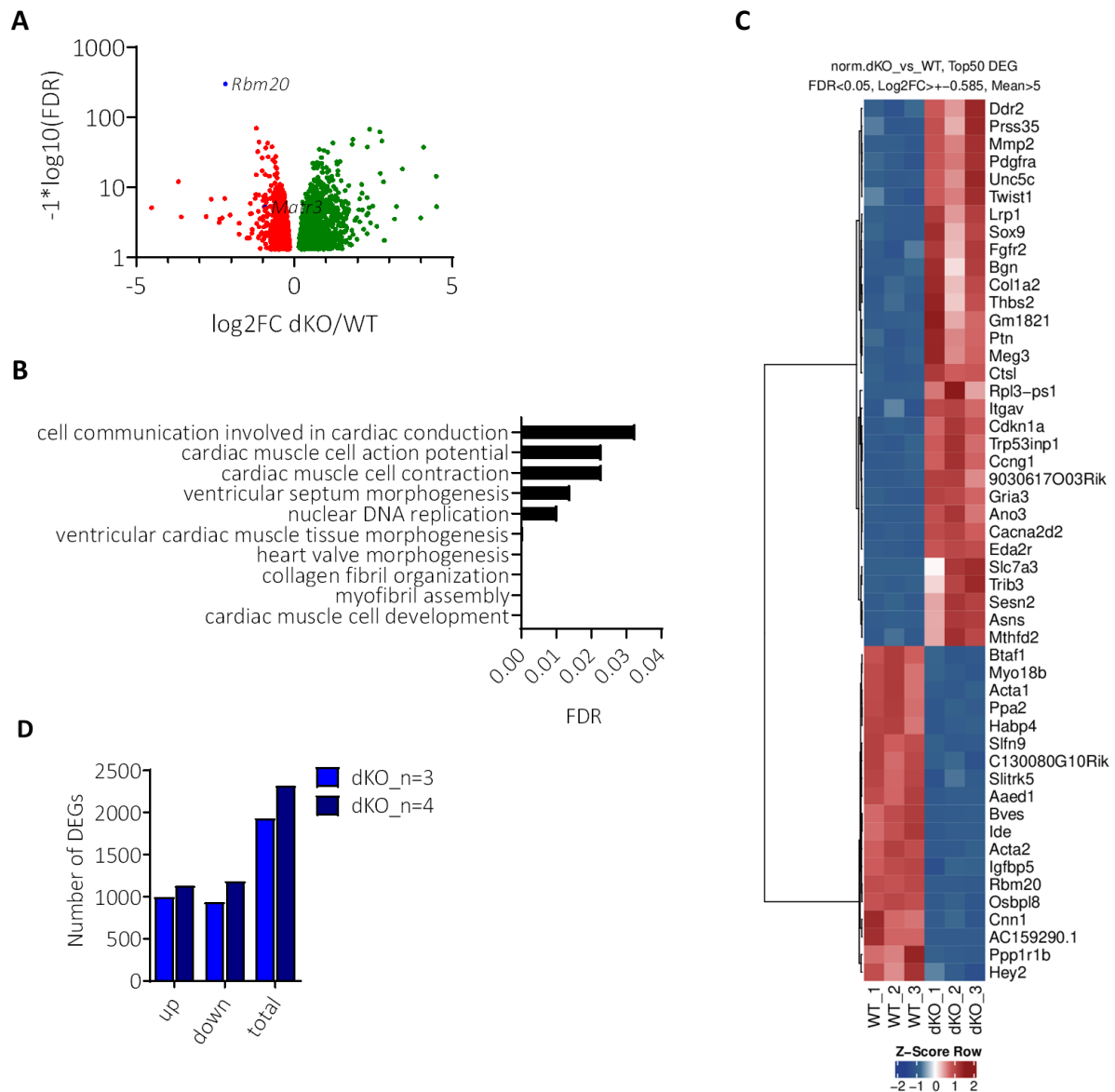
Figure 39 Transcriptomic changes of dKO hearts

Transcriptome analysis of dKO hearts at E14.5 (n=3). **A** Volcano plot representation of differential expression analysis of genes in wild type versus dKO. Values are blotted for statistical significance with FDR (padj) based definition (y-axis) versus magnitude of change (log2FC, x-axis). Regulation is considered when gene exhibit ≥ 5 counts, log2FC <> ± 0,585 and FDR ≤ 0,05. Red points mark genes that are significantly downregulated and green dots are upregulated in dKO hearts. *Rbm20* and *Matr3* are labeled in blue. **B** Gene set enrichment analysis with Top 10 sets for GO *biological process complete* with Bonferroni-corrected for P < 0.05. **C** Top 50 most significantly differentially expressed DEGs in dKO hearts (sorted by smallest padj). **D** Comparison of DEGs based on the number of sequenced replicates. The red blocks represent increased expression, and blue blocks represent genes with decreased expression levels.

In contrast to *Rbm20*-deficient hearts, transcriptome analysis of Matr3-cKO hearts at E14.5 revealed major transcriptome changes, reflected by 2.626 DEG that are divided into 1409 up-regulated and 1.217 down-regulated genes (**Figure 38**A). Again, genes associated with *collagen fibril organization* are upregulated in Matr3-cKO hearts, creating a transcriptome

signature of fibrosis (**Figure 38**B). Within the Top50 DEGs several collagens are listed, including *Col6a6*, *Col3a1, Col1a2*, Col1a1 *and* Col5a1. Contradictory, *Rbm20* is significantly decreased in Matr3-cKO hearts compared to non-littermate WT, again reinforcing the need for littermate controls (**Figure 35**D, page 45).

Intriguingly, dKO hearts exhibit less DEGs (1.934) than single knockout of *Matr3*, although there is a remarkable overlap of deregulated DEGs in Matr3-cKO and dKO (**Figure 36**, page 46). We attribute the higher number of DEGs in Matr3-cKO compared to Matr3-cKO/RBM2o dKO hearts to higher phenotype variability, resulting in less significant changes compared to WT. Accordingly, the number of DEGs in the dKO approaches the number of DEGs from the cKO as the sample size increases from triplicate to quadruplicate (**Figure 39**D). Towards better comparability, analysis is based on the triplicate for transcriptome and isoform changes. GO term for *collagen fibril organization* is the most deregulated term in dKO hearts, comparable to *Matr3* single knockout, (**Figure 39**B). Taken together, our gene expression analysis revealed distinct transcriptomic changes in E14.5 hearts lacking either *Rbm20*, *Matr3* or both.

RBM20- and MATR3-dependent mRNA splice isoform changes of cardiac transcripts
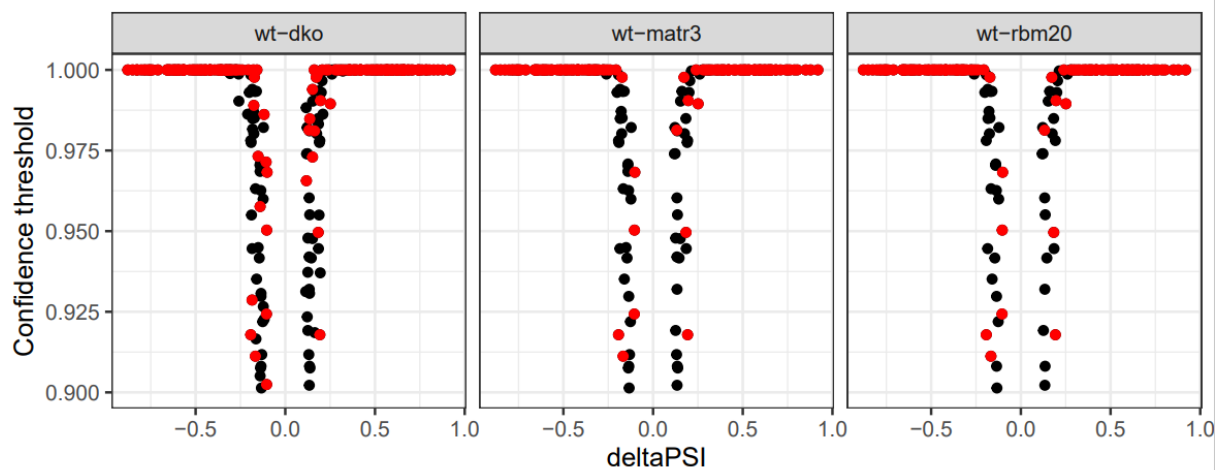
Figure 40 Identification of local splice variations (LSVs) in *Rbm20* and *Matr3* single as well as double knockout hearts

Volcano plots contrasting the ΔPSI (x-axis) against confidence threshold (y-axis) of each identified local splice variation (LSV) of the respective mouse line. Due to the bioinformatic analysis tool MAJIQ, both confidence and ΔPSI are strongly depending on each other. Significant LSVs (significance ≤1) are indicated by the black dots, whereat non-significant LSVs are labeled in red.

In addition to the gene expression analysis, the RNA-Seq data were analyzed for MATR3- or RBM20-specific mRNA splice variations using MAJIQ to identify local splice variations (LSV) in comparison to the wild type. Based on this assessment, RBM20[KO] exhibit 84, Matr3-cKO

92 and dKO 131 high-confidence LSV (**Figure 40**, **Figure 41**A). In total, 50 LSV were identified in all conditions, whereas RBP-specific LSV are less pronounced: 8 in RBM20^KO, 19 in Matr3-cKO and 31 in dKO. In addition, 26 LSV are common between RBM20^KO and dKO (resulting from the loss of RBM20) whereas 23 LSV are common between Matr3-cKO and dKO (caused by the loss MATR3). These LSVs were subsequently classified as alternative splicing events (classification of alternative splicing events see **Figure 2**, page 6). For all knockout strains the majority of LSVs represent binary events with intron retention (IR) or exon skipping (ES, **Figure 41**C), indicating that both RBM20 and MATR3 act as splicing repressors as previous described previously.
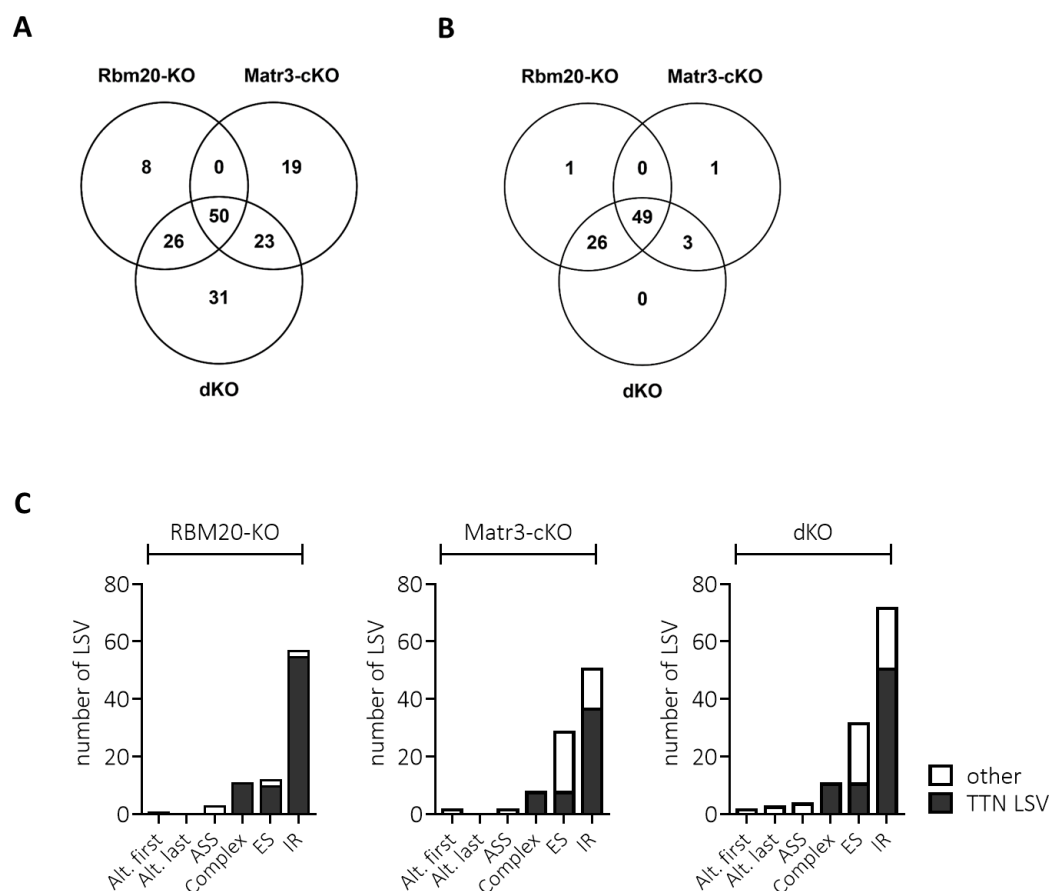
Figure 41 Number of local splice variants in *Rbm20* and *Matr3* single as well as double knockout hearts

Venn diagrams of all local splice variants (LSV; **A**) and Titin-related LSVs (**B**), showing the overlap between the three knockout strains RBM20^KO, Matr3-cKO and dKO. **C** Bar diagram displaying the number of LSVs after classification as alternative first exon, alternative last exon, ASS, complex, ES or IR (from left to right). Classification of Titin-related LSVs are highlighted in dark grey, and LSVs of other transcripts are white. Alternative first exon: alt. first, alternative last exon: alt. last, alternative splice site (ASS), complex (involvement of three or more splice graph edges), exon skipping (ES) or intron retention (IR). Local splice variations = LSV: ≥2 splice graph edges, Percentage Spliced In (PSI)>0.9 and ΔPSI>0.05)

Remarkably, most LSV accumulate in the TTN transcript and a considerable overlap between merging LSVs was observed for the three knockouts models (**Figure 41**B). Within the TTN transcript, the majority of LSVs occur within the PEVK region (**Figure 42**A-C). Notably, RBM20-mediated LSVs are detected in both RBM20-single as well as dKO mice, generating the RBM20 mutant-specific- N2BA-G TTN isoform (**Figure 46**, page 56).
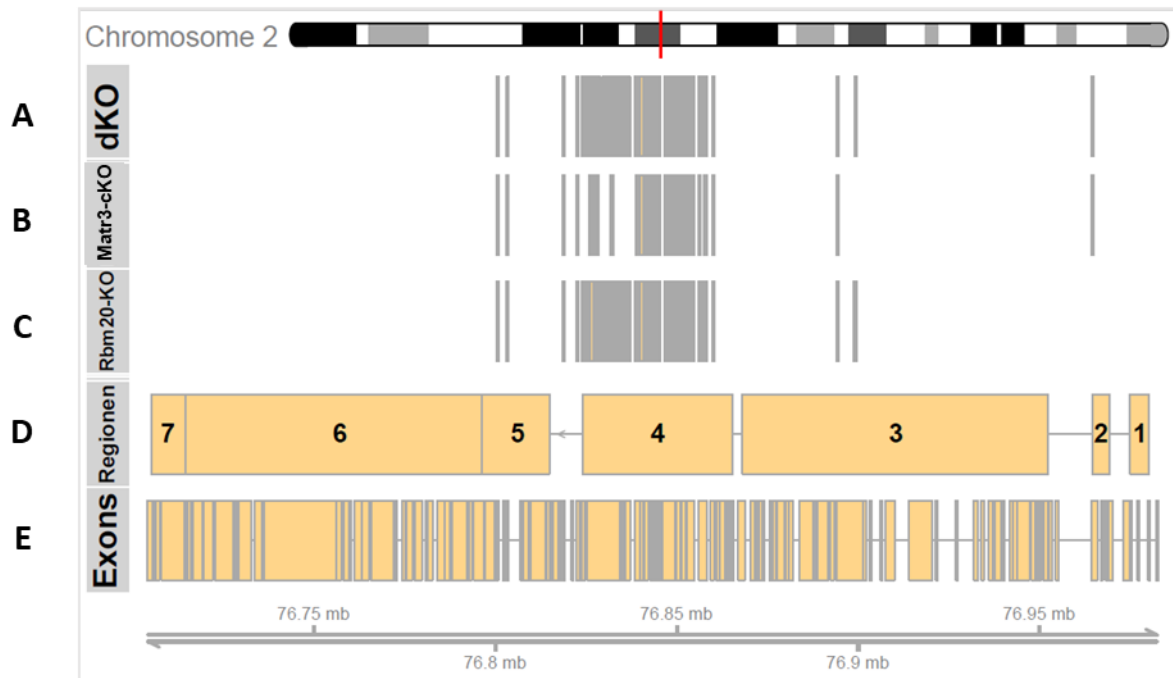
Figure 42 Differential splicing of Titin in RBM20 and MATR3 single and double knockout cardiomyocytes

A-C LSV significantly changed in dKO (A), Matr3-cKO (B) and RBM20-KO (C) hearts. **D** TTN domains are indicated by the following domains: 1, 3, 5, 7 immunoglobulin-like, 2 Z-repeat, 4 PEVK, 6 Fibronectin Type III. **E** Exons are indicated at the bottom.

Although there are minor changes in gene expression and no DCM-like phenotype in the RBM20^{KO} mutants, a comparable number of total LSVs was identified compared to the Matr3-cKO. Interestingly, there is no correlation between the murine alternatively spliced transcripts and the previously described 31 conserved genes with RBM20-dependent alternative splicing in humans and rats - except for titin (**Figure 43**A). Furthermore, no overlap with published MATR3-dependent AS events was observed, which might result from the use of different cell types, indicating that MATR3 indeed promotes alternative splicing of cardiac-specific transcripts (**Figure 43**B). Nevertheless, we identified an overlap with some RBM20-regulated transcripts, namely *Camk2d*, *Ldb3*, *Sorbs1*, and *Ttn* (**Figure 43**C).
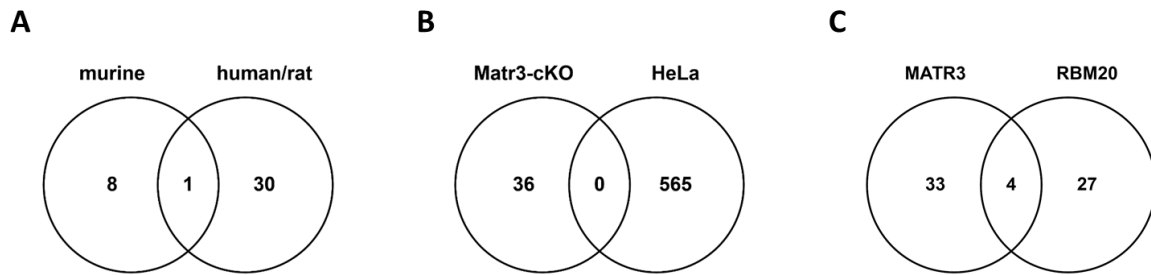
Figure 43 Comparison of identified, alternatively spliced transcripts with published data

A Comparison of our data with 31 RBM20-dependent alternative splicing events common in human and rat hearts [32]. **B** Comparison of our data with 565 MATR3-depentend alternatively spliced transcripts in human HeLa cells [89]. **C** Comparison of murine MATR3 and human/rat RBM20 mis-spliced targets [32].

For a more detailed analysis of the LSVs, we selected two targets of interest, *Ldb3* and *Camk2d*. In general, cardiac *Ldb3* isoforms include cardiac-specific exon 4, whereas skeletal-muscle isoforms express exons 5 and 6 instead of exon 4 [143]. Recent studies have demonstrated that hRBM20 regulates mutually exclusive inclusion of exon 4 in human and rat *Ldb3*. As a result, loss of functional RBM20 leads to skipping of exon 4 and the subsequent alteration in *Ldb3* isoform expression are related to DCM [143, p. 3], [144, p. 3], [145]. In our data set, only MATR3-cKO and dKO (but not RBM20-KO) hearts demonstrate defective splicing in *Ldb3*. Usage of an alternative splice site (ASS) was significant for boundary 8-9 (**Figure 44**A-G, in purple), accompanied by decrease of exon boundary 5-9 usage, although the latter change was not significant (**Figure 44**A-G, in red). Remarkably, the abundance of exon 4, which is regulated by RBM20, is not altered in *Matr3*-deficient cardiomyocytes. Notably, gene expression of *Ldb3* is significantly reduced in both, Matr3-cKO and dKO, respectively (**Figure 44**H). Taken together, the loss of *Matr3* in cardiomyocytes induces a *Ldb3* isoform, which presumably interferes with formation of the z-disk.

In addition to *Ttn* and *Ldb3*, calcium/calmodulin-dependent protein kinase II d (*Camk2d*) has previously been reported as a RBM2-regulated AS splicing target, where exons 14–16 are mutually exclusive [32], [92]. Our findings revealed that loss of *Matr3* results in two LSVs (referring to exon 20 and 21; **Figure 45**A). dKO hearts show a rather complex splicing event at exons 18-21 (**Figure 45**B). Notably, gene expression of *Camk2d* is significantly decreased in both conditions (**Figure 45**C). Based on literature and our results, we conclude that MATR3 and RBM20 indeed share a common set of alternatively spliced transcripts such as *Camk2d*, *Ldb3*, and *Ttn*. However, MATR3 and RBM20 play distinct roles in cardiac splicing, since transcripts respond differently to the loss of the RBPs – at least during cardiogenesis.
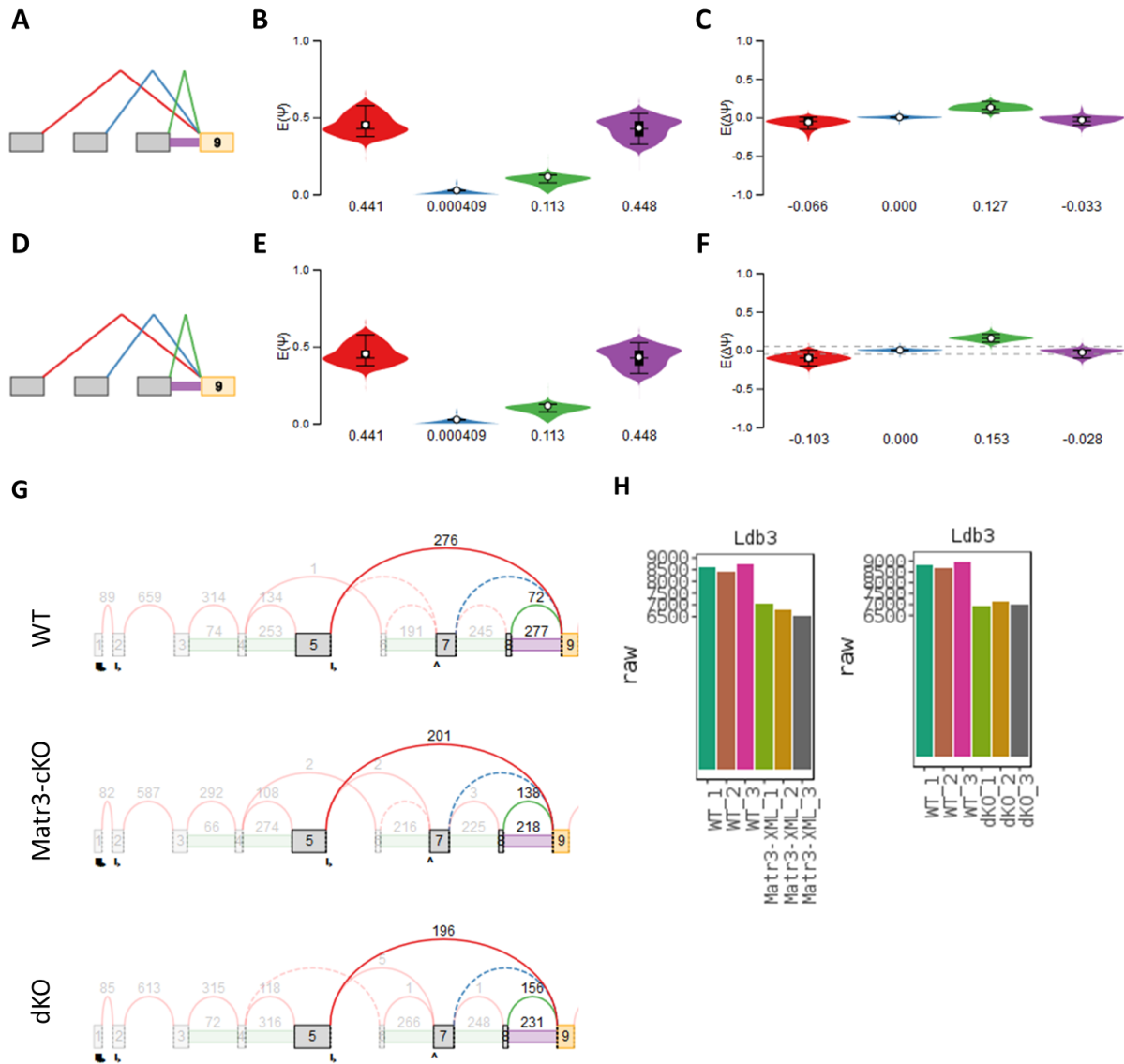
Figure 44 MATR3 regulates alternative splicing of *Ldb3*

Alternative splicing of *Ldb3* in Matr3-cKO (**A-C**) and dKO (**D-F**) at LSV ID: ENSMUSG00000021798.14:t:34567398-34567567. Matr3-cKO (**A**) and dKO (**D**) exhibit similar LSV type. PSI per junction and ΔPSI per junction for Matr3-cKO (B+C) and dKO (E+F). **G** Voila visualization of significant LDB3 LSV for MATR3-cKO and dKO in comparison to WT. **H** Gene expression of Ldb3 in Matr3-cKO and dKO hearts compared to WT. RNA-Seq based expression of *Ldb3* in Matr3-cKO: log2FoldChange Matr3-XML/norm.WT -0,34, padj 0,00 and in dKO: log2FoldChange dKO/norm.WT -0,33, padj 0,00.
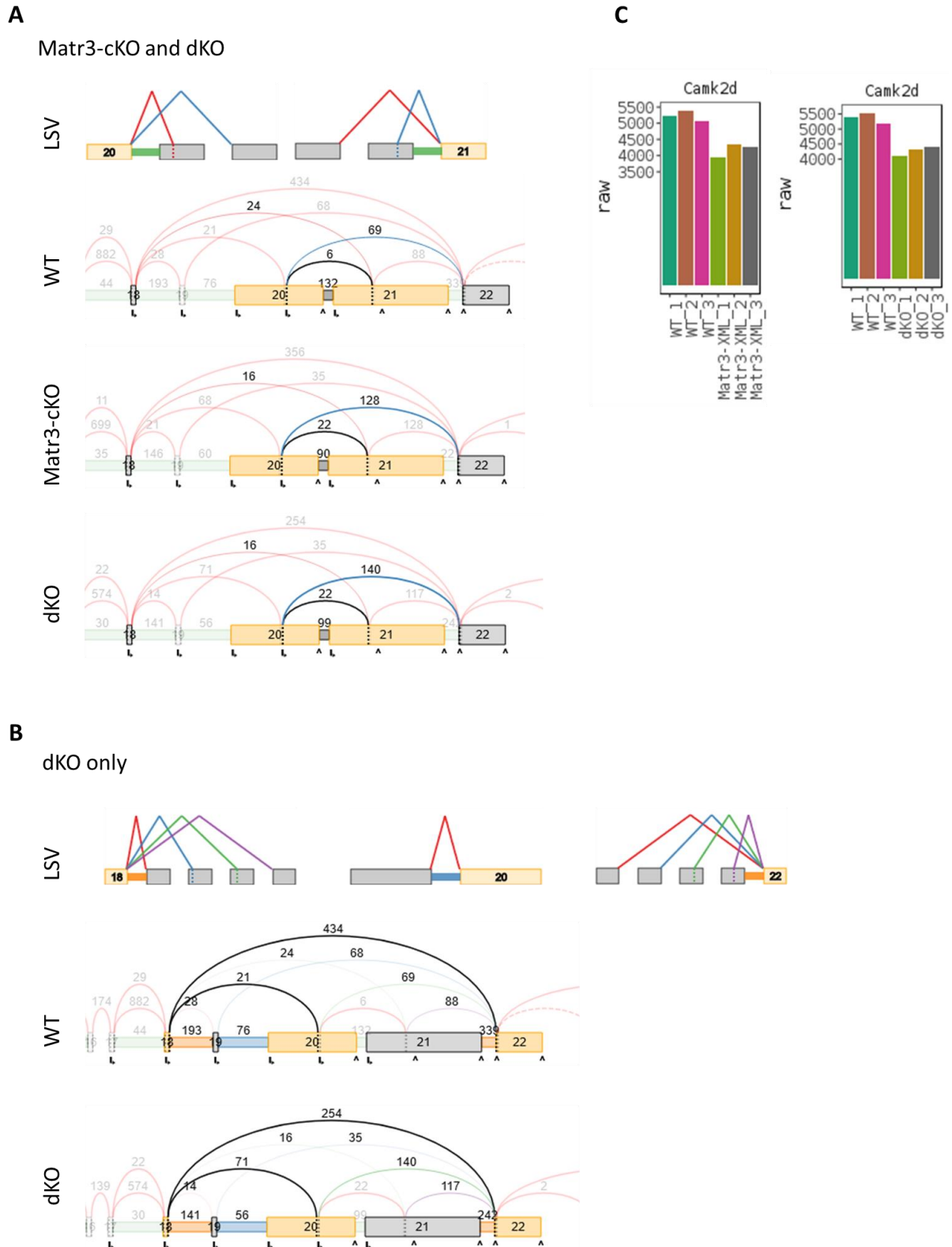
Figure 45 MATR3 regulates alternative splicing of *Camk2d*

Commonly altered LSVs in Matr3-cKO and dKO (**A**) and dKO-exclusive LSVs (**B**) for *Camk2d*. Voila visualization of significant LSV for MATR3-cKO and dKO in comparison to WT. **C** Gene expression of *Camk2d* in Matr3-cKO and dKO hearts compared to WT. RNA-Seq based expression of *Camk2d* in Matr3-cKO: log2FoldChange Matr3-XML/norm.WT - -0,32, padj 0,00 and in dKO: log2FoldChange dKO/norm.WT -0,33, padj 0,00.

Loss of *Matr3* in cardiomyocytes results in a switch of titin isoforms

The alternative splicing analysis demonstrated that Titin is a main target of MATR3 in murine cardiomyocytes. To further validate this finding, Titin isoforms were determined by titin gels. Since titin gels require a large amount of input material, late-embryonic E18.5 hearts of single and double knockouts were examined. At this developmental stage, titin undergoes an isoform switch, although the fetal N2BA isoform is still predominantly expressed [74], [95]. Only in adult hearts the N2B isoform prevails (**Figure 46**A+B). The N2BA/N2B ratio in embryonic E18.5 hearts is significantly increased in the Matr3-cKO in comparison to controls, suggesting that MATR3 plays an important role for isotype switching (**Figure 46**C). In contrast the giant N2BA-G titin isoform occurs exclusively in RBM20[KO] and dKO, but not in Matr3-cKO hearts, indicating that MATR3 is dispensable for this process (**Figure 46**D). Furthermore, no additional effects of MATR3 for titin isoform expression was observed in dKO compared to the RBM20[KO] hearts. Mis-splicing and defects in titin isoform switching will have major effects on passive stiffness and will impair cardiac contractility, which reflects the physiological measurements in the knockout models.
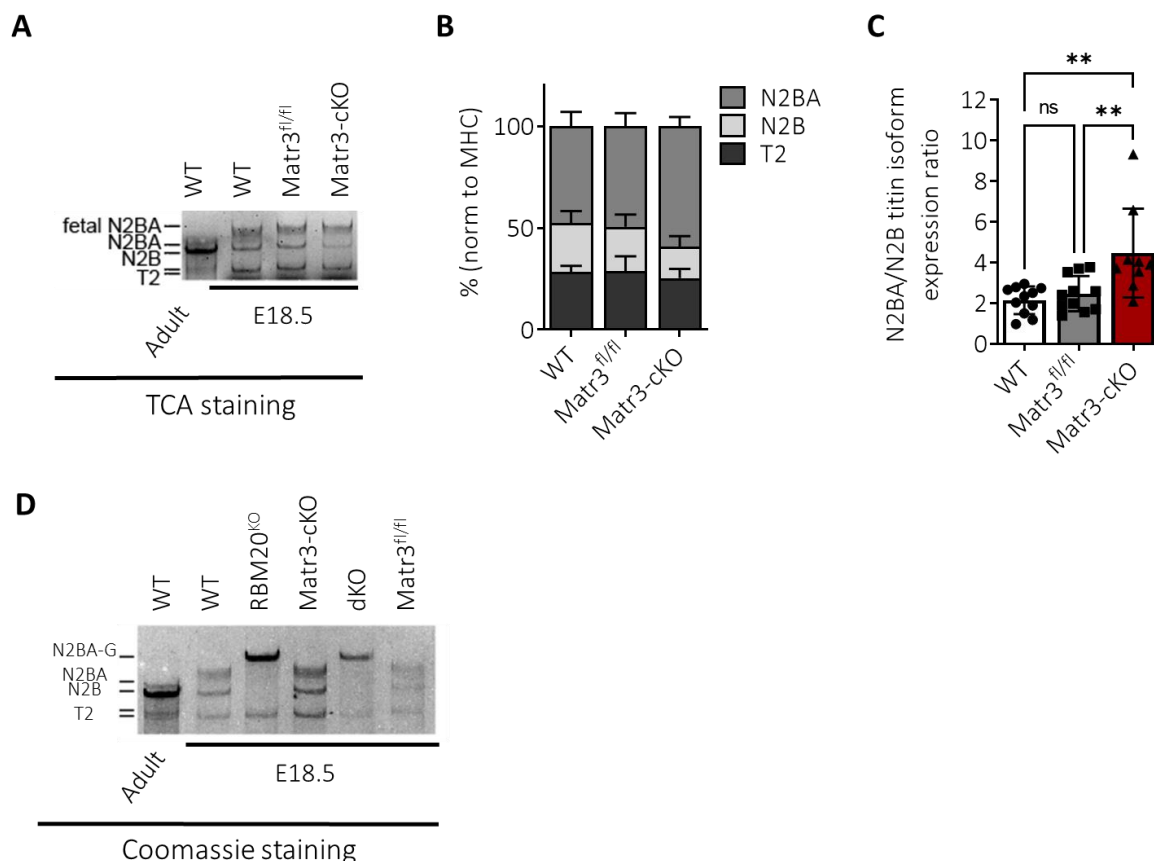
Figure 46 Changes of Titin isoform composition in *Rbm20* and *Matr3* single and double knockout hearts at E18.5

A TCA-stained titin gel visualizing titin isoform in E18.5 hearts of WT, MATR3-floxed and MATR3-cKO. **B** Quantification of titin isoforms, normalized to myosin heavy chain (MHC) bands. N2BA and N2B indicate full-length titin isoforms; T2 is the proteolytic fragment of titin (n≥9). **C** Quantification of N2BA/N2B titin isoform

expression ratio (n≥9) reveals an elevated N2BA/N2B ratio in Matr3-cKO. Data represent the mean ± SD. One-way ANOVA with post-hoc Tukey HSD (Honestly Significant Difference). ns = not significant, **P < 0.01. **D** TCA-stained titin gel from E18.5 embryonic hearts from WT, RBM20[KO], Matr3-cKO and corresponding Matr3^{fl/fl} control and the dKO.

Cardiomyocyte-specific mRNA targets of MATR3

To determine the ratio of alternative splicing events regulated by direct protein-RNA binding that are not caused by secondary effects, we searched for bona fide mRNA targets of MATR3. Since the number of primary cardiomyocytes is limited and not sufficient for CLIP experiments, we applied HyperTRIBE to determine cardiomyocyte-specific mRNA targets of MATR3. This approach was first tested in a suitable cell culture model, before applying it to the mouse.

Evaluation of cardiomyocyte cell culture models reveals density-dependent transcriptional regulation of *Matr3*

Cell culture models of murine cardiomyocytes are limited, mainly based on either embryonic stem cell (ESC)-derived cardiac bodies [146], [147] or the cardiac muscle cell line HL-1 [148]. HL-1 cells present cardiac features including e.g. contractility [148], hypoxia-induced stress response [149], and the expression of calcium and potassium channels [150]. In our culture conditions, cardiac bodies showed robust expression of cardiomyocyte markers such as MYH6 and MYH7 but still expressed low levels of ESC markers such as *Sox2* (**Figure 47**). *Matr3* and *Rbm20* expression are highest in HL-1 cells compared to cardiac bodies or isolated adult cardiomyocytes. In addition, HL-1 cells offer the opportunity of transient transfections, thereby enabling HyperTRIBE studies.
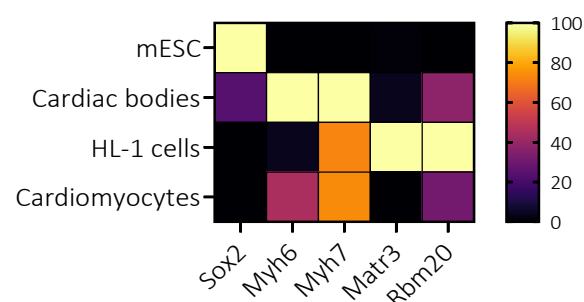
Figure 47 Expression of target genes in cardiac cells compared to embryonic stem cells

Heatmap of marker genes and target gene expression (determined by qRT-PCR, n≥3) in four different cell types: 1. mESC= murine embryonic stem cells, 2. CM7/J1-ESC-derived cardiac bodies, 3. HL-1 cells and 4. Isolated adult cardiomyocytes. Marker genes: stem cell marker *Sox2*, cardiac striated muscle genes *Myh6* and *Myh7*. Target genes: *Matr3* and *Rbm20*. Color scheme: Yellow indicates a normalized gene expression value of 100% and black indicates a value of 0%.

Immunofluorescence antibody staining reveled a presence of MATR3 in the nucleus in low- and medium-dense HL-1 cultures. Surprisingly, the MATR3 protein was completely absent when HL-1 cells were kept at high density (**Figure 48**A). This observation was further confirmed at the mRNA expression level (**Figure 48**E), indicating that *Matr3* expression is predominantly regulated at the transcriptional level. Density-dependent downregulation of MATR3 was not only observed in murine HL-1 cells, but also in human primary endothelial cell lines (HUVEC and HDLEC; **Figure 48**B+C), indicating a conserved regulatory mechanism mediated by cellular density. Notably, HEK293T are heterogenous in respect to the downregulation of MATR3 protein shown by IF (**Figure 48**D), since some cells still exhibit a clear nuclear MATR3 staining under confluency. Here, remaining MATR3-expressing HEK293T cells also appear to masked the lack density-dependent transcriptional regulation of Matrin3 mRNA transcripts (**Figure 48**F). To avoid density-dependent downregulation of *Matr3*, HL-1 cells of medium density were used for the HyperTRIBE method. The density-dependent regulation of MATR3 also motivated us to analyze potential upstream regulatory mechanism (see page 65).
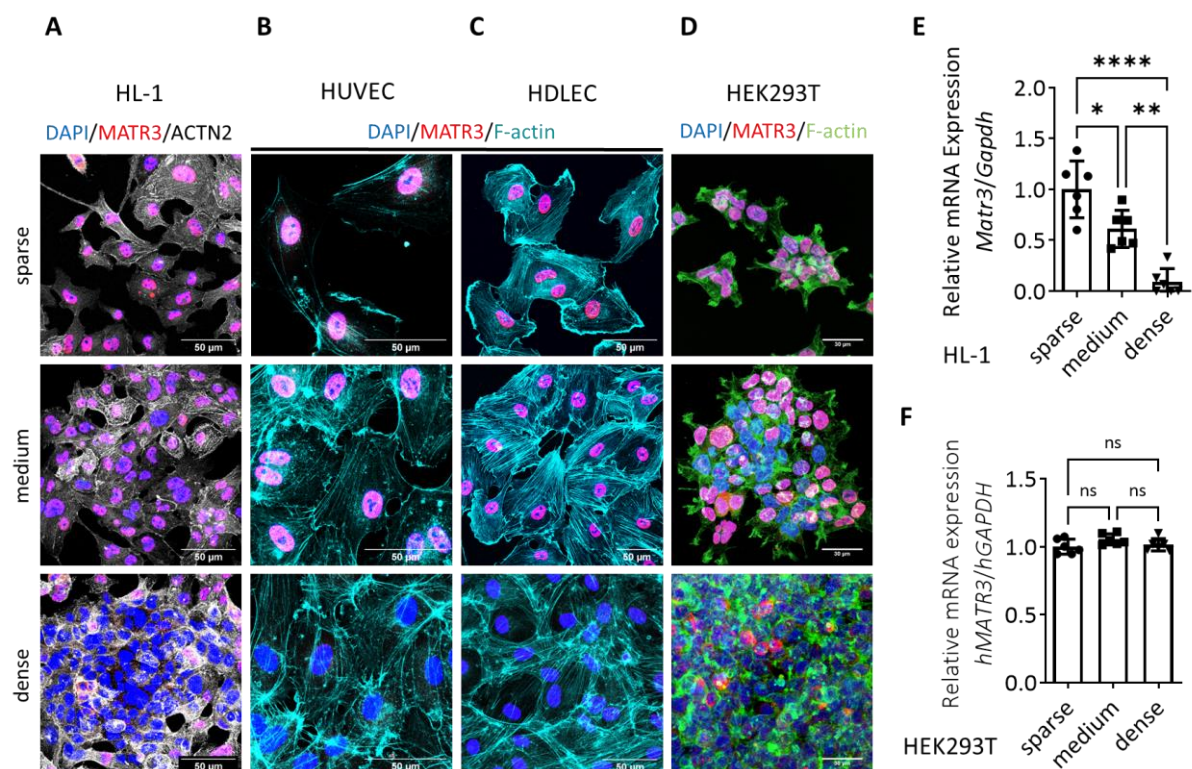
Figure 48 Density-dependent heterogeneity of MATR3

A-D Immunofluorescent staining of MATR3 in indicated cell lines: **A** Murine, cardiac HL-1 cells; **B** human, primary endothelial HUVECs or **C** lymph endothelial HDLECs and **D** human, embryonic HEK293T cells. Note the loss of MATR3 in A-C (but not in D) under confluency. **E+F** qRT-PCR using HL-1 cells (E, n=6) and HEK293T cells (F, n=6) with indicated densities reveals transcriptional regulation of density-dependent *Matr3* heterogeneity in HL-1

cells. Data represent the mean ± SD. Two-way ANOVA with Bonferroni's multiple comparisons test. ns = not significant, *P < 0.05; **P < 0.01; ****P < 0.0001.

Experimental design of HyperTRIBE for MATR3

Since the iCLIP method requires large amounts of material as input whereas the number of embryonic cardiomyocytes is limited, we adapted the recently developed HyperTRIBE (HT) method to identify direct RNA targets of the RBP Matrin3 in embryonic cardiomyocytes. Three different fusion proteins were generated, all harboring a V5 epitope tag (**Figure 49**). First, murine *Matr3* was fused to the catalytic domain of Drosophila ADAR (dmADAR*), carrying the hyperactive mutant E488Q [25]. This M3-HT fusion protein (143 kDA) is able to bind target mRNAs, thereby providing editing A-to-I near the binding site. Second, a *Matr3* variant without RNA recognition motifs was fused to dmADAR* (M3Δ-HT, 125 kDA). This fusion protein served as negative control, since it has lost its ability for RNA-binding. Third, we fused the dmADAR* domain to the V5 epitope (HT, 50 kDA) to identify background editing. Background editing was defined as sequence-independent editing events induced by the catalytic domain of ADAR itself, which might occur simply due to proximity to RNA. Both controls (HT and M3Δ-HT) were used for normalization to eliminate background edits and endogenous editing events mediated by ADAR 1 and 2 [151]. Since the JACUSA bioinformatic pipeline compares two conditions, bioinformatic analysis of "M3-HT normalized to M3Δ-HT" and "M3-HT normalized to HT" was applied to identify transcripts that were specifically edited by the M3-HT fusion, normalized to the corresponding background control. In order to obtain an unbiased analysis, both data sets were analyzed in parallel.
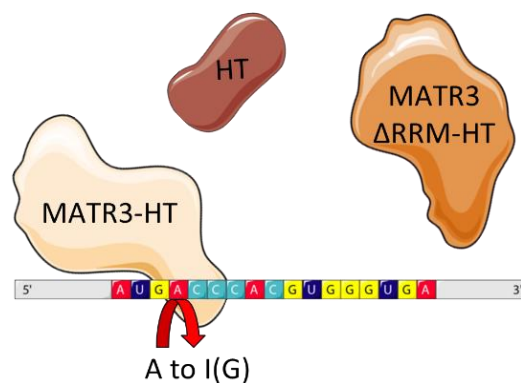
Figure 49 Overview of HyperTRIBE fusion proteins for MATR3 and their RNA-binding affinities

Schematic illustration indicating the MATR3 protein fusion with the catalytic domain of hyperactive ADAR (M3-HT fusion protein in beige), which can bind to RNA and performs A-to-I editing nearby the binding site. In addition, control fusion of MATR3 without both RNA recognition motifs (M3Δ-HT, in orange) and dmADAR* fusion protein (HT, in brown) are illustrated. Both control fusions are not able to bind to RNA targets of MATR3 and are used to identify background editing events.

Pilot experiment of MATR3-HyperTRIBE in murine HL-1 cell line

As a proof of principle, HyperTRIBE was tested in murine HL-1 cardiomyocyte cell line by transient transfection with the HyperTRIBE plasmids. HL-1 cells endogenously express *Matr3* (**Figure 47**, page 57), thereby representing a suitable cell culture model to validate HyperTRIBE fusion proteins and investigate RNA targets of MATR3. The nuclear localization of the three fusion proteins in transiently transfected HL-1 cells was confirmed by immunofluorescence staining with an antibody against V5 epitope tag (**Figure 50**A). Both, endogenous MATR3 and HT fusion proteins localize to the nucleus, indicating that fusion of the catalytic domain of dmADAR to MATR3 does not alter the subcellular localization. In addition, Western blot by V5 antibody detected fusion proteins with the calculated sizes (**Figure 50**B). A pilot RNA-seq experiment of transiently transfected HL-1 cells identified MATR3-HT editing events (data not shown).
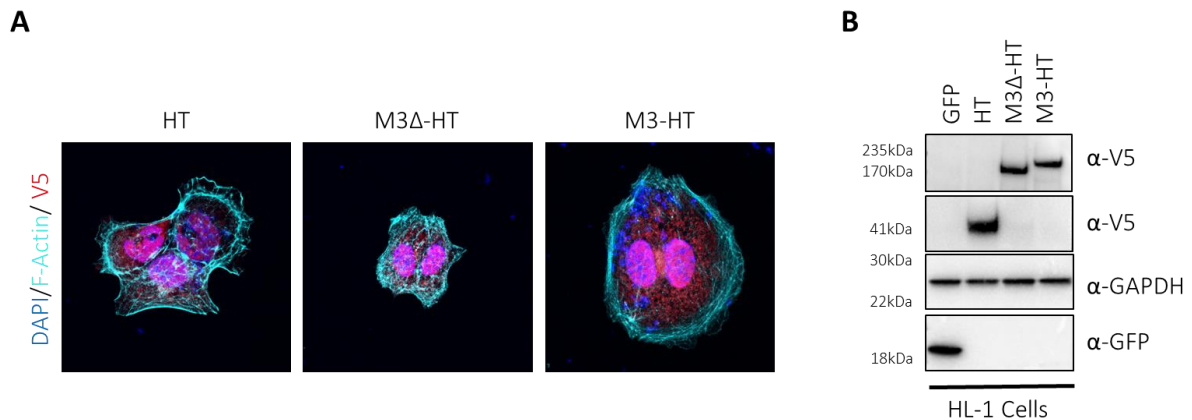
Figure 50 Transient overexpression of HT fusion proteins in cardiac HL-1 cells

A IF staining of V5-tag (red) staining in HL-1 cells transiently overexpressing HT fusion proteins. Cells were counter stained with F-Actin (cyan) and nuclear stain DAPI (blue). **B** Western blot validation of HT fusion proteins at calculated molecular weights in transiently transfected HL-1 cells. GFP overexpressing vector was used as transfection control.

Establishing HyperTRIBE mouse models for MATR3

In a next step, transgenic HyperTRIBE mice were generated by expressing the HT fusions in the ROSA26 locus after Cre-mediated recombination with the cardiomyocyte-specific XMLC2-Cre line. All three HT mouse strain were viable and fertile, indicating that overexpression of HT fusion proteins does not induce side effects (data not shown).

To identify the RNA-targets of MATR3 in embryonic cardiomyocytes, E14.5 hearts from the three individual transgenic mouse lines were collected and processed for RNA-Seq, which is then used for both gene expression and JACUSA-based editing analysis. When compared to C57BL/6J wild type (**Figure 51**A) or HT mice (**Figure 51**A, B), *Matr3* expression is 2-fold higher in M3-HT and M3Δ-HT hearts at this developmental stage. Gene expression analysis

revealed that concomitant with the overexpression of *Matr3*, cardiac stress response markers, as well as both endogenous adenosine deaminase ADAR enzymes were slightly upregulated in the RNA-Seq data (**Figure 51**B). However, the qRT-PCR-based verification of a larger sample set did not confirm cardiac stress response or upregulation of ADARs in E14.5 hearts overexpressing MATR3-HT fusion proteins (**Figure 51**C).

To elucidate whether *Matr3* overexpression per se leads to cardiac stress responses *in vivo*, a Matrin3 overexpressing mouse line was generated. For this approach, murine V5-HA double-tagged *Matr3* was overexpressed from the ROSA26 locus combined with the XMLC2-Cre. The cardiomyocyte-specific, 1.5-fold overexpression of *Matr3* did not result in a significant upregulation of the indicated cardiac stress markers in E14.5 hearts (**Figure 51**D). Since overexpression of HT fusion proteins is not resulting in a pathophysiological response, we applied this model to identify cardiac MATR3 mRNA targets *in vivo*.
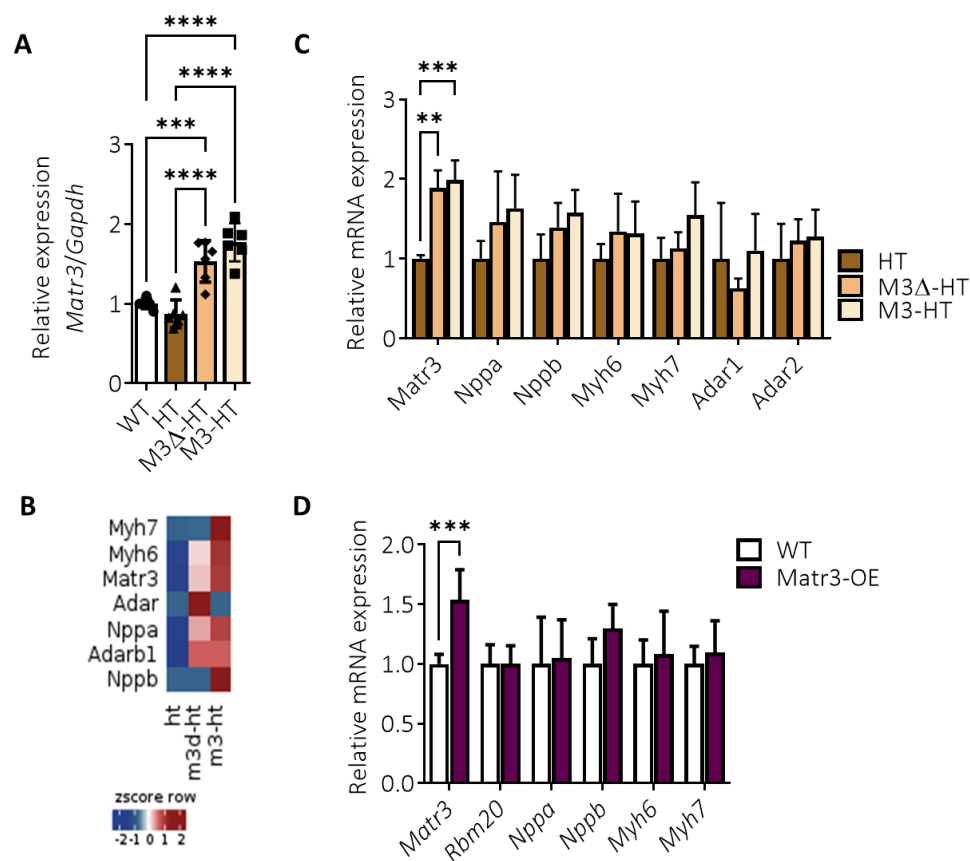
Figure 51 Cardiomyocyte-specific expression of MATR3-HT fusion proteins

A qRT-PCR validation of E14.5 hearts overexpressing MATR3-HT fusions proteins (n=6). **B** Expression of selected genes in the RNA-seq data set (n=3) and **C** corresponding validation by qRT-PCR (n=6). **D** qRT-PCR of E14.5 hearts overexpressing (OE) V5-HA double-tagged *Matr3* in cardiomyocytes (n=8) compared to littermate WT (n=6). **A+C+D** Data represent the mean ± SD. Two-way ANOVA with Bonferroni's multiple comparisons test. P values less than or equal to 0.05 are depicted: **P < 0.01; ***P < 0.001; ****P < 0.0001.

HyperTRIBE identifies hundreds of direct RNA targets for MATR3 in cardiomyocytes

The RNA-Seq data was subsequently analyzed by JACUSA pipeline to determine the MATR3-HT-induced differential A-to-I editing sites events (hereinafter called edits). Single-nucleotide polymorphisms (SNPs) were filtered out. Transcripts with a single editing site were considered to be more likely non-specific, whereas transcripts with two or more edits were defined as high-confidence HyperTRIBE targets of MATR3 and were analyzed further.
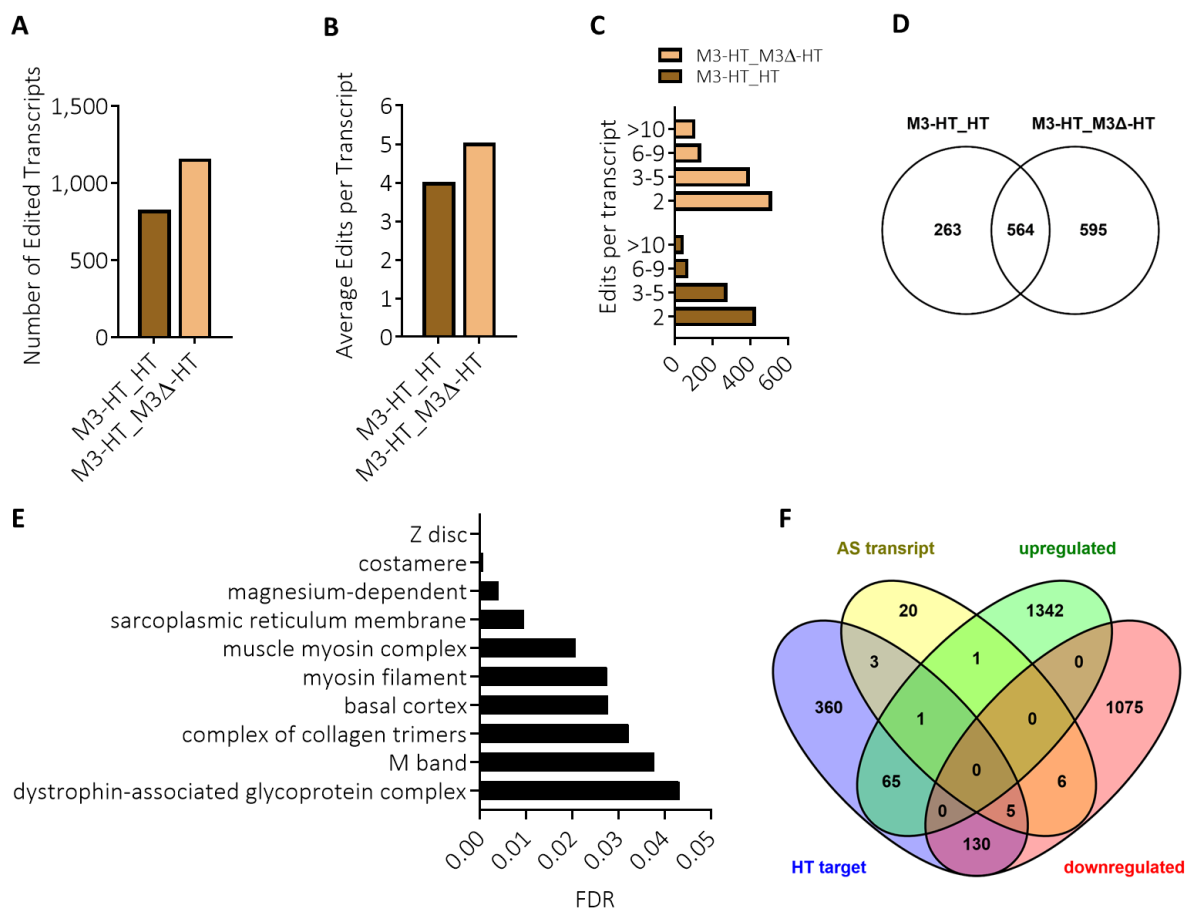
Figure 52 HyperTRIBE for MATR3 identifies hundreds of direct cardiac pre-mRNA targets

A Number of transcripts with at least two edits depending on the control condition (HT or M3Δ-HT). **B** Average number of edits per transcripts. **C** Frequency histogram clustering the number of edits per transcripts. **D** Venn diagram merging the overlap of high confidence targets. **E** GO analysis for the cellular component of high-confidence targets mRNAs of Matrin3 with FDR P < 0.05. Only the Top 10 Go Terms are shown. **F** Overlap of high confident targets (in blue) with effects upon *Matr3* gene knockout, classified by alternatively spliced transcript (AS transcript, in yellow) as well as up- (in green) or downregulated (in red) DEGs.

Depending on the control, several hundred edited transcripts were identified (**Figure 52**A), indicating that MATR3 HyperTRIBE fusion proteins catalyzed appropriate deamination of A-to-I editing reaction. In average, each target transcript harbors 4-5 edits (**Figure 52**B). However, frequency histograms of the number of edits per target transcript unravel that most genes have two edits, but some transcripts exhibit even more than 10 edits (**Figure 52**C). By

merging the two comparisons, we define an overlap of 564 edited transcripts as cardiomyocyte-specific HT targets for MATR3 (**Figure 52**D), including *Camk2d*, *Ldb3* and *Ttn*. These 564 high-confidence targets are enriched for cardiac GO terms such as Z-disc and A-band, supporting the idea that MATR3 targets cardiac-specific transcripts (**Figure 52**E). Surprisingly, only 9 out of 564 HT targets are alternative spliced in embryonic hearts upon the loss of *Matr3* (**Figure 52**F, overlap yellow and blue)*. In addition, 201 HT targets are significantly deregulated, including 66 upregulated (overlap green and blue) and 141 downregulated genes (overlap red and blue). Representative mapping of the three targets of interest *Camk2d*, *Ldb3* and *Ttn* are shown in **Figure 53**A-C, where edits are distributed across the target transcripts.

In total, we found HyperTRIBE targets that are not alternatively spliced by MATR3, but might be induced by the overexpression of Matr3 HT fusion proteins or regulated by another MATR3-dependent RNA process, which was not part of this work. On the other hand, HyperTRIBE did not mark all MATR3-spliced target transcripts identified by MAJIQ. This could be explained by RNA editing levels below the threshold of detection combined with an insufficient sequencing coverage. In addition, since TRIBE does not provide the nucleotide resolution binding profile of techniques such as in CLIP, TRIBE is dependent on Adenosines in the proximity of the binding site itself, which is probably not always the case. Furthermore, the identification of HyperTRIBE targets is depending on the length and turnover rate of certain transcripts, which was not taken into account here.

Although HyperTRIBE does not identifies the exact binding site of an RBP at single-nucleotide resolution, a metagene analysis of the location of HT editing sites was performed (**Figure 53**D+E). For that, the pre-mRNA sections were subdivided in start and stop codon, 5'UTR, 3'UTR, coding region (CDS) and intronic region. In general, editing events are predominantly located in the intronic regions of pre-mRNA, followed by CDS, confirming that MATR3 binds to pre-mRNAs. This is consistent with previous reports, demonstrating that MATR3 binds predominantly to intronic regions of pre-mRNA, where it acts as an intronic splicing repressor [89], [90], [116]. Taken together, the adapted transcriptome-wide HT method successfully mapped cardiomyocyte-specific MATR3 targets.
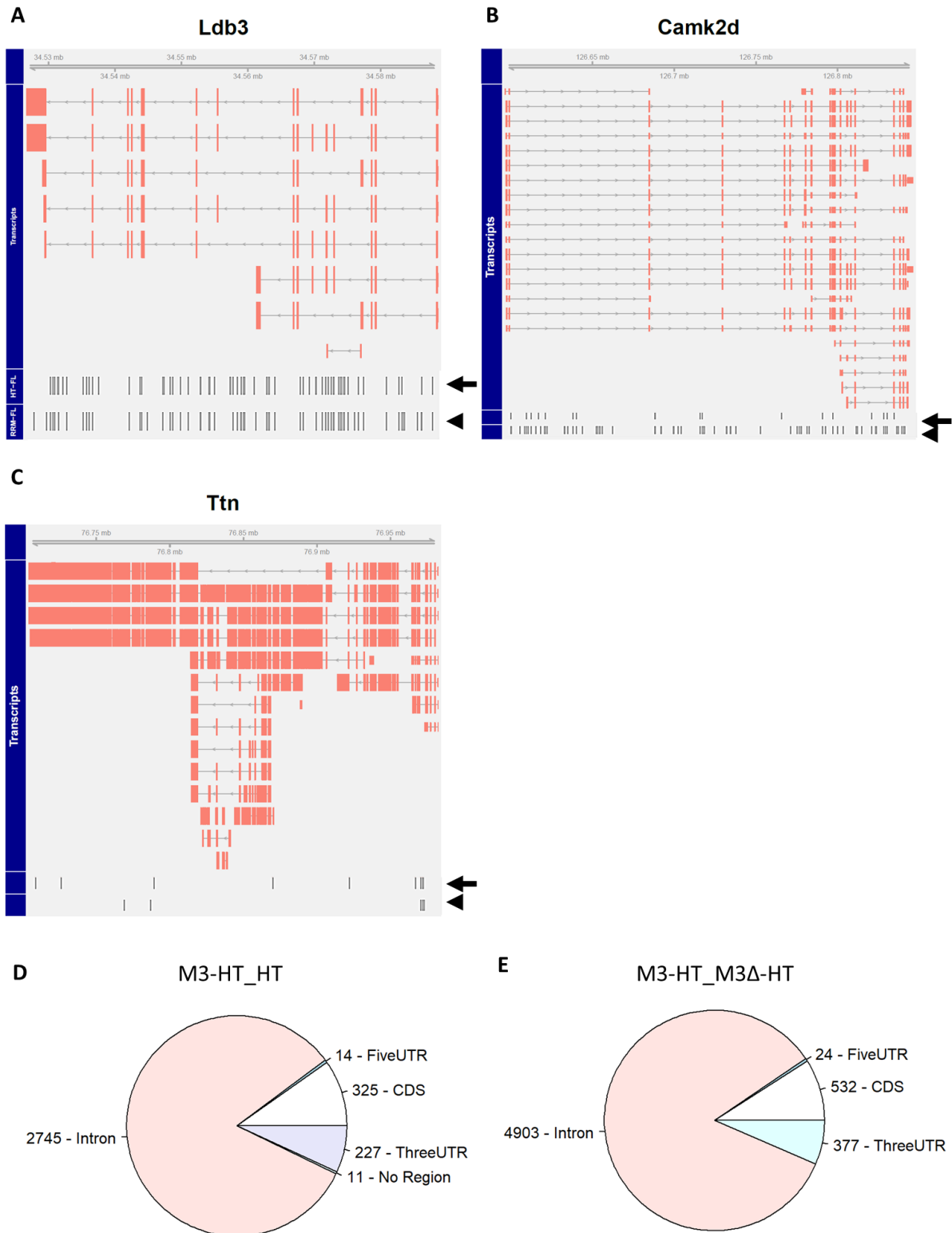
Figure 53 HyperTRIBE editing sites for MATR3 mainly cluster in intronic regions of target pre-mRNA

A-C Examples of selected genes illustrating annotated transcripts and editing tracks for either M3-HT_HT (upper track, see arrow) or M3-HT_M3Δ-HT (lower track, see arrowhead). Red bars indicate annotated exons and grey lines mark editing events. **D+E** Metagene analysis of the specific location of TRIBE edits within the pre-mRNA based on the comparisons M3-HT_HT (left) and M3-HT_M3Δ-HT (right). CDS= coding sequence. UTR = untranslated region.

MATR3 is a potential target of YAP-dependent regulation in cardiomyocytes

The density-dependent downregulation of *Matr3* (**Figure 48**, page 58) raised the question about potential upstream regulatory networks. Both MATR3 (this study) and YAP/TAZ [152] are regulated by cell-density in cell culture experiments. Under low density condition, cells co-express nuclear, transcriptional active YAZ/TAZ as well as MATR3 (**Figure 54**A). Under high density, YAZ/TAZ shuttle to the cytoplasm where they are stored or degraded. Similarly, MATR3 staining intensity declines from sparse to medium dense cell cultures and is completely absent at confluency. At high cell density, only a minority of cells express YAP/TAZ, which exactly mirrors strong MATR3 staining intensity in the few cells still showing MATR3 expression (**Figure 54**B). This co-occurrence of YAP/TAZ and MATR3 provides the first hint regarding a potential YAP/TAZ-mediated transcriptional regulation of *MATR3*. Matrin3 is listed as one of over 2.000 target genes of the YAP transcription factor in low- or high-throughput transcription factor functional studies from the CHEA Transcription Factor Targets dataset [153]. Based on these findings, we propose that YAP controls transcriptional regulation of MATR3 in cardiomyocytes and thereby also alternative splicing.
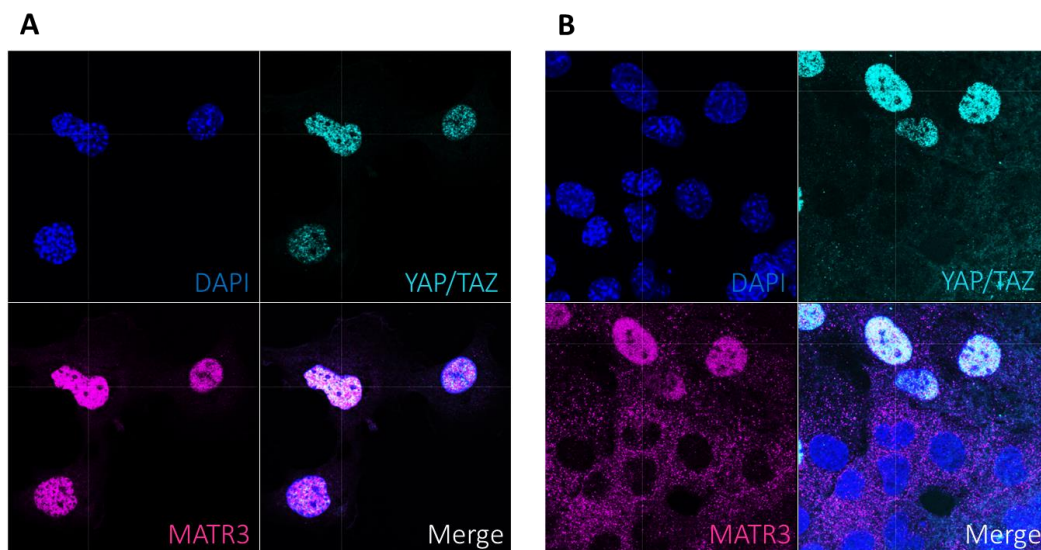
Figure 54 Density-dependent co-occurrence of YAP/TAZ and MATR3 in cardiac HL-1 cells

Co-staining of sparse (**A**) and dense (**B**) cardiac HL-1 cells with YAP/TAZ (cyan) and mouse MATR3 (purple) and nuclear dye DAPI (blue). Note the co-abundance of YAP/TAZ and MATR3 staining in some cells under dense cell confluency in B.

To prove that YAP is a bona fide upstream regulator of MATR3, a constitutively active form of YAP (YAP5SA, **Figure 55**A) was conditionally overexpressed from the ROSA26 locus using a heart and muscle-specific Cre-driver (MCK-CRE). YAP5SA contains mutations of five selected Serines to Alanines (5SA) resulting in a constitutively active form of YAP. By using YAP5SA overexpression hearts, YAP-activated transcription of representative well-characterized direct targets, as well as Matrin3, was analyzed. Since endogenous *Yap* and

Matr3 expression gradually decline during heart maturation [94], [154], hearts of 3-week-old YAP5SA-MCK and littermates were analyzed.

Western blots confirmed a significant increase in YAP levels in YAP5SA-MCK hearts compared to littermates (**Figure 55**B). Concomitantly, MATR3 protein levels increases in the Yap5SA-MCK hearts, although this increase was not statistically significant, probably due the low number of replicates. However, qRT-PCR confirmed a significant upregulation of *Yap, Matr3* and the downstream targets *Ctgt* and *Cyr61* in YAP5SA-MCK hearts (**Figure 55**C), suggesting a direct transcriptional regulation of Matrin3 by YAP5SA. Although several cardiac stress response markers are upregulated in 3-week-old Yap5SA-MCK hearts (**Figure 55**C), no obvious pathological alterations were observed (data not shown). Taken together, our data correlate regulation of *Yap* and *Matr3* in cardiomyocytes, indicating that Matrin3 represents a potential YAP downstream target. Further studies are needed to reveal the mechanism in more detail.
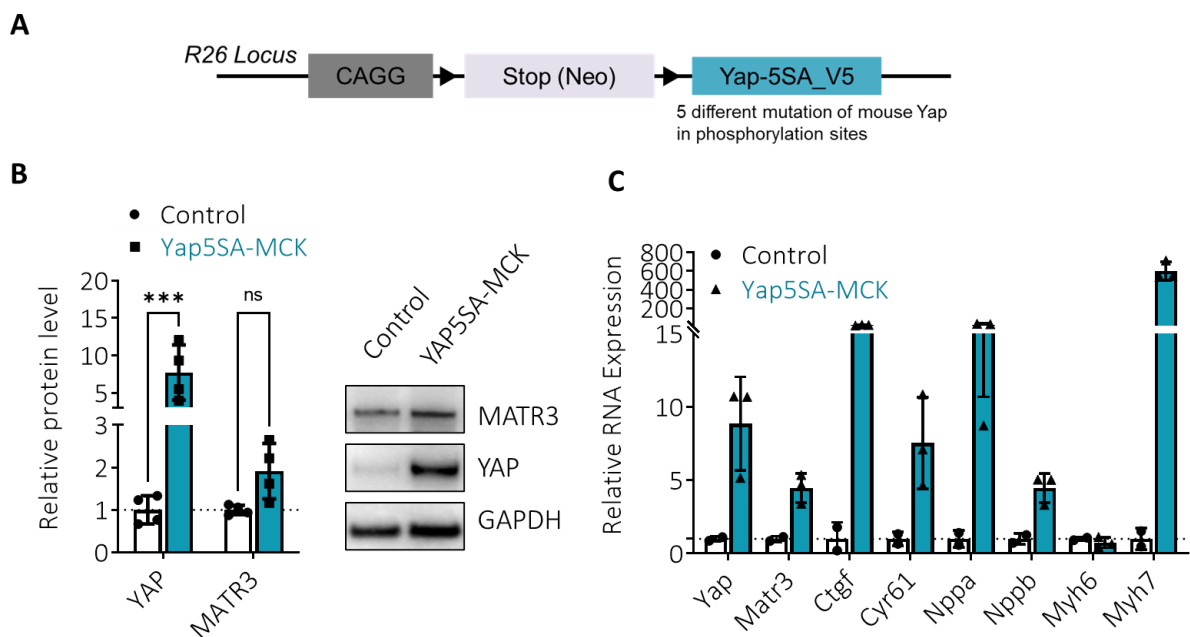
Figure 55 *Matr3* is a YAP5SA target in juvenile cardiomyocytes

A Scheme of YAP5SA transgenic overexpression mouse line, harboring a loxP-flanked Neo-STOP cassette and a V5-tagged murine YAP5SA in the ROSA26 locus. **B** Representative Western blot and quantification of YAP and MATR3 protein levels in YAP5SA-MCK and control hearts (n=4). Data represent the mean ± SD. Two-way ANOVA with Šídák's multiple comparisons test. ns = not significant, ***P < 0.001. **C** qRT-PCR of YAP5SA-MCK (n=3) and control left ventricles (n=2) for *Yap* and *Matr3*, as well as for canonical targets (*Ctgf* and *Cyr61*), and cardiac stress response markers (*Nppa*, *Nppb*, *Myh6* and *Myh7*). Control animals were single heterozygous for either Rosa-CAG or MCK-Cre.

MATR3 is not altered in cardiac biopsies from human individuals with defined pathologies

Disease-causing hMATR3 mutations are extensively linked to distal myopathy 2 and amyotrophic lateral sclerosis (ALS) patients lacking cardiac manifestations [155]. However, cardiac symptoms were described. In contrast, genomic expression profiling of human inflammatory cardiomyopathy (DCMi, also known as myocarditis) revealed a 2.4-fold upregulation of *hMATR3* in DCMi cardiac biopsies compared to controls [156]. To investigate a potential correlation of hMATR3 protein alterations in human heart diseases, left ventricular cardiac biopsies were analyzed for altered hMATR3 staining patterns and localization. Cardiac biopsies of explanted hearts were obtained from randomly selected human patients suffering from myocarditis (DCMi), coronary heart disease (CHD), dilated cardiomyopathy (DCM), and ischemic cardiomyopathy (ICM). Biopsies from patients with aortic stenosis, which is an abnormal narrowing of the aortic valve, were used as non-heart failure control to monitor normal Matrin3 abundance in human hearts. Notably, these patient samples were not assessed for genomic mutations, especially in the *hMATR* gene locus. Biopsies were analyzed in both cross-sectional and longitudinal orientations and immunostained for hMATR3. In summary, no alterations in hMATR3 abundance or localization were observed in these heart-failure patients (**Figure 56**). In DCMi samples, the majority of myocardial infiltrating cells were MATR3^{pos}. Thus, the infiltrating MATR3^{pos} immune cells might explain the increased *hMATR3* expression in human DCMi cardiac biopsies [156]. Our preliminary analysis only included a small group of patients and does not exclude that hMATR3 abundance or localization changes in human heart diseases.
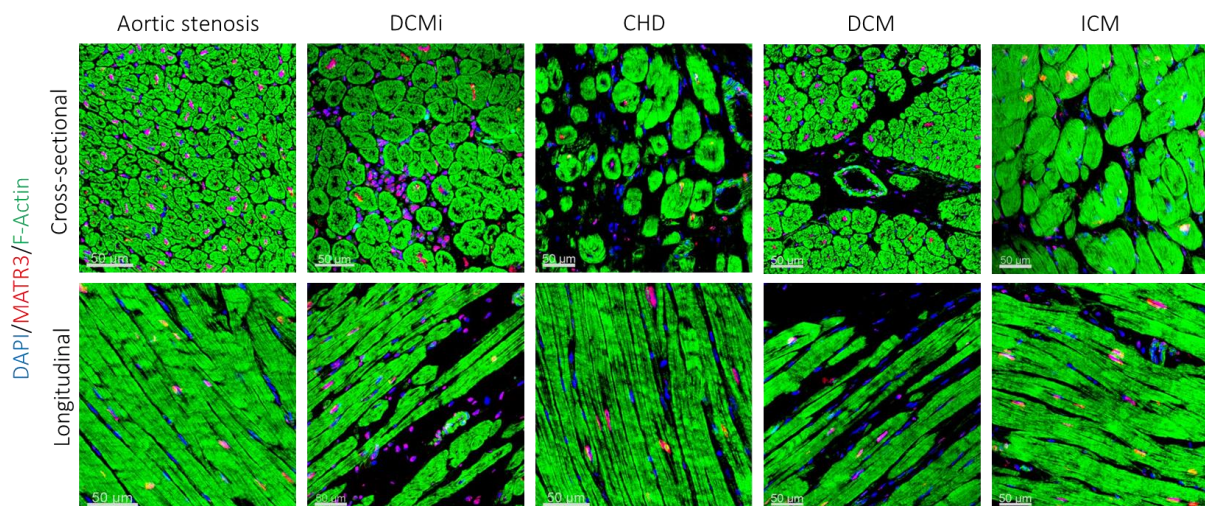
Figure 56 Matrin3 in human cardiac biopsies with different heart diseases

Human cardiac biopsies from patients with indicated heart diseases were stained for MATR3 (red), F-Actin (green) and nuclear marker DAPI (blue). Scale bar 50 µm. DCMi: myocarditis, CHD: coronary heart disease, DCM: dilated cardiomyopathy and ICM: ischemic cardiomyopathy.

Discussion

The genetic background has a strong impact on the RBM20-KO heart phenotype

RBM20 is by far the best-studied splicing factor in cardiomyocytes, since *Rbm20*-deficient rats and humans harboring *RBM20* missense mutations develop DCM with fibrosis, reduced contractility, and arrhythmia. However, we demonstrate that loss of murine *Rbm20* on the C57Bl/6J genetic background does not result in DCM and premature death. This is in contrast to a previously published *Rbm20*-KO mice strain generated on an FVB genetic background. Remarkably, both, C57Bl/6 and FVB are inbred mouse strains. In general, accumulated mutations and genetic modifiers determine the outcome of phenotypes in inbred mouse strains. In the context of the heart, phenotypic divergence in the FVB and C57BL/6 strains has been investigated in terms of e.g. cardiac mass and heart rate [157], [158] as well as susceptibility to ventricular arrhythmias [158] and even wound healing after myocardial infarction [159]. Based on these studies, we conclude that the genetic background modifies phenotypic severity in the RBM20 loss-of-function mouse model.

The differences between C57/BL6 and FVB strains after Rbm20 deletion do not seem to relate to the appearance of the mutant N2BA-G Titin isoform, which is present in both genetic backgrounds. Furthermore, the mutant N2BA-G Titin isoform does also occur in Matr3 mutants without causing adverse effects on adult mouse hearts. The data seem to suggest that the effects of N2BA-G Titin are species-specific and differ between the mouse compared to rats and humans. The three species exhibit major differences e.g., regarding the heart physiology including heart rate and arrhythmia susceptibility. Humans and rats have a lower heart rate than mice, which might enable to cope better with the adverse effects of the mutant N2BA-G Titin isoform seen in other species. In addition, reported disparities in the transcriptome, myocardial stiffness, compliance of cardiomyocytes or structural parameter account for the differences between mice and humans [160]–[163].

In contrast to the previously reported ultrastructural changes in RBM20-KO rats [102], our RBM20-mice did not show pathophysiological and ultrastructural changes such as fibrosis, but absence of the p-wave combined with irregular RR intervals in the ECG, indicating atrial fibrillation. In addition to ventricular arrhythmia, atrial fibrillation pathophysiology is widely reported for human and rodents with RBM20 mutations [103], [106], [135], [136].

Currently, we do not know why mice develop atrial fibrillation after inactivation of Rbm20 but no DCM. It might be relevant that humans and rats generate only one RBM20 isoform [32], whereas two isoforms are expressed in mice [164], but since deletion of the Rbm20 gene

prevents expression of both isoforms in mice, it is difficult to formulate a specific hypothesis. Despite this limitation it is clear that the pathological effects of Rbm20 deficiency strongly depends on the genetic background, with exception of atrial fibrillation. In contrast to the *Rbm20* knockout, cardiomyocyte-specific knockout of *Matr3* leads to a profound heart phenotype in C57BL/6J genetic background.

Similarities and differences of paralogues RBM20 and MATR3 in cardiomyocytes

Paralogous RBP families and their targets have been widely studied in the past since family members tend to exhibit functional redundancies [165]. Overlapping functions of the paralogs MATR3 and RBM20 have not been investigated so far, although both genes have been linked to myopathies [84], [132] and act as splicing repressors [89], [92]. In general, paralogous genes are often expressed in distinct cell lineages; however, *Rbm20* and *Matr3* are co-expressed in cardiomyocytes.

In this study, we identified MATR3 as a crucial splice factor for postnatal heart development and function. We demonstrate that a critical perinatal switch from fetal to adult splicing program is missing in *Matr3*-deficient hearts leading to partial maintenance of the fetal gene program in adults. Ablation of *Matr3* in cardiomyocytes leads to dilated cardiomyopathy and premature death, whereas the loss of *Rbm20* on the same genetic background does not induce premature lethality despite atrial fibrillation (**Table 1**). Our data indicate that paralogous MATR3 and RBM20 exert partially redundant functions.

First and most strikingly, both splicing repressors have common and exclusive RNA and splice targets, arguing for an overlapping function in respect of AS. Overall, MATR3 binds hundreds of cardiac (this study) and neuronal transcripts [117], revealing cell-type specific RNA regulatory networks. Furthermore, we detected a remarkable overlap with RBM20-spliced transcripts including TTN, although only the loss of RBM20 and not MATR3 leads to the generation of a giant TTN isoform. Overall, it is striking that different RBPs (hnRNP U, SRSF1, RBM20, MATR3) concomitantly regulate the splicing of common target genes (e.g. *Camk2d* and *Ttn*, [166]), highlighting the complexity and necessity of tightly-regulated and partially redundant alternative splicing regulation of cardiac transcripts to maintain cardiac function, as well as the contribution of mis-splicing to the progression to heart failure.

Second, we showed that the simultaneous deletion of cardiac MATR3 and RBM20 amplifies the hypotrabeculation phenotype, concomitant with earlier lethality in dKO compared to the single knockouts (**Table 1**). The dKO phenotype might be based on a combination of MATR3- and RBM20-exclusive effects within cardiomyocyte, resulting in a stronger phenotype. In combination with *Mart3*-dependent effects, we postulate that giant TTN variant

N2BA-G is the major driver of their neonatal lethality in the dKO compared to the single Matr3-cKO, since the neonates cannot adapt to the increased postnatal cardiac load. Measurements of cardiomyocyte contractility are necessary to address the elasticity of the differentially spliced molecular spring regions in isolated cardiomyocytes of our single and double knockout mice.

Table 1 Summary of the findings regarding MATR3 and RBM20 single and double knockout mouse lines. Table was partially created with BioRender.com.

	Healthy mice	RBM20-KO	MATR3-cKO	dKO
Lethality	life expectancy of 2 years	normal life expectancy	three weeks after birth	around birth
Cardiac phenotyp				
Differentially expressed genes	reference	180	2.625	1.933
Alternatively spliced transcripts	reference	84	92	131
TTN variant at E18.5	N2B>N2BA	N2BA-G	N2B<N2BA	N2BA-G

Third; since both paralogs own similar RNA binding motifs, bind identical sequences and direct AS of a selected splice site. In order to gain further mechanistically insights, direct RNA binding consensus sequences should be analyzed at single nucleotide resolution by iCLIP in the future, since identification and comparison of the direct binding sites in relation to the LSV was not addressed in this study.

Forth, *Matr3* and *Rbm20* exhibit differential expression patterns during cardiogenesis and cardiomyocyte maturation, arguing against complete functional redundancy at all developmental stages of cardiomyocytes. MATR3 gradually declines during cardiomyocyte maturation [94], whereas *Rbm20* levels remain mostly unaltered [93], although differential expression of *Rbm20* was monitored in heart failure patients [92]. Furthermore, *Rbm20* is exclusively expressed in striated muscle cells, whereas MATR3 is expressed more broadly.

Consistent with the expression profile in wildtype mice, embryonic but not postnatal knockout of *Matr3* in cardiomyocytes leads to heart malformations and failure. Based on these findings, we postulate that MATR3 is mainly required for embryonic cardiogenesis than for cardiomyocyte maturation or homeostasis.

Fifth, MATR3 and RBM20 single knockout (as well as MATR3 overexpressing) cardiomyocytes do not exhibit transcriptional adaptation of the respective paralogue, which is a common mechanism of genetic compensation among paralogous genes [167], [168] even in the same murine tissues [169]. At present, we cannot exclude that other RBPs with similar functions as Matr3 and Rbm20 compensate for AS at splice site normally occupied by Matr3 and Rbm20.

Lastly, we provide evidence for different upstream regulatory pathways for both paralogs (see page 78).

The study faces some limitation due to the bioinformatic splicing analysis using MAJIQ. MAJIQ is working with thresholds and as a result, some interesting candidates are below the significance threshold in one or another KO group. To overcome the necessarily of short-read alignment, future AS splicing analysis will be carried out by new next-generation approaches generating full-length transcript sequences. Both, PacBio Isoform Sequencing (Iso-Seq) or Oxford Nanopore Technologies (ONT) circumvent the assembly of single reads to detect alternatively spliced isoforms. ONT sequencing has been recently applied to investigate RBM20-dependent AS [170]. Furthermore, we have focused on MATR3-dependent conventional (linear) splicing. Since RBM20 is required for the formation of circRNA isoform of titin, it seems prudent to identify potential roles of MATR3-dependent circular RNAs formation.

In addition, it needs to be mentioned that we have not addressed potential binding of MATR3 and RBM20 to DNA in this study; although both proteins encode DNA-binding domains. It is proposed that the RBM20-dependent splicing factory is an example of trans-interacting chromatin domains functionally involved in the regulation of gene expression [98]. However, so far, no study indicates that RBM20 is directly acting on chromatin organization and transcriptional control. In contrast, MATR3 is able to bind to certain promoters in human iPSCs and mice [171], [172], indicating a potential regulatory function as DNA-binding protein at least in certain cell types. Future experiments uncovering the genome-wide DNA interaction of MATR3 (using CUT&RUN sequencing [173] or ChIP-Seq) might elucidate the impact of MATR3 as DNA-binding protein in contrast to RBM20.

Contribution of alternatively spliced targets to the MATR3-related DCM phenotype

The loss of MATR3 and RBM20 results in mis-regulation of alternative splicing of sarcomeric transcripts including TTN, CAMK2d and LDB3, which have been linked to splice defect-associated cardiac diseases in the past (reviewed in [174]). Titin is by far the most prominent splicing target of RBM20 and the loss of splicing repressor RBM20 leads to aberrant inclusion of multiple exons resulting in the expression of the largest reported TTN isoform called N2BA-G. However, it has been shown that additional splice factors contribute to TTN splicing, e.g. SLM2 [175] and hnRNP U [166], increasing the complexity of titin splicing pattern. Since the titin pre-mRNA harbors over 300 spliced exons, this transcript is in general prone to attract splice factors. In addition, mis-splicing has a major impact on cardiac compliance, since Titin is the third most abundant protein following actin and myosin

Under physiological conditions, two titin isoforms (fetal, compliant N2BA and adult, stiffer N2B) are co-abundant in the sarcomere of cardiomyocytes. Under physiological conditions, the large cardiac N2BA isoform is rapidly replaced by the smaller N2B isoform after birth. This change in titin isoform expression influences the elastic properties of the myocardium to ensure efficient filling of the left ventricle and thereby blood supply for the entire body. As known from the literature, the deletion of N2B region [176] or PEVK elements [177] of Titin elevates passive tension accompanied by diastolic dysfunction. Under pathophysiological conditions such as DCM, an elevated N2BA/N2B ratio has been previously described [76], [178], which is consistent with our observation in the MATR3-KO-driven DCM. In this study, we demonstrate that MATR3 directly regulates Titin splicing through binding to distinct regions. Subsequently, *Matr3* depletion in cardiomyocytes results in an elevated N2BA/N2B ratio and this might manifest in altered sarcomere stiffness of the perinatal MATR3 knockout hearts, impairing their contractility. While the loss of *Matr3* is not sufficient to generate the titin giant isoform N2BA-G, RBM20 remains the only determinant to splice out the corresponding TTN region. Taken together, the paralogues RBM20 and MATR3 share the giant protein TTN as a common target, although loss of the respective RBP has different effects on titin isoform composition.

Another example of Matr3 deficient mis-splicing is LDB3 (Z-line protein LIM domain binding 3). In mice, the cardiac-specific ablation of LDB3 results in premature death due to either congenital myopathy [179] or late-onset DCM with disrupted cardiomyocyte ultrastructure and decreased cardiac function [180]. In patients, mutations (mainly within exon 5 and 6, which is only lowly expressed in the heart, [181]), as well as abnormal alternative splicing [144], has been linked to DCM. Interestingly, loss of MATR3 and RBM20 leads to mutually exclusive inclusion of exons 5–7, which are usually expressed in skeletal muscle isoforms of

LDB3. However, RBM20 seems to be exclusively responsible for differential inclusion of exon 4, since only the loss of RBM20 but not MATR3 results in exon 4 exclusion. Therefore, MATR3 and RBM20 exhibit a redundant and non-redundant function for the LDB3 pre-mRNA. Since LDB3 is located in the Z-line of sarcomeres and is crucial for their stability [179], altered isoform composition during cardiogenesis presumably impairs heart function and contractility in our mouse models.

As a third example, we had a closer look at CaMKII, which is composed of four different chains, namely alpha, beta, gamma, and delta. As Calcium/calmodulin-dependent protein kinase, it is regulating Ca^{2+} homeostasis and excitation-contraction coupling. Overall CaMKII activity is increased in hypertrophied and failing myocardium [182], [183]. For *CamkIId* (delta), the loss of functional RBM20 results in skipping of exon 14 and concomitant inclusion of exons 15 and 16 [32]. Since exon 14 encodes the nuclear localization signal, CaMKIId shifts from the nucleus to the cytoplasm [32]. Thereupon, calcium handling is disrupted in human and murine *Rbm20*-deficient cardiomyocytes, resulting in proarrhythmic calcium releases from the sarcoplasmic reticulum [103] and presumably manifesting in atrial fibrillation. Interestingly, it has been postulated that MATR3 itself is a Ca^{2+}-dependent CaM-binding protein and a downstream substrate of caspases, thereby modulating both Ca^{2+}-dependent interaction with calmodulin and caspase-mediated cleavage *in vitro* [184]. To further examine a potential calcium imbalance, Ca^{2+} measurements and stimulations could be recorded in isolated cardiomyocytes of *Matr3* and *Rbm20*-knockout mice. In addition, AS of CaMKIId is of particular interest, because it binds and phosphorylated the PEVK and N2B-unique sequence of titin [185], [186]. Although the relevance of CaMKII-dependent TTN modifications for cardiomyocyte structure and function still needs to be investigated [187], the lack of functional CaMKII might not only result in calcium imbalance, but also in an altered TTN phosphorylation of *Matr3*-deficient cardiomyocytes, which could be further analyzed by *All-Titin Phosphorylation Assays* [186].

In the future, the impact of a certain alternatively spliced target can be further addressed by mouse model expressing aberrant, alternatively-spliced isoforms, which might resemble hypotrabeculation and lethality as observed in the Matr3-cKO. On the other hand, certain mis-spliced sites could be restored to partially rescue the DCM phenotype caused by MATR3-deficiency.

Successful establishment of the HyperTRIBE method in cardiomyocytes using transgenic mouse lines

In previous studies, the TRIBE method was used to identify RNA targets of multiple RBPs in *Drosophila* and human cells [22]–[26], but the methods has not been used in primary mouse

cells *in vitro* or in mice *in vivo*. In this study, we generated transgenic mouse lines allowing application of HyperTRIBE *in vivo* in cardiomyocytes, resulting in the identification of hundreds of cardiac MATR3 mRNA targets. We reason that these RNAs represent high confident targets, since they contain more than one A-to-I editing event per transcript, mainly within introns. The accumulation of multiple editing events per transcript is in contrast to previous studies, since especially the first generation of TRIBE marked the majority of targets by one single editing site, although the whole transcriptome including intron-containing pre-mRNA was analyzed [22]. Since our HT mice display no obvious pathophysiological alterations and are viable, we assume that HT-induced edited sites within introns are spliced out during pre-mRNA processing and will most likely not impair mRNA stability, cause amino acid alterations or nonsense-mediated mRNA decay (NMD).

The MATR3-HT fusion selectively marks approximately 10% of all sequenced transcripts, which is consistent with a previous report showing that MATR3 binds thousands of RNAs [117]. However, since we used an overexpression approach, random binding upon saturation of endogenous targets might occur. Initially, it was unclear which of the two background controls (catalytic domain or RRM-depleted MATR3 variant fused to the catalytic domain) would be more suitable and both were processed in parallel. Just like the HT fusion protein from full-length MATR3, the MATR3-delta variant is expressed at high levels and associated DEGs, whereas HT (catalytic domain of ADAR) can be used as unique control independent of the fused RNA-binding protein of interest. Therefore, we conclude that both controls have pros and cons and both should be taken into account when defining high confident targets.

Notably, the catalytic domain of ADAR can only perform A-to-I(G) editing in a one-directional way, whereat the reversion from G-to-A has not been described. Nevertheless, some rare events of G-to-A were identified, which are probably due to sequencing or alignment errors, somatic mutations, or differences in the genetic background of the mouse lines, since HT mouse lines have not yet been backcrossed into a clean C57Bl/6J background. In the future, implementation of an existing single nucleotide polymorphism (SNP) database (e.g. dbSNP [188] or Mouse SNP Miner [189]) in the bioinformatic pipeline might further discriminate edits and SNPs.

Due to the three-dimensional structure of RNAs, A-to-I editing events might occur at some distance from the binding sites, therefore a transcriptome wide Matr3 binding motif analysis was not implemented. In principle, binding sites of RBPs at single-nucleotide resolution can only be identified via the iCLIP method, but it has been reported that TRIBE editing reflects the pattern of CLIP signals and corresponding metagene quantification of the location for different proteins including *Drosophila* Hrp48, FMR1 and NonA [22]. In our study, most editing sites were mapped to introns which are in general larger than exons and therefore,

might accumulate more edits. In addition, the enrichment of editing sites in introns might reflect the binding specificity of the MATR3 [89], [90]; although HT-Editing does not label the precise binding site of an RBP. Despite the disadvantages and limitations mentioned above, we have identified bona fide targets of MATR3 in cardiomyocytes by HyperTRIBE. To validate the specific editing events of individual targets, Sanger sequencing of cDNA and corresponding genomic DNA needs to be performed from the same individuum.

A limiting factor is that HyperTRIBE does not mark the direct binding site at single-nucleotide resolution. To target precise binding sites, we are still aiming to perform CLIP experiments using an endogenous antibody MATR3 in HL-1 cells. The use of HL-1 cells provides sufficient cell numbers and high expression of both RBPs, enabling CLIP experiments. To eliminate secondary binding of the endogenous antibodies, siRNA-mediated knockdown of MATR3/RBM20 in HL-1 cells could be used as background binding control. Once iCLIP data for MATR3 in HL-1 cells is available, the position of CLIP peaks can be compared to HyperTRIBE editing events and to published RBM20 CLIP data [32] [92].

One aspect that was not taken into account in this study is that MATR3 itself was recently associated with adenosine-to-inosine (A-to-I) editing - at least in human myelogenous leukemia cell line K562 cells [190]. By combining RNA-sequencing and global protein-RNA binding data, the screen revealed a small number of RBPs, which were associated with considerable editing changes upon knockdown [190], including MATR3. To address whether MATR3 is involved in RNA editing *in vivo*, different cell types of our loss- and gain-of-function mouse model could be analyzed for MATR3-dependent RNA edits by the JACUSA pipeline in the future. However, such an approach will not reveal whether the lack of MATR3-dependent editing causes functional changes *in vivo*, or whether the alternatively spliced MATR3 targets are responsible.

Endothelial subtypes respond differently to the loss of MATR3

The Matr3(Gt-ex13) homozygous gene trap allele that disrupts the 3′UTR portion of the gene, leads to early embryonic lethality before E4.5 in mice [94]. Heterozygous mice with lower MATR3 protein levels exhibit incompletely penetrant bicuspid aortic valve, aortic coarctation, and patent ductus arteriosus [94]. In comparison to the gene trap mouse model, our constitutive deletion of *Matr3* leads to embryonic lethality in the third trimester, leading to defects in the development of blood and lymphatic vasculature as well as to reduced trabeculation and cardiac stress response. However, no defects of the outflow tract were observed in heterozygous mutants (data not shown). Remarkably, not all investigated cell types are affected by the loss of MATR3, which is evident by the unaltered pericyte coverage during skin vascularization. Since multiple cell types are affected by the global loss of

MATR3, we did not pursue an analysis of alternative splicing in germ line mutants but switched to a model of cell type-specific Matr3 inactivation.

Regarding a cell-type-specific function, a previously reported cell culture study claimed that MATR3 exerts key regulatory functions in endothelial for cell survival, as indicated by reduced proliferation and increased necrosis in *Matr3*-depleted human EA.hy926 cells[110]. These observations are in stark contrast to our study, which relies on knock down of Matr3 in HUVEC cells and on the use of endothelial-specific knockout mice. The hybrid cell line EA.hy926 was established by fusing primary human umbilical vein cells with a thioguanine-resistant clone of A549 by exposure to polyethylene glycol (PEG) [191]. In contrast, HUVECs are primary cells (in our case) from pooled donors. Although EA.hy926 show endothelial Weibel-Palade bodies and display other characteristics of differentiated endothelial cell, differences between common models (primary human aortic or umbilical vein endothelial cells) and EA.hy926 cells have recently been described, especially in respect to gene expression [191], [192]. For example, the expression of endothelial *von Willebrand factor* (vWF), VEGFR1, and VEGFR2 is significantly lower in EA.hy926 cells compared to primary endothelial cells [191], [192]. Moreover, gene expression of *Matr3* in these cells (EA.hy926 compared to primary endothelial subtypes) has not been assessed so far. In general, effects mediated by siRNA knockdown might be different, depending on endogenous gene expression of the gene of interest (here MATR3 and effected transcripts), as well as on the number of passages, and cell density. To confirm our observation that loss of MATR3 promotes hyperproliferation exclusively in HDLECs but not in HUVECs, HUVECs from different donor groups might be treated with siMATR3 and subsequently analyzed.

In vivo studies, addressing the responsiveness of endothelial subtypes upon *Matr3* depletion, have not been published so far. In this study, we discovered that *Matr3*-null embryos exhibit subcutaneous edema and severe defects in lymphangiogenesis. In contrast, the effects of global Matrin3 inactivation on blood vessels are rather moderate. Within the dermis of Matr3-KO mice, the loss of *Matr3* resulted in increased LEC proliferation and vessel enlargement, revealing that MATR3 is required to coordinate precise lymphatic network branching in the embryonic skin. Due to hyper-proliferation, LECs presumably fail to build up network and connect, resulting in reduced lymphatic network branching complexity, as well as insufficient drainage of lymphatic fluid from the interstitium. To further monitor the lymph fluid uptake, FITC-dextran and Evans blue dye lymphangiography might open up an opportunity to test the drainage function during fetal or newborn stages [193], [194]. This future experiment will not only show that the structure of the lymphatic network is impaired in KOs, but also whether lymph fluid uptake is compromised.

To identify the cellular lineage which is causative for the edema phenotype in Matr3-*null* embryos, vascular and lymphatic endothelial cell-specific *Matr3* knockout models were analyzed. First, we made use of the Tie2-Cre deleter strain expressing Cre from the receptor tyrosine kinase Tek (Tie2) locus [137], which showed efficient inactivation of *Matr3* in vascular but not in LECs. In general, the receptor tyrosine kinase Tie2 is predominantly expressed by vascular endothelial [195] and hematopoietic cells [196]. Although Tie2 signaling is crucial for BECs and LECs development [197], [198], most embryonic LEC clusters are not targeted by either the Tie2-Cre transgene [42], [199] or by Tie2-GFP reporter mice [200]. Especially the origin of dermal lymphatic vessels does not depend on Tie2-linage venous-derived LECs [42] and thereby Tie2-driven Cre recombination is less active or even inactive in LECs. Matr3[EC-cKO] knockout mice are viable and do not phenocopy the mild vascular phenotype from *Matr3*-null embryos, revealing that vascular endothelial-specific knockout of *Matr3* has no obvious effect on angiogenesis.

In contrast, the LEC-specific Matrin3 cKO reproduce the subcutaneous edema from *Matr3*-null embryos. We made use of the Lyve1-eGFP-hCre to deplete *Matr3* specifically in LECs. At E15.5, Matr3[LEC-cKO] recapitulate the lymphatic defects evident in *Matr3*-null skins, whereas the structure and size of their jugular lymph sacs have not yet been investigated until now. However, a proportion of Matr3[LEC-cKO] survived to adulthood due to a mosaic expression pattern of eGFP-Lyve1-Cre, which has not yet been described in the literature so far. Since already the partial Lyve1-mediated inactivation of Matr3 induces malformation of the lymphatic network in Matr3[LEC-cKO], the complete loss of *Matr3* in all LECs might may have more dramatic consequences, including subcutaneous edema and embryonic lethality. In the future, the knockout efficiency in edematous and non-edematous Matr3[LEC-cKO] samples could be further determined using FACS-sorted LECs, followed by qRT-PCR specifically analyze effects of *Matr3* in GFP[pos] and GFP[neg] populations. Taken together, knockout of *Matr3 in vivo* induces a severe lymphatic phenotype in both constitutive and LEC-specific Matrin3 knockout mice.

Since *Lyve1* expression is not restricted to LECs, the contribution of additional Lyve1^{pos} cell lineages needs to be taken into account when using the Lyve1-eGFP-hCre driver, in particular macrophages and endocardial cells. First, macrophages need to be considered, because they can stimulate or inhibit lymphangiogenesis [139], [201]. It is well known that Lyve1^{pos} macrophages define dermal lymphatic vessel diameter during development by regulating LEC proliferation [138], although they are not the major source of lymphangiogenic growth factors, such as VEGF-C, in the embryonic dermis [138]. In this study, we have demonstrated that macrophages are targeted by the Lyve1-eGFP-hCre in the embryonic skin. To rule out an impact of macrophages on the lymphatic phenotype of our conditional Matr3[LEC-cKO], knockout validation and marker gene expression in FACS-sorted

CD45^pos^/LYVE1^pos^ macrophages should be addressed. Inactivation of Matrin3 in macrophages using LysM-Cre mice will reveal whether the absence of Matr3 in macrophages has any effect on lymphangiogenesis [202]. In addition to macrophages, endocardial cells need to be considered, since they express *Lyve1* at low levels throughout embryogenesis [138], [201]. To rule out the impact of the endocardium on the observed phenotype, conditional Matr3^LEC-cKO^ embryos should be screened for heart defects and pericardial edema.

The current challenge we are facing is to determine the cell-type-specific molecular function of MATR3 in endothelial subtypes. BEC and LEC represent two distinct endothelial cell populations but obviously, LECs are more affected than BECs by the loss of *Matr3*. Therefore, we postulate that MATR3 might be a key alternative splice regulator in the lymphatic endothelium. Since MATR3 represents an RNA-binding protein, the identification of LEC-specific mRNA targets will be crucial. For this purpose, the HyperTRIBE method in combination with FACS-sorted primary BECs and LECs will be applied to identify pan-endothelial and BEC/LEC-specific mRNA targets.

Until now, it is not known which splice factors regulate crucial AS networks of lymphangiogenic genes, in particular *Prox1* and *Vegfr-3*. Therefore, it will be fundamental to identify potential alternative spliced isoforms of key lymphatic genes upon the loss of splice factor MATR3. However, the number of primary FACS-sorted BECs and LECs is limited for RNA seq, validation, and functional assays such as cell migration, tube formation, and spheroid sprouting assays. To overcome this issue, HUVEC and HDLEC cell lines need to be used, which are suitable for this type of analysis, since they partially mimic the effects of the loss of Matrin3, in particular regarding proliferation.

Matrin3 links alternative splicing and Hippo signaling

In this study, we demonstrated upregulation of *Matr3* levels in constitutive active YAP-overexpressing hearts, concomitant with transcriptional activation of well-established YAP targets, uncovering MATR3 as a direct target of YAP *in vivo*. In brief, YAP/TAZ signaling is involved in tissue homeostasis due to organ size control, tissue regeneration, and self-renewal [133], [152], [154], [203], [204]. The Hippo cascade is a critical regulator of YAP/TAZ activity, which acts as a transducer to drive expression of target genes such as *Ctgf* and *Cyt61*. So far, no alternative splicing factors have been identified as a direct YAP target.

We did not apply published bioinformatics tools or analyzed ChIP-Seq data to identify potential regulatory regions of Matr3, since the density of the examined cells is usually not taken into account. To verify MATR3 as a direct YAP target, combined ATAC-seq with ChIP-seq from cardiomyocytes or cardiac HL-1 cells will be integrated in the future. Based on this

approach, increased chromatin accessibility and binding peaks in the *Matr3* gene in the context of constitutive YAP overexpression in cardiomyocytes would strengthen our hypothesis. Implementation of predicted DNA-binding sequences and ATAC-Seq foot printing [205] will further unveil YAP-associated transcription factors that are directly bound to *Matr3* promoter. So far, transcription factor binding sites in the *Matr3* gene promoter region comprise only IRF-1, Nkx2.5, Nkx6.1, and Pou2F1a [206], which are not known to employ YAP. Transcriptional activation via YAP is usually mediated by interactions with TEAD transcription factor family. Corresponding TEAD binding sites might be located in distant enhancers, which might be located several megabases away from the Matr3 transcriptional initiation site [204].

The upstream control mechanism regulating MATR3 expression in the heart seem to differ from RBM20, for which two main pathways are postulated. First, *Rbm20* expression is modulated by the mitogen-activated protein kinase (MAPK) pathway, mediated by the two downstream transcriptional factors c-Jun and Elk-1 (ETS Transcription Factor), which directly binds to the promoter of *Rbm20* [207]. Second, *Rbm20* can be upregulated via the PI3K-Akt-mTOR axis by stimulation with growth factors such as insulin [208], [209]. So far, no cellular density-dependent transcriptional regulation has been described for *Rbm20*. Based on our results, we hypothesize that expression of MATR3 is directly dependent on proliferation when cell density is low. To further corroborate this view, co-staining of MATR3 with proliferation markers such as Ki67 or PH3 and RNA Pol II Ser2P/Ser5P need to be done. Furthermore, we will investigate MATR3-dependent alternative splicing using cells kept either at low or high density and correlate the results to expression of MATR3-dependent RNA targets.

Future Directions

Function of MATR3 in endothelial subtypes

Primordial endothelial cells are specified into blood (BEC) and lymphatic (LEC) subtypes with unique adaptations based on their distinct function. In this study we found that the RNA-binding protein MATR3 is indispensable for lymphomagenesis, whereas the proliferation of BECs is not affected by the loss of MATR3, revealing fundamental differences in the biology of both cell populations. At the moment we cannot clarify if the different phenotype in dermal BECs and LECs is based on either a different subset of targets or if coping response mechanisms and downstream effects differ in the two subtypes upon the loss of MATR3. To explore these apparently different cellular responses, RNA-Seq data of primary MATR3-deficient LECs and BECs will be analyzed for both alternatively spliced transcripts as well as differentially expressed genes. We postulate that MATR3 might indeed specifically binds LEC-specific transcripts such as *Prox1*, *Pdpn*, or *Vegf3,* and here, HyperTRIBE could further discriminate pan-endothelial from LEC and BEC-specific targets of Matrin3. Moreover, the transcriptome analysis will reveal downstream effects upon the loss of MATR3 such as changes in the extracellular matrix composition, maturation and proliferation state as well as differentiation.

MATR3 in human diseases

The present study has revealed novel, essential functions of the RNA-binding protein MATR3 in the murine cardiovascular system, expanding the knowledge about MATR3, which previously has been primarily associated with neurodegenerative and neuromuscular diseases. Notwithstanding the new insights into the function of MATR3, further studies about the role of human MATR3 for cardiovascular diseases and the impact of disease-causing mutations in *hMATR3* gene are necessary.

In total, 10-30% of adult DCM-patients harbor mutations located predominantly in the TTN gene [210], although pediatric DCM patients display only a low mutation rate [211], leaving a gap in the understanding of disease onset and involved mutations. So far, muscle-restricted RBM20 is the only identified splicing factor causative for human familial cardiomyopathy, usually diagnosed during early adulthood [104], [212], [213]. A genetic screen that focuses on human mutations in RBPs and in particular splice factors in (pediatric) cohorts of heart disease patients might reveal new causes of cardiomyopathy in the future. Since Matrin3 is a broadly expressed splicing factor, we postulate that mutations in *hMATR3* will result in miscarriage or infant morbidity and mortality or act as a modifier, if mutations only lower but not completely lose functionality. Although a preliminary immunohistological analysis of a

small cohort of human patients did not reveal in MATR3 protein abundance localization, additional samples should be examined, especially from pediatric patients.

Since MATR3 loss promotes lymphedema formation in mice, the question arises whether Matrin3 might play a similar role in human disorders of the lymphatic system. Similar to our Matrin3 knockout mouse models, loss-of-function as well as missense mutations of *hMATR3* might cause predisposition to lymphedema in humans. So far, mutations in the human *MATR3* gene have not yet been reported for patients suffering from primary lymphedema [214]–[216]. To address the potential contribution of MATR3 for defects in lymphangiogenesis, selected samples from patients suffering from primary or secondary lymphedema could be analyzed in respect to *hMATR3* mutations and expression, or MATR3-dependent AS events. Specifically, Whole Exome combined with Whole Transcriptome Sequencing of a cohort of patients with lymphatic system malformations should be performed, as reported recently [215], [217]. Since lymphedema in Matrin3 mutants becomes evident already during embryonic stages, patients diagnosed with sporadic fetal edema (also known as sporadic in utero generalized edema) should be screened for mutations in the *hMATR3* gene, as previously reported for VEGFR2 and FOXC2 [218]. Such an approach might indicate whether *hMATR3* represents a candidate for human primary lymphedema.

Material and Methods

Animal experimentation

All animals and procedures for mouse experiments were approved by the local governmental animal protection committee (Regierungspräsidium Darmstadt). The corresponding animal proposal numbers are B2/1125 and B2/1183. Mice were housed in individually ventilated cages accompanied with environmental enrichment under specific pathogen-free conditions in the Animal House Facility of the Max Planck Institute for Heart and Lung Research, Bad Nauheim, Germany.

Mouse ES cell-based gene targeting

Targeting vectors were electroporated into V6.5 F1 hybrid ES cells (gift from Rudi Jaenisch, RRID:CVCL_C865) and targeted stem cell clones were injected into C57BL/6 blastocysts to obtain chimeric mice, which were backcrossed to the C57BL/6 background. Knockout or knock-in mice were generated using cell type-specific Cre lines (**Table 2**). ESC cell culture and transgenic service were performed by Sonja Krüger and Susanne Kreutzer (MPI-HLR, Bad Nauheim, Germany). Cardiac bodies were kindly provided by Sonja Krüger.

Table 2 Mouse strains used in this study

Strain	Reference
CMV-Cre deleter	[219]
Flp-Recombinase	[220]
HyperTRIBE Strains	Silke Kreher, Dr. Andre Schneider, MPI-HLR Bad Nauheim
Lyve1-Cre = Lyve1-eGFP-hCRE	[221]
Matr3-KO	Silke Kreher, Dr. Andre Schneider, MPI-HLR Bad Nauheim
Matr3-loxP	Silke Kreher, Dr. Andre Schneider, MPI-HLR Bad Nauheim
MCK-Cre	[142]
Rbm20-KO	Silke Kreher, Dr. Andre Schneider, MPI-HLR Bad Nauheim
ROSA26-Matr3-V5HA	Silke Kreher, Dr. Andre Schneider, MPI-HLR Bad Nauheim
Tie2-Cre	[137]
XMLC2-Cre	[141]
YAP5SA-V5	Dr. Shuichi Watanabe, MPI-HLR Bad Nauheim

Generation of constitutive Rbm20 knockout mice

The following targeting strategy was applied to generate constitutive Rbm20-LacZ knockin mice (**Figure 57**). First, a Rbm20 conditional mouse allele was generated by inserting neomycin and LacZ cassettes concomitant with loxP sites flanking exon 4 and 5 into V6.5 F1 hybrid ES cells as described. Next, founder mice were bred with CMV-Cre deleter to remove the neomycin cassette obtain the constitutive allele. Rbm20^{KO} mice were crossed at least 10 generations on C57BL/6J genetic background.
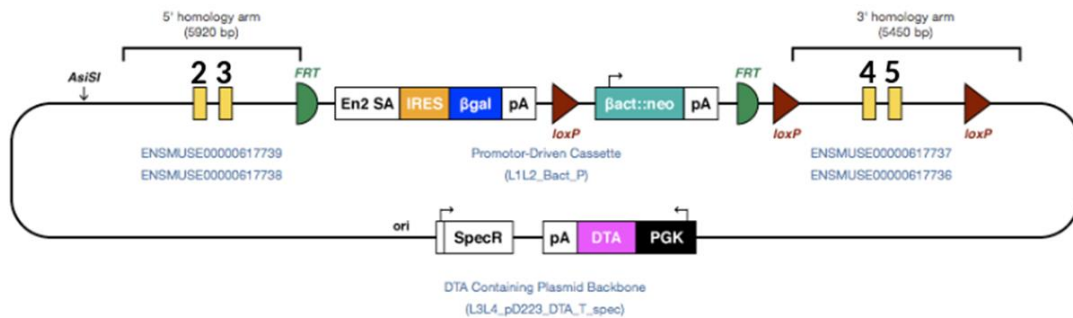
Figure 57 Targeting strategy for *Rbm20*

Generation of constitutive and conditional Matr3 knockout mice
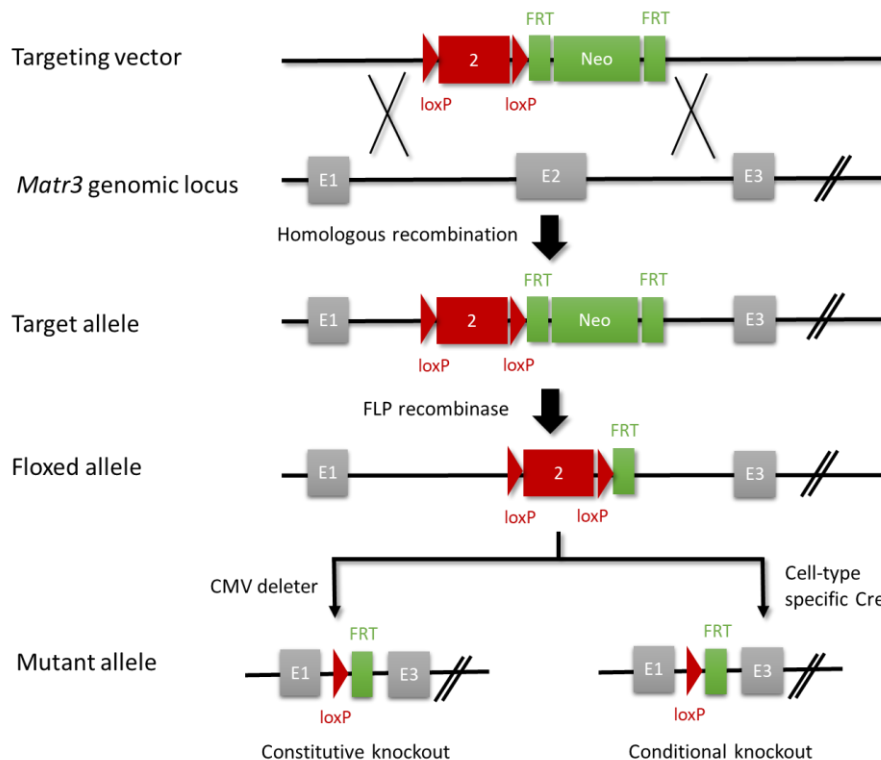
Figure 58 Generation of conditional and constitutive Matr3 knockout mice

Schematic illustration of gene targeting strategy for *Matr3*. In the targeting vector, loxP sites (red triangles) flank exon2 of the Matr3 gene (in red) and FRT sites flank the neomycin-resistance (Neo) cassette (in green). E: exon; Neo: neomycin resistance cassette. Scheme is not to scale.

Matr3 knockout mice were generated using the Cre-loxP System (**Figure 58**). In the targeting vector, two loxP sites flank exon2 of the *Matr3* gene and FRT sites flank the neomycin-resistance (Neo) cassette. Upon homologous recombination, the targeting vector flanks the second exon of gene *Matr3* by two loxP sited. The FRT-flanked Neo selection cassette was removed from the targeted allele by breeding with FLP recombinase to obtain the floxed allele. Constitutive knockout of *Matr3* was achieved by breeding Matr3^{flox/flox} mice with CMV-Cre deleter, which was then crossed out again. Conditional knockout strains were obtained by crossing Matr3^{flox/flox} with cell type-specific Cre-transgenic strains.

Generation of dKO mice

dKO mice were generated from constitutive RBM20KO and conditional MATR3-cKO mice in combination with the XMLC2-Cre.

Generation of knock-in mice by targeting the ROSA26 locus in mouse ES cells

Constitutive overexpression mouse strains were generated using ROSA26 site-specific gene knock-in (**Figure 59**). Therefore, cDNA for each gene of interest (GOI) was inserted downstream of the loxP-flanked STOP cassette in the ROSA26 locus of mouse ES cells [222]. The loxP-flanked STOP cassette is removed by Cre-mediated homologous recombination, resulting in a cell type-specific overexpression of GOI. All overexpression mouse lines were kept double heterozygous (ROSA26-CAG$^{+/-}$, Cre$^{+/}$).
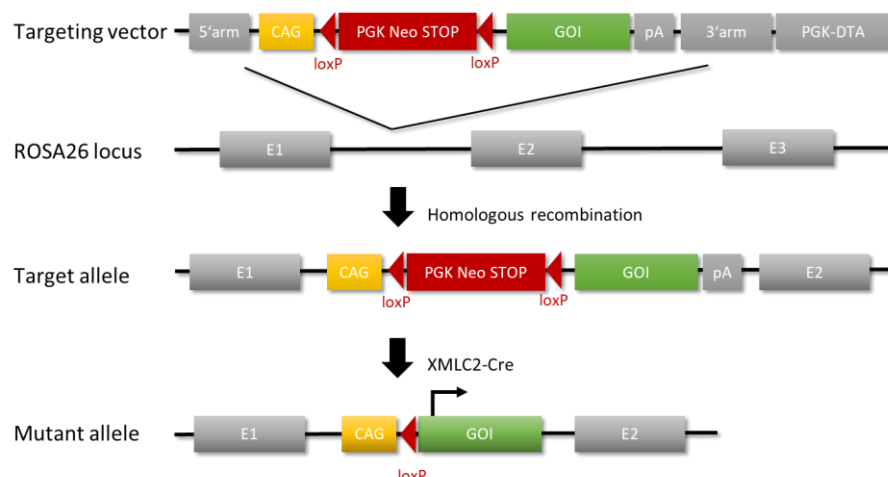
Figure 59 Schematic illustration of targeting the ROSA26 locus in mouse ES cells

The targeting vector contains the CAG promoter (in yellow), a loxP-flanked STOP sequence (in red) and cDNA for the GOI (in green), which is inserted via homologous recombination into the ROSA26 locus. Overexpression is achieved upon Cre recombinase-mediated excision of the STOP cassette. CAG: enhancer promoter; PGK: phosphoglycerate kinase promoter, Neo: neomycin resistance gene as positive selection marker; GOI: gene of interest; pA: polyadenylation sites; E: exon. Scheme is not to scale.

The genes of interest to be inserted into the ROSA26 locus are either full-length *Matr3* or RNA binding-deficient *Matr3ΔRRM* with a V5 and HA double-tag (**Figure 60**A+B) or HyperTRIBE fusions (**Figure 60**C-E; see HyperTRIBE, page 92).
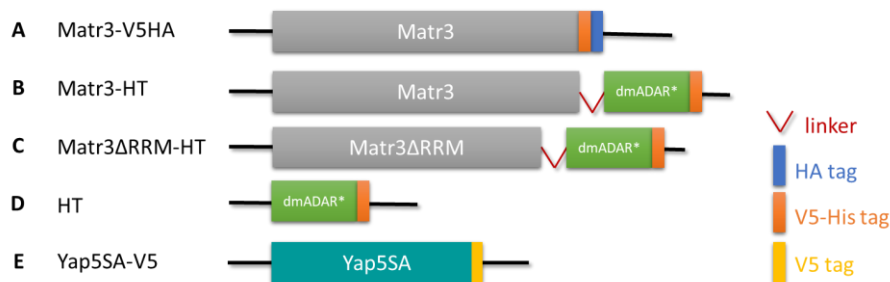
Figure 60 Schematic representation for conditional overexpression of GOIs in the ROSA26 locus

Extraction of genomic DNA for genotyping

Ear or tail biopsies were digested in 500 µL tail lysis buffer (100 mM Tris-HCl, pH8.8; 5 mM EDTA, pH 8.0; 0.2% SDS; 200 mM NaCl), supplemented with 5 µL Proteinase K (stock concentration 20 mg/ml; Catalog No. 7528.2, Carl Roth) at 56°C overnight. Lysates were centrifuged at 14,000 rpm for 10 min and decanted into a new tube containing 500 µL isopropanol and genomic DNA was precipitated. After centrifugation at 14,000 rpm for 20 min, supernatants were removed and the genomic DNA-containing pellets were washed in 500 µL 70% ethanol, followed by centrifugation at 14,000 rpm for 5 min. The genomic DNA was air-dried at RT for at least 1h, suspended in 300 µL 1x TE buffer (10 mM Tris-HCl, 1 mM disodium EDTA, pH 8.0) by incubation at 56°C overnight.

Genotyping of transgenic mice

Genotyping PCRs were performed with self-designed primers purchased from Merck/Sigma Aldrich. The master mix for one PCR reaction contained 10 µl 2× Taq Master Mix prolong (Catalog No. P111/P112, Vazyme), 10 µl ddH$_2$0, 2µl genomic DNA, and 1 µl Primer mix (final concentration: 10 µM forward and 10 µM reverse primer pair). PCR was performed in Bio-Rad thermocyclers. PCR products were loaded on a 2% agarose gel (dissolved in 1x TAE, containing 0.04 M Tris-Acetate and 0,001 M EDTA, pH 8.0), supplemented with ethidium bromide solution (Catalog No. A1152.0100, AppliChem). DNA was visualized under UV light (Transilluminator UST-30M-8R, Biostep) and documented with Intas GelDoc software.

Table 3 PCR primers for mouse genotyping

PCR	Primers
Rosa-CAG	ROSA-CAG-FOR 5'-CTT GCT CTC CCA AAG TCG CTC TGA G-3' ROSA-CAG-REV 5'-ACC GTA AGT TAT GTA ACG CGG AAC TCC-3' ROSA-WT-REV 5'-CTT TAA GCC TGC CCA GAA GAC TCC C-3'
Matr3-loxP	MATR3-1.LOXP-FOR 5'-CTG GTT CAT CTT TGA CTT GCT GACC-3' MATR3-1.LOXP-REV 5'-CAG ATT CTG AAT ATA TGC AGA GCC TGC-3'
Matr3-KO	MATR3-1.LOXP-FOR 5'-CTG GTT CAT CTT TGA CTT GCT GACC-3' MART3-2.LOX-REV 5'-GTA GCA CTT ACT CCA GTT AAG CAC ATC G-3
Rbm20-KO	RBM20-LOXP-FOR1 5'-TCT GCC GAG AGA TGG ATG CAG A-3' RBM20-LOXP-REV1 5'-CAG AAC TGA CAT GAG GTT GAG-3'
Cre	CRE-FOR 5'-CGA CCA GGT TCG TT CAC TCA TGG-3' CRE-REV 5'-CAG GCT AAG TGC CTT CTC TAC ACC-3'
Lyve1-Cre	WT-FOR 5'-TGC CAC CTG AAG TCT CTC CT-3' CRE-FOR 5'-TGA GCC ACA GAA GGG TTA GG-3' WT-REV 5'-GAG GAT GGG GAC TGA AAC TG-3'

Sample acquisition

Plug check mating and embryo dissection

Vaginal plug checking was used to determine mating and the day of plug detection is counted as embryonic day 0.5 (E0.5). Embryos with appropriate age were dissected (in ice-cold PBS) free of the uterine muscle and membranes, whereas embryonic limbs were used for genotype analysis.

Sacrificing mice and tissue collection

Either combined carbon dioxide anesthesia and cervical dislocation or perfusion after ketamine (180 mg/kg) -xylazine (16 mg/kg) injection was performed to sacrifice animals.

Human myocardial biopsies

Human myocardial tissue samples were obtained from left ventricular biopsies of transplanted hearts. Immediately after tissue procurement, cardiac biopsies were shock frozen in liquid nitrogen, stored at - 80°C and processed for immunohistochemistry. Patients delivered a prospective written informed consent for research use of cardiac tissues to comply with the requirements of the Medical Council in Hesse, Germany, and the institutional ethics guidelines of the Kerckhoff-Klinik, Bad Nauheim, Germany. The responsible person at the clinic is Dr. Manfred Richter.

MRI and ECG

Cardiac magnetic resonance imaging (MRI)

Mice are anesthetized with 2.5% isoflurane, thereafter anesthesia is maintained with 1.5-2.0% (v / v) isoflurane in 0.5 l / min air and 0.5 l / min oxygen. Mice were kept on a warming plate during the MRI measurements, which were performed with a horizontal 7.05 T Bruker PharmaScan. MRI data were analyzed with Medis Suite MR V3.0 digital software (Medical Imaging Systems bv, Netherlands), including the corresponding QMass app. Here, multiple contiguous short-axis slices (slice thickness 1.0mm or 0.5mm) were acquired for complete coverage. Representative images show four-chamber views of the hearts. MRI was performed by Dr. Astrid Wietelmann, Scientific Service Group for MRI and µCT of the MPI-Bad Nauheim.

Electrocardiogram (ECG)

Non-invasive electrocardiography was performed using external electrodes under anesthesia as published by our laboratory [223]. For this purpose, mice were anesthetized with 2.0-2.5% isoflurane/oxygen for a maximum of 10 minutes and positioned with all 4 limbs on a footplate electrode. Heart rate and ECGs were recorded with the Rodent Surgical Monitor (Indus Instruments, USA).

Cell culture experiments

Murine embryonic stem cells

V6.5 mouse embryonic stem cells (ESC) were maintained on mouse embryonic fibroblast feeder layer at 37°C, 5% CO2 with daily media exchange. Media contained DMEM (Catalog No. 42430-025, Gibco) supplemented with 10% PSG, 15% FBS (Catalog No. S 0115, BioChrome), 0.1% 2-Mercaptoethanol (Catalog No. 97622, Sigma Aldrich), 1% MEM NEAA (Catalog No. 11140-035, Gibco) and 1000 U ESGRO Mouse LIF Medium Supplement (Catalog No. ESG1107, Merck). Slides were coated with 0.1% Gelatin when seeded for IF staining.

Isolation and cultivation of juvenile and adult cardiomyocytes

Cardiomyocytes were isolated from murine hearts by enzymatic digestion using a Langendorf system as previously described by O'Connell et al. [224]. In brief, dissected hearts were cannulated via the aorta and arrested by retrograde perfusion with calcium-free buffer (113mM NaCl, 4.7mM KCl, 0.6mM KH_2PO_4, 0.6mM Na_2HPO_4, 1.2mM $MgSO_4x7H_2O$, 12mM $NaHCO_3$, 10mM $KHCO_3$, 10mM HEPES, 30mM Taurin, 10mM 2,3-Butanedionemonoxime, 5.5mM glucose). Cannulated hearts were enzymatically digested by

perfusion with enzyme buffer solution (0.25mg/ml Liberase DH (Roche Diagnostics Corp.), 0.14mg/ml Trypsin, 12.5µM $CaCl_2$, dissolved in calcium-free buffer) and cut off from the cannula. Atria were separated, and ventricles were cut into small pieces in stop buffer (10% FCS; 12.5µM $CaCl_2$ in enzyme buffer). After gentle pipetting, myocytes were centrifuged at 500 rpm for 1 min. The supernatant was discarded and cell pellet, containing the cardiomyocyte fraction, was re-suspended in stop buffer 2 (5% FCS, 12.5µM $CaCl_2$ in enzyme buffer) and filtered through 500µm cell strainers.

For culturing cardiomyocytes, the calcium content of the cell suspension was adjusted stepwise to 1 mM and cardiomyocyte-containing cell pellets were re-suspended in supplemented M199 cell culture medium (Catalog No. 11310882, Gibco). Supplements include 5 mM creatinine x H_2O; 2mM L-carnitine x HCl; 5mM taurine; 25mM HEPES (Catalog No. 15630080, Gibco); 1% penicillin/streptavidin; 10% FCS; 1% insulin-transferrin-sodium selenite media supplement, adjusted to pH 7.3). Isolated cardiomyocytes were cultured at 37°C with 5% CO_2. Chemicals were purchased from Sigma Aldrich unless otherwise stated. Cardiomyocyte isolation was performed by Marion Wiesnet (MPI-HLR, Bad Nauheim, Germany).

ESC-derived cardiac bodies

Murine ES cell line CM7/1 was differentiated into cardiac bodies as previously described [147] in combination with the 3D Cell Culture Bioreactor CERO 3D (OMNI Life Science GmbH & Co KG). Cardiac bodies were harvested after 14 days of differentiation.

HL-1 cells

HL-1 cells (Catalog No. SCC065) were cultured on gelatin (0.02% w/v, Catalog No. G9391)/fibronectin (10 µg/ml, Catalog No. F1141) -coated plates and maintained in Claycomb medium (Catalog No. 51800C-500ML) supplemented with 10% HL-1 cell screened FBS (Catalog No. TMS-016-B), 100 µg/ml PSG (Catalog No. G6784), 0.1 mM Norepinephrine (Catalog No. A0937) and 2 mM L-Glutamine (Catalog No. G7513). The medium was changed every 24-48h. HL-1 cells were grown at 37°C in an atmosphere of 5% CO_2 and 95% air. Once the cells reached confluence, they were split 1:2 or 1:3 [as recommended by the manufacturer using Trypsin-EDTA (Catalog No. T3924) and Trypsin Inhibitor (Catalog No. T6522)], which is designated as a passage. Cells were used for a maximum of 15 passages. All components for HL-1 culturing were purchased from Sigma Aldrich/Merck.

HEK293T cells

Cells were cultured in high glucose DMEM (Catalog No. D5671-500ML, Sigma Aldrich) containing 10% FBS (Catalog No. F2442, Sigma Aldrich) and 1% PSG (Catalog No.

G6784-100ML, Sigma Aldrich) at 37°C and 10% CO_2. Cells were used for a maximum of 20 passages.

HUVECs and HDLECs

Human umbilical vein endothelial cells (HUVECs from pooled donors; Catalog No. C2519A, Lonza) were cultured at 37°C and 5% CO2 in EBM Endothelial Cell Growth Basal Medium (Catalog No. CC-3121, Lonza) containing SingleQuots supplements (Catalog No. CC-4133, Lonza).

Primary Human Dermal Lymphatic Endothelial Cells (HDLECs from a single donor; Catalog No. CC-2543, Lonza) were cultured at 37°C and 5% CO2 in EGMTM-2 BulletKit Medium (Catalog No. CC-3162, Lonza). Cells were used for a maximum of six passages.

RNA interference (RNAi) in cell culture

siRNA-mediated knockdown was performed using Lipofectamine RNAiMAX Transfection Reagent (Catalog No. 13778150, Thermo Fisher Scientific) as recommended by the manufacturer. ON-TARGETplus siRNA (SMARTPool) were purchased from Dharmacon (Horizon). Transfection was performed within the first hour post cell spitting. Cells were fixed at indicated time points, but no later than 72 hours post-transfection.

Table 4 siRNA pools used in this study

siRNA	Catalog No.	Lot
human Matr3-siRNA	L-017382-00-0005	190813
human Control-siRNA	D-001810-10-05	2626313

Plasmid transfection

Lipofectamine2000 reagent (Catalog No. 11668019, Thermo Fisher Scientific) was used for transient plasmid DNA transfection according to the manufacturer's protocol. Notably, transfection was performed within the first hour post cell spitting. The medium was substituted approximately 24 hours post-transfection. 48 hours post-transfection the cells were used for down-stream analysis because the expression of plasmids had reached a maximum.

<u>RNA-based methods</u>

RNA extraction for qRT-PCR and RNA-Seq

RNA was isolated from cells or tissue using the Direct-zol RNA Miniprep Kit (Catalog No. E2052, Zymo Research) according to the manufacturer's instructions. RNA was diluted in RNase-free TE (Catalog No. AM9849, Thermo Fisher Scientific) and stored at -80°C.

cDNA synthesis and qRT-PCR

Complementary DNA (cDNA) was reverse transcribed from 1µg of total RNA using SuperScriptTM II RT (Catalog No. 18064014, Thermo Fisher Scientific) or PrimeScript™ RT reagent Kit with gDNA Eraser (Catalog No. RR047A, Takara Bio Inc.). qPCR was performed with TaqMan Gene Expression Master Mix and TaqMan probes (TaqMan Gene Expression Assays) purchased from Applied Biosystems. qPCR reactions were processed on a StepOnePlus real-time PCR instrument (Applied Biosystems) and data were calculated using the $\Delta\Delta C_t$ method. Each sample set was performed in technical triplicates and normalized to G*apdh* or *ACTB* as internal housekeeping gene controls. The master mix for one 10µl qRT-PCR reaction was prepared as followed:

TaqMan™ Gene expression master mix	5.0 µL
TaqMan™ gene specific probe (FAM-dye)	0.5 µL
TaqMan™ housekeeping gene probe (VIC-dye)	0.5 µL
cDNA (diluted 1:100 in ddH$_2$O)	4.0 µL

Table 5 TaqMan Gene Expression Assays

Gene Name	Assay ID	Species
Acta1	Mm00808218_g1	mouse
ACTB (housekeeping gene)	Hs99999903_m1	human
Adar1	Mm00508001_m1	mouse
Adar2=Adarb1	Mm00504621_m1	mouse
Ctgf	Mm01192933_g1	mouse
Col1a1	Mm00801666_g1	mouse
Col4a1	Mm01210125_m1	mouse
Cyr61	Mm01323719_g1	mouse
Gapdh (housekeeping gene)	Mm99999915_g1	mouse
Matr3	Mm00726619_s1	mouse
MATR3	Hs01004687_g1	human
Myh6	Mm00440359_m1	mouse
Myh7	Mm00600555_m1	mouse
Nppa	Mm01255748_g1	mouse
Nppb	Mm01255770_g1	mouse
Rbm20	Mm01265001_m1	mouse
Yap	Mm01143263_m1	mouse

Whole transcriptome sequencing

RNA and library preparation integrity was verified with a BioAnalyzer 2100 (Agilent) or LabChip Gx Touch 24 (Perkin Elmer). 0,8 - 1µg of total RNA was used as input for SMARTer Stranded Total RNA Sample Prep Kit - HI Mammalian (Clontech). Raw reads were assessed for quality, adapter content, and duplication rates with FastQC 0.11.8 [225]. Trimmomatic version 0.39 was employed to trim reads after a quality drop below a mean of Q15 in a window of 5 nucleotides [226]. Only reads of at least 15 nucleotides were cleared for subsequent analyses. Trimmed and filtered reads were aligned versus mouse genome version mm10 (GRCm38) using STAR 2.6.1d with the parameters "--outFilterMismatchNoverLmax 0.1 - - outFilterScoreMinOverLread 0.9 --outFilterMatchNminOverLread 0.9 --alignIntronMax 200000" [227].

The number of reads aligning to genes was counted with featureCounts 1.6.4 from the Subread package [228]. Only reads mapping at least partially inside exons were admitted and aggregated per gene. Reads overlapping multiple genes or aligning to multiple regions were excluded. Differentially expressed genes were identified using DESeq2 version 1.18.1 [229]. Genes were classified to be significantly differentially expressed (DEG) with Benjamini-Hochberg corrected P-Value < 0.05 and $-0.59 \leq$ Log2FC $\geq +0.59$. The annotation was enriched with UniProt data (UniProt release 25.06.2019; [230]) based on Ensembl gene identifiers [231]. RNA sequencing and related bioinformatic analysis was performed by Dr. Stefan Günther (MPI-HLR, Bad Nauheim, Germany).

Gene ontology terms for *Mus musculus* were identified using Gene Ontology Consortium data, selected for GO *biological process complete*, with Fisher's exact test type and Bonferroni correction for multiple testing. Top 10 results for Bonferroni-corrected for P < 0.05 are displayed [232], [233].

MAJIQ and Voila

Alternative splicing events in Rbm20, Matr3 and double knockout mutant mice were analyzed with MAJIQ version 2 using the GENCODE annotation version 25 [19]. The majiq build step creates a splicegraph comprising known and novel local splicing variations (LSVs) and was executed with default parameters except for –minreads=20, --min-denovo=30 and --min-intronic-cov=0.1. The majiq deltapsi step quantifies changes in relative LSV abundance between conditions as change in percent selected index (∆PSI) values and was executed with default parameters except for –minreads=25 and --prior-minreads=50. The final voila tsv step enables the calculation of confidence measures reflecting the probability that a ∆PSI

value exceeded a user-defined threshold and was executed with default parameters except for –threshold=0.05 and --non-changing-treshold=0.02.

The resulting tsv files were processed in R version 4.0.2 [234], filtering for LSVs with at least one junction with ∆PSI > 5% and confidence > 90%, keeping only those junctions exceeding the thresholds. LSVs without junctions were filtered out. If LSVs were left with only one junction, the removed junction with the highest ∆PSI was added again. Finally, LSVs with two remaining junctions were classified as intron retention, exon skipping, alternative promoter, alternative polyadenylation and alternative splicing site based on overlaps with GENCODE exon annotations. LSVs with more than two junctions were classified as complex. Data was visualized with VOILA [19]. The bioinformatic analysis was performed by Dominik Stroh and Dr. Kathi Zarnack (BMLS, Frankfurt, Germany). Parts of the bioinfomatic analysis are published in Dominik Strohs Bachelor thesis entitled "Bioinformatische Analyse der Funktion der RNA-bindenden Proteine RBM20 und MATR3 in der RNA-Regulation im Herzgewebe der Maus" Goethe-Universität Frankfurt am Main, October 2020.

HyperTRIBE

Cloning of HyperTRIBE fusions: TRIBE plasmid pMT-Hrp48-ADARcd-V5-His (Addgene, plasmid no. 81172) was kindly provided by Weijin Xu and Michael Rosbach (Brandeis University in Waltham, US). Mutagenesis PCR created the E488Q hyperactive mutation (dmADAR*) from the original plasmid, using the following primer pair:

5'-CACTGGAATCGTCCCCTGACCGGACTCGATTTTGGTGCG-3'

5'-CGCACCAAAATCGAGTCCGGTCAGGGGACGATTCCAGTG-3'

For the final expression vectors, dmADAR* was fused to C-terminal part of full-length sequence of Matr3 or the Matr3∆RRM control variant, which encodes a depletion of the two RNA recognition motifs. Pure dmADAR* without fusion served as an additional control. A linker sequence (AAATAVD in amino acids, GCGGCCGCCACCGCGGTGGAC in DNA sequencing) was used between the sequence of the RBP of interest and dmADAR*. HyperTRIBE fusions carry a V5-His double-tag. In HL-1 cells, final HyperTRIBE fusions are overexpressed using the pCAG-GS expression vector. HyperTRIBE mouse strains were generated by transgene insertion into the ROSA26 locus.

Processing and sequencing of HyperTRIBE samples: HL-1 cells were transfected with generated HyperTRIBE plasmids using Lipofectamine2000 reagent (Catalog No. 11668019, Thermo Fisher Scientific) and harvested 48h post-transfection for downstream analysis such as immunofluorescent staining, Western blotting, or RNA-seq. For RNA-seq, total RNA from HL-1 cells or E14.5 embryonic hearts was isolated using the Direct-zol RNA Miniprep Kit von Zymo (Catalog no. R2053) as described above. Since Presumably binds to both intronic and

exonic regions, whole transcriptome sequencing (WT) with ribosomal RNA depletion was applied for target identification. Paired-end RNA sequencing was performed to filter out sequencing errors and to optimize the identification of adenosine-to-inosine (A-to-I) RNA editing events. In average 40 mio reads were obtained per sample. RNA sequencing of HyperTRIBE samples was performed by Dr. Stefan Günther (MPI-HLR, Bad Nauheim, Germany) as previously described.

JACUSA-based, bioinformatic data analysis of HyperTRIBE: HyperTRIBE data were processed with the online available JACUSA v1.3.5 workflow [235]. In brief, JACUSA pipeline enables to identify site-specific editing events as RNA-RNA-differences by comparison of transcriptome data from control and condition of interest. Notably, JACUSA does not filter for potential single-nucleotide polymorphisms and background editing. To exclude background editing, two different control constructs were used and taken as reference in JACUSA. JACUSA-based analysis of HyperTRIBE was processed by Prof. Dr. Christoph Dieterich (Klaus Tschira Institute for Integrative Computational Cardiology Department of Internal Medicine III, University Hospital Heidelberg, Germany).

HyperTRIBE downstream data analysis: Bioinformatic analysis provided lists of editing sites within potential target transcripts of MATR3. downstream analysis is based on this information and was performed with Excel 2015. Venny v2.1.0 [236] was used to visualize the overlap among the lists of edited transcripts. Bar diagrams were generated with GraphPad Prism 9.2.0. Gene ontology terms for *Mus musculus* were identified using Gene Ontology Consortium data, selected for GO *biological process complete*, with Fisher's exact test type and Bonferroni correction for multiple testing. Top 10 results for Bonferroni-corrected for $P < 0.05$ are displayed [232], [233].

Protein-based methods

Protein extraction and immunoblot

Cells or tissue samples were lysed with lysis buffer containing protease inhibitors and homogenized by sonication (Sonificator Bandelin Sonoplus HD2070). Protein concentration was determined using Bradford (DC™ Protein Assay from Bio-Rad). Total cell or tissue extracts in Novex™ NuPAGE™ LDS- sample puffer (Catalog No. NP0007, Thermo Fisher Scientific) was loaded on NuPAGE 7% Tris-Acetate gels (Catalog No. EA0355Box, Invitrogen) and subjected to gel electrophoresis in XCell SureLock™ Mini-Cells (Invitrogen). Here, prestained Protein Marker VI (Catalog No. A8889, BC PanReac AppliChem) or BioReagents™ EZ-Run™ Prestained Rec (Catalog No. 10638393, Thermo Fisher Scientific) was loaded as protein ladder.

Table 6 Antibodies used for Western blotting

Name	Species	Catalog No	Company	Dilution
anti-GAPDH	rabbit	2118	Cell Signaling Technology	1:2000
anti-GFP	rabbit	custom-made	Kindly provided by Dr. Andre Schneider	1:1000
anti-MATR3	rabbit	12202-2-AP	Proteintech	1:1000
anti-mouse IgG, HRP	goat	31430/ 1858413	Thermo Fisher Scientitic	1:2000
anti-rabbit IgG, HRP	goat	31460	Thermo Fisher Scientitic	1:2000
anti-RalA	mouse	610221	BD Transduction Laboratories	1:1000
anti-RBM20	rabbit	custom-made	Kindly provided by Prof. Dr. Michael Gotthardt (MDC, Berlin, Germany)	1:1000
anti-V5	rabbit	ab9116	Abcam	1:1000
anti-YAP	rabbit	PA1-46189	Thermo Fisher Scientitic	1:1000

Table 7 Buffers and solutions for Western blotting

Buffers and Solutions	Components
RIPA lysis buffer	pH 8.0 50mmol L-1 Tris, pH 7,4; 150mmol L-1 NaCl; 1% NP40; 0.5% sodium deoxycholate; 0.1% SDS; protease inhibitor cocktail
Protease inhibitor mix	2mg mL-1 aprotinin, 2mg mL-1 leupeptin, 1mol L-1 Na3VO4, 1mol L-1 NaF, 0.2mol L-1 PSMF
10 x TBS	0.2mol L-1 Tris, 1.4M NaCl, pH 7.6
1 x TBST	100mL 10 x TBS + 900mL Aqua dest. + 0.1 % Tween®20
20 x Transfer buffer	163.2g Bicine; 209.6 g Bis-Tris; 12g EDTA in 1000 mL Aqua dest.
1 x Transfer buffer	250mL 20 x transfer buffer; 1000mL methanol; 3750mL Aqua dest.

Gels were run in NuPAGE MOPS SDS Running Buffer (Catalog. No 11589156, Invitrogen) to obtain protein separation with protein sizes ranging from > 200 to 20 kDa. Next, proteins were transferred to Amersham™ Protran® Western blotting nitrocellulose membranes (Catalog No. GE10600002, GE Healthcare Life Science) using blot modules for the XCell SureLock™ Mini-Cells (Invitrogen). Red Alert staining (Catalog No. 71078, Merck) was used to verify successful protein transfer. Next, membranes were blocked in 5% BSA (Catalog No. BP 1605, Fisher Scientific) dissolved in TBST. and probed with specific antibodies overnight at 4°C, followed by incubation with peroxidase-conjugated (HRP) secondary antibodies for at least one hour at RT. The bands were visualized by chemiluminescence using an ECL

detection kit (Clarity Western ECL Substrate, Bio-Rad) and a ChemiDoc MP Imaging System (Bio-Rad). Quantification of band intensities by densitometry (RalA or GAPDH loading control as reference) was carried out using the Image Lab software (Bio-Rad) or ImageJ/Fiji (NIH).

Titin gels

Titin gels were processed as previously described [237]. Gels were stained with Coomassie and isoforms were quantified using the Aida Image Analyzer software. Data were further analyzed and visualized using GraphPad Prism 9.2.0. One-way ANOVA (ANalysis of VAriance) with post-hoc Tukey HSD (Honestly Significant Difference) test has been conducted to check for significance. Titin gels and quantifications were carried out in collaboration with Dr. Michael Radke and Prof. Dr. Michael Gotthardt (Max Delbrück Center for Molecular Medicine in the Helmholtz Association, Berlin, Germany).

Imaging-based techniques

Cryopreserved tissue sections

Tissues or embryos were dissected and fixed in 4%PFA/PBS overnight at 4°C and thereafter transferred to 30% sucrose (Catalog No. 9097.1, Carl Roth) in 1x PBS, again incubating overnight at 4°C. Samples were transferred into FSC22®Clear (Leica Biosystems), frozen on dry ice, and stored at -80°C. 10µm thick sections were cut with a Leica CM1950 cryostat and slides with cryosections were stored at -20°C.

Immunofluorescence staining of cells and (human or murine) cryosections

Table 8 Primary and secondary antibodies used for immunofluorescent stainings

Name	Species	Catalog No	Company	Dilution
anti-mouse MATR3	mouse	MABN1587	Millipore	1:200
anti-MATR3	rabbit	12202-2-AP	Proteintech	1:500
anti-α-Actinin (Sarcomeric) antibody, ACTN2	mouse	A7811-.2ML	Sigma Aldrich	1:500
anti-V5	rabbit	ab9116	Abcam	1:200
anti-YAP/TAZ (D24E4)	rabbit	8418	Cell Signaling Technology	1:200
F-Actin (anti-Phalloidin-TRITC)	-	P1951	Sigma Aldrich	1:500
DAPI	-	D1306	Thermo Fisher Scientific	1:1000
anti-rabbit Alexa 488	goat	A11070	Invitrogen	1:1000
anti-mouse Alexa 594	goat	A-11032	Invitrogen	1:1000

For IF, cells were seeded and processed on Nunc Lab-Tek Chamber slides (Catalog No. 177429, Thermo Fisher Scientific). Cells or cryosections were fixed for 15 min with 4% PFA/PBS. After three times washing, samples (cells or prefixed tissue sections) were permeabilized with 0,05% TritonX-100/PBS for 15 min. Three times washing was applied before blocking the samples for at least 15 min with 0.1% BSA/PBS (Catalog No. A7284-500ML, Sigma Aldrich). Primary antibodies were dissolved in incubation buffer (0.05% BSA/0.005% TritonX-100/PBS) and incubated with samples overnight at 4°C. The next day, samples were washed three times with PBS, followed by incubation with the corresponding secondary antibodies dissolved in PBS. DAPI staining was performed for 10 min. After final washing, samples were mounted in Mowiol 4-88 (Catalog No. 81381, Sigma Aldrich) covered with glass slides (Catalog No. LH26.1, Carl Roth).

Hematoxylin and Eosin staining or Sirius Red/Fast Green Collagen staining

Frozen sections were rinsed in ddH_2O and stained in Mayer's Hematoxylin (Haemalaun, Catalog No. 2E-038, Chroma Technology Corporation) for 10 min and then rinsed in warm running tap water until sections turned into blue. After rinsing in ddH_2O again, sections were stained in Eosin (Catalog No. 2C-140, Chroma Technology Corporation) for 6 min. Sections were dehydrated in an ascending alcohol series: 95% for 10 sec, 100% for 10 sec, and 100% for 2 min. Alternatively, cryosections were stained with the semi-quantitative total tissue collagen detection kit (Sirius Red/Fast Green collagen staining kit: Catalog No. 9046, Chondrex) as recommended by the manufacturer. Finally, sections were cleared in xylene for at least 10 min before they were mounted with Entellan (Catalog No. 1079600500, Merck). Histochemistry imaging was performed with HS all-in-one fluorescence microscope Biorevo Keyence BZ-9000E (Keyence). Images were processed with the corresponding BZ-II Analyzer.

Whole-mount embryonic dorsal skin

Staining of whole-mount embryonic dorsal skin was performed as previously described [140]. In brief, dorsal skin tissue was dissected from E15.5 mouse embryos and extra layers of muscle were removed. Samples were fixed in 4% PFA/PBS for 20 min followed by incubation in blocking buffer (3% BSA in PBS containing 0.2 % TritonX-100 and 0.25% Tween20) for at least one hour at RT. Washing steps between fixation and blocking were performed with PBST (0.1% Tween-20). Samples were incubated shaking in 1:1 (v:v) blocking buffer in PBS containing primary antibodies overnight at 4°C. For immunofluorescence detection, corresponding secondary were incubated for at least 2 h at room temperature. Whole-mount samples were mounted on glass slides with ProLong™ Gold Antifade Mountant (Catalog No. P36930, Thermo Fisher Scientific). Appropriate coverslips (Menzel 18x18mm, #1.5, Thermo

Fisher Scientific) for confocal microscopy were used. The cervicothoracic dorsal skin region was selected for imaging of (tiled) z-stack (10✕) images.

Whole-mount juvenile ear skin

Table 9 Primary and secondary antibodies for IF whole mount staining of embryonic dorsal back skin and juvenile/adult ear skin

Name	Species	Catalog No.	Company	Dilution
anti-CD31	rat	550274	BD Pharmingen	1:200
Anti-GFP-Alexa-488	rabbit	A21311	Invitrogen	1:200
anti-Goat IgG (H+L) AF555	donkey	A32816	Invitrogen	1:200
anti-Goat IgG (H+L) AF647	donkey	A21447	Invitrogen	1:200
anti-Ki67	rabbit	ab15580	Abcam	1:200
anti-LYVE1	rabbit	ab14917	Abcam	1:500
anti-MATR3	rabbit	12202-2-AP	Proteintech	1:1000
anti-NG2	rabbit	AB5320	Merck	1:200
anti-NRP2	goat	AF567	R&D Systems	1:200
anti-PROX1	goat	AF2727	R&D Systems	1:200
anti-PROX1	rabbit	11-002P	AngioBio Co.	1:200
anti-rabbit Alexa 488	goat	A11070	Invitrogen	1:200
anti-Rabbit IgG AF647	donkey	A31573	Invitrogen	1:200
anti-Rat IgG AF488	donkey	A21208	Invitrogen	1:200
anti-Rat IgG AF647	chicken	A21472	Invitrogen	1:200
anti-α-smooth muscle actin-Cy3	mouse	C6198	Sigma Aldrich	1:200

Whole-mount ear skin was processed based on the protocol of Yamazaki *et al.* [238]. In brief, ear skin from juvenile or adult mice was dissected, fixed in 4% PFA/PBS for 1 hour at RT, and washed three times in PBST (0.2% TritonX-100 in PBS). Connective tissues, fat, and hair were removed before staining. The samples were incubated in blocking buffer (0.2% TritonX-100 and 10% FCS in PBS) with diluted primary antibodies overnight at 4 °C. Afterward, samples were washed three times for 10 min with PBST at RT, followed by the incubation with secondary antibodies in blocking buffer. After three washing steps, samples were mounted on slides in mounting media (ProLong™ Gold Antifade Mountant, Catalog No.

P36930, Thermo Fisher Scientific). Here, the inner surface of the ear skin was in contact with the coverslip.

Transmission electron microscopy

Animals under anesthesia were perfused with 1.5% glutaraldehyde (Catalog No. G6257, Sigma Aldrich) and 1.5% formaldehyde (Catalog No. 252549, Sigma Aldrich) in 0.15M HEPES (Catalog No. 9105.03, Roth). Hearts were removed and stored in the same fixative at 4°C for at least 24h. Samples were washed with 0.05M HEPES and post-fixed in 1% osmium tetroxide (Catalog No. E19190, Science Services) in aqua bidest. After washing with water, heart samples were kept in 0.1% Tannin (Catalog No. 2726.1, Roth)/0.05M HEPES for 30 minutes, followed by twice 10 min washing with 1% Na_2SO_4 (Catalog No. 4403.1, Roth) in 0.05M HEPES. Samples were half-saturated in 2% watery uranyl acetate (Catalog No. 77870.01, Serva) for 1h and dehydrated in an ascending ethanol series, calibrated in 1:1 Propylenoxid:Epon (Catalog No. 33715.03, Serva) and finally embedded in Epon. Polymerization occurred at 60°C within 48h. Ultrathin sections were cut using an ultramicrotome (Leica EM Rapid) and examined by TEM (JEOL JEM-1400 Plus). Sample preparation and ultrastructural imaging were performed by Janett Piesker, Scientific Service Group Microscopy of the MPI-Bad Nauheim.

Image acquisition and processing

Confocal microscopy was carried out on a Leica TCS SP8 Confocal or a Leica TCS SP8 Multiphoton (MP). Scanning speed, excitation, and amplification settings were kept constant during each experiment. Sequential scans were stacked and are shown as maximum projection. ImageJ/Fiji software was used for processing, measurements, and quantifications.

Blinding, statistical analysis and visualization

The following experiments were quantified blinded: cardiac MRI, cardiomyocyte size measurements, quantifications of blood and lymph vessel formation.

Number of samples of the certain genotypes is indicated as "n" in figure legends. All data are presented as mean ± SD (standard deviation). In addition, individual data points are scattered. Unless otherwise stated, statistical significance between groups was assessed using a two-tailed Student's t-test (2 groups) or ANOVA analysis (> 2 groups). $P < 0.05$ was considered to be significant. Asterisks show statistical significance: * $P < 0.05$; **$P < 0.01$; ***$P < 0.001$; ****$P < 0.0001$. ns = not significant.

The survival of mice was estimated by the Kaplan-Meier method and survival curves were compared with the Gehan-Breslow-Wilcoxon test. All calculations and bar diagrams were done using GraphPad Prism 9.2.0. Venn diagrams were generated using Venny v2.1.0 [236]

to examine the overlap among conditions. The Integrative Genomics Viewer (IGV) 2.3.91 [239] was used for the visual exploration of sequencing data and WIlsON R package was used for plotting feature-based sequencing data [240]. Illustrations for HT proteins (**Figure 49**, page 59) were drawn by using pictures from Servier Medical Art by Servier [241].

List of commonly used chemicals and machines

Table 10 Commonly used chemicals and machines

Chemical and items	Catalog No	Company
Agarose	2267	Carl Roth
Bicine	B3876	Sigma Aldrich
Bis-Tris	A1025,0500	AppliChem
EDTA (H2O free)	8040.1	Carl Roth
EDTA-Na2 + 2 H2O	8043.2	Carl Roth
Ethanol 100%	K928.3	Carl Roth
Ethanol denatured	9065.4	Carl Roth
HCl 37%	4625.1	Carl Roth
Isopropanol	6752.4	Carl Roth
Methanol	4627.5	Carl Roth
NaCl	3957.2	Carl Roth
NP40 (Nonidet P40 Substitute)	74385	Fluka Analytical
Paraformaldehyd	0335.4	Carl Roth
PCR strips	A1302-3700	Star Lab Group
Precision cover glasses (High Precision Cover Glasses 170+-5µm. No. 1.5H) 18 x 18 mm	0107032	Paul Marienfeld GmbH & Co. KG
Protein LoBind Tubes	0030108116	Eppendorf
Rnase-ZAP	R2020-250ml	Sigma Aldrich
SDS ultra pure	2326.3	Carl Roth
Sodium deoxycholate	30970	Sigma Aldrich
Superfrost Ultra Plus Microscope Slides	J3800AMNZ	Thermo Fisher Scientific
Tris	5429.2	Carl Roth
TritonX-100	6683.1	Carl Roth
Tween-20	9127.2	Carl Roth
Thermocyclers for PCR	C1000 Touch Thermal Cycler, T100 Thermal Cycler	BioRad
UV light chamber (Wavelength 312nm)	Transilluminator UST-30M-8R	BioView
Centrifuges	5430	Eppendorf

Abbreviations

µm	Micrometer		E	Embryonic day
ALS	Amyotrophic Lateral Sclerosis		ECG	Echocardiography
			ED mass	End systolic mass
A-to-I	Adenosine to inosine RNA editing		EDV	End diastolic volume
			EF	Ejection fraction
BEC	Blood endothelial cell		ESC	Embryonic stem cell
bp	Base pairs		ES mass	End diastolic mass
BSA	Bovine serum albumin		ESC	Embryonic stem cells
BW	Body weight		ESE	Exonic splicing enhancer
cDNA	Complementary DNA		ESS	Exonic splicing silencer
CHD	Coronary heart disease		ESV	End systolic volume
circRNA	Circular RNA		FBS	Fetal bovine serum
CLIP	Cross-linking and immunoprecipitation		FC	Fold change
			FCS	Fetal calf serum
CO	Cardiac output		FDR	False discovery rate
CO_2	Carbondioxide		fl/fl	Floxed allele
DAPI	4', 6-diamidino-2phenylindole		For	Forward (Primer)
DCM	Dilated cardiomyopathy		FVB	Friend leukemia virus B, inbred laboratory mouse strain
DCMi	Myocarditis, inflammatory cardiomyopathy			
			GOI	Gene of interest
ddH_2O	Double distilled water		GFP	Green fluorescent protein
DEG	Differentially expressed gene		GSEA	Gene set enrichment analysis
dKO	Double knockout			
DMEM	Dulbecco's Modified Eagle's Medium		h	Hour(s) or in respect to genes: human
DNA	Deoxyribonucleic acid			
			H&E	Hematoxylin & eosin

H2O	Water	LSV	Local splicing variation
HCM	Hypertrophic cardiomyopathy	LV	Left ventricle, left ventricular
HDLEC	Primary Human Dermal Lymphatic Endothelial Cells	LVEF	Left ventricular ejection fraction
HEK293T	Human embryonic kidney cells 293T	LVOT	Left ventricular outflow tract
hESC	Human embryonic stem cell	MDa	Mega dalton
hnRNP	Heterogeneous nuclear ribonucleoproteins	min	Minutes
		mg	Milligram
hiPSC	Human induced pluripotent stem cell	MRI	Magnetic resonance imaging
		mRNA	Messenger ribonucleic acid
HT	HyperTRIBE (method)	mRNPs	Ribonucleoprotein complexes
HUVEC	Primary Human Umbilical Vein Endothelial Cells	N2a	Neuro-2a, mouse neural crest-derived cell line
HW	Heart weight	n.d.	Not detected
iCLIP	Individual-nucleotide resolution CLIP	neg	Negative
		NES	Nuclear export signal
ICM	Ischemic cardiomyopathy	NLS	Nuclear localization signal
IF	Immunofluorescent / Immunoflourescence staining	NMD	Nonsense-mediated mRNA decay
		OE	overexpressing
IGV	Integrative Genomics Viewer	P	Postnatal day
ISE	Intronic splicing enhancer	PBS	Phosphate-buffered saline
ISS	Intronic splicing silencer	PBST	Phosphate buffered saline with Tween-20
JLS	Jugular lymph sacs		
kDA	Kilo Dalton	PCR	Polymerase chain reaction
KO	Knockout	PFA	Paraformaldehyde
L	Liter	pos	Positive
LEC	Lymphatic endothelial cell	PSG	L-Glutamine-penicillin-streptomycin solution

qRT_PCR	Quantitative polymerase chain reaction	SV	Stroke volume
RBP(s)	RNA-binding protein(s)	T	Thrombus
RNA	Ribonucleic acid	TA	Musculus tibialis anterior
RNA-seq	RNA sequencing	TBS	Tris-buffered saline
RNP	Ribonucleoprotein	TBST	Tris-buffered saline (TBS) with Tween-20
rpm	Revolutions per minute	TL	Tibial length
RRM	RNA recognition motif	TRIBE	Targets of RNA-binding proteins identified by Editing
RT	Room temperature		
Rev	Reverse (Primer)	v:v	Volume to volume
RV	Right ventricle	vSMC	Vascular smooth muscle cells
scRNA-seq	Single-cell RNA-sequencing		
		WT	Wild type
SD	Standard deviation	ZnF	Zinc finger
sKO	Single Knockout		
SRE	Splicing regulatory element		

References

[1] G. Dreyfuss, V. N. Kim, and N. Kataoka, "Messenger-RNA-binding proteins and the messages they carry," *Nat. Rev. Mol. Cell Biol.*, vol. 3, no. 3, pp. 195–205, Mar. 2002, doi: 10.1038/nrm760.

[2] C. Maris, C. Dominguez, and F. H.-T. Allain, "The RNA recognition motif, a plastic RNA-binding platform to regulate post-transcriptional gene expression," *FEBS J.*, vol. 272, no. 9, pp. 2118–2131, May 2005, doi: 10.1111/j.1742-4658.2005.04653.x.

[3] J. H. Laity, B. M. Lee, and P. E. Wright, "Zinc finger proteins: new insights into structural and functional diversity," *Curr. Opin. Struct. Biol.*, vol. 11, no. 1, pp. 39–46, Feb. 2001, doi: 10.1016/s0959-440x(00)00167-6.

[4] Z. Zhou, L. J. Licklider, S. P. Gygi, and R. Reed, "Comprehensive proteomic analysis of the human spliceosome," *Nature*, vol. 419, no. 6903, pp. 182–185, Sep. 2002, doi: 10.1038/nature01031.

[5] S. Valadkhan and Y. Jaladat, "The spliceosomal proteome: at the heart of the largest cellular ribonucleoprotein machine," *Proteomics*, vol. 10, no. 22, pp. 4128–4141, Nov. 2010, doi: 10.1002/pmic.201000354.

[6] A. A. Hoskins and M. J. Moore, "The spliceosome: a flexible, reversible macromolecular machine," *Trends Biochem. Sci.*, vol. 37, no. 5, pp. 179–188, May 2012, doi: 10.1016/j.tibs.2012.02.009.

[7] Y. Wang and Z. Wang, "Systematical identification of splicing regulatory cis-elements and cognate trans-factors," *Methods San Diego Calif*, vol. 65, no. 3, pp. 350–358, Feb. 2014, doi: 10.1016/j.ymeth.2013.08.019.

[8] C. Schindewolf, S. Braun, and H. Domdey, "In vitro generation of a circular exon from a linear pre-mRNA transcript," *Nucleic Acids Res.*, vol. 24, no. 7, pp. 1260–1266, Apr. 1996, doi: 10.1093/nar/24.7.1260.

[9] Y. Wang *et al.*, "Mechanism of alternative splicing and its regulation," *Biomed. Rep.*, vol. 3, no. 2, pp. 152–158, Mar. 2015, doi: 10.3892/br.2014.407.

[10] U. Kim, Y. Wang, T. Sanford, Y. Zeng, and K. Nishikura, "Molecular cloning of cDNA for double-stranded RNA adenosine deaminase, a candidate enzyme for nuclear RNA editing," *Proc. Natl. Acad. Sci. U. S. A.*, vol. 91, no. 24, pp. 11457–11461, Nov. 1994, doi: 10.1073/pnas.91.24.11457.

[11] S. M. Rueter, T. R. Dawson, and R. B. Emeson, "Regulation of alternative splicing by RNA editing," *Nature*, vol. 399, no. 6731, pp. 75–80, May 1999, doi: 10.1038/19992.

[12] J. M. Gott and R. B. Emeson, "Functions and mechanisms of RNA editing," *Annu. Rev. Genet.*, vol. 34, pp. 499–531, 2000, doi: 10.1146/annurev.genet.34.1.499.

[13] K. Nishikura, "Functions and regulation of RNA editing by ADAR deaminases," *Annu. Rev. Biochem.*, vol. 79, pp. 321–349, 2010, doi: 10.1146/annurev-biochem-060208-105251.

[14] T. W. Nilsen and B. R. Graveley, "Expansion of the eukaryotic proteome by alternative splicing," *Nature*, vol. 463, no. 7280, pp. 457–463, Jan. 2010, doi: 10.1038/nature08909.

[15] D. Pullirsch and M. F. Jantsch, "Proteome diversification by adenosine to inosine RNA editing," *RNA Biol.*, vol. 7, no. 2, pp. 205–212, Apr. 2010, doi: 10.4161/rna.7.2.11286.

[16] M. L. Gonzalez-Garay, "Introduction to Isoform Sequencing Using Pacific Biosciences Technology (Iso-Seq)," in *Transcriptomics and Gene Regulation*, J. Wu, Ed. Dordrecht: Springer Netherlands, 2016, pp. 141–160. doi: 10.1007/978-94-017-7450-5_6.

[17] S. Oikonomopoulos, A. Bayega, S. Fahiminiya, H. Djambazian, P. Berube, and J. Ragoussis, "Methodologies for Transcript Profiling Using Long-Read Technologies," *Front. Genet.*, vol. 11, 2020, [Online]. Available: https://www.frontiersin.org/article/10.3389/fgene.2020.00606

[18] S. Anders, A. Reyes, and W. Huber, "Detecting differential usage of exons from RNA-seq data," *Genome Res.*, vol. 22, no. 10, pp. 2008–2017, Oct. 2012, doi: 10.1101/gr.133744.111.

[19] J. Vaquero-Garcia *et al.*, "A new view of transcriptome complexity and regulation through the lens of local splicing variations," *eLife*, vol. 5, p. e11752, Feb. 2016, doi: 10.7554/eLife.11752.

[20] S. S. Norton, J. Vaquero-Garcia, N. F. Lahens, G. R. Grant, and Y. Barash, "Outlier detection for improved differential splicing quantification from RNA-Seq experiments with replicates," *Bioinforma. Oxf. Engl.*, vol. 34, no. 9, pp. 1488–1497, May 2018, doi: 10.1093/bioinformatics/btx790.

[21] J. Ule, K. B. Jensen, M. Ruggiu, A. Mele, A. Ule, and R. B. Darnell, "CLIP identifies Nova-regulated RNA networks in the brain," *Science*, vol. 302, no. 5648, pp. 1212–1215, Nov. 2003, doi: 10.1126/science.1090095.

[22] A. C. McMahon *et al.*, "TRIBE: Hijacking an RNA-Editing Enzyme to Identify Cell-Specific Targets of RNA-Binding Proteins," *Cell*, vol. 165, no. 3, pp. 742–753, Apr. 2016, doi: 10.1016/j.cell.2016.03.007.

[23] J. Biswas, R. Rahman, V. Gupta, M. Rosbash, and R. H. Singer, "MS2-TRIBE Evaluates Both Protein-RNA Interactions and Nuclear Organization of Transcription by RNA Editing," *iScience*, vol. 23, no. 7, p. 101318, Jul. 2020, doi: 10.1016/j.isci.2020.101318.

[24] H. Jin *et al.*, "TRIBE editing reveals specific mRNA targets of eIF4E-BP in Drosophila and in mammals," *Sci. Adv.*, vol. 6, no. 33, p. eabb8771, Aug. 2020, doi: 10.1126/sciadv.abb8771.

[25] W. Xu, R. Rahman, and M. Rosbash, "Mechanistic implications of enhanced editing by a HyperTRIBE RNA-binding protein," *RNA N. Y. N*, vol. 24, no. 2, pp. 173–182, Feb. 2018, doi: 10.1261/rna.064691.117.

[26] R. Rahman, W. Xu, H. Jin, and M. Rosbash, "Identification of RNA-binding protein targets with HyperTRIBE," *Nat. Protoc.*, vol. 13, no. 8, pp. 1829–1849, Aug. 2018, doi: 10.1038/s41596-018-0020-y.

[27] Y. Blech-Hermoni and A. N. Ladd, "RNA binding proteins in the regulation of heart development," *Int. J. Biochem. Cell Biol.*, vol. 45, no. 11, pp. 2467–2478, Nov. 2013, doi: 10.1016/j.biocel.2013.08.008.

[28] R. G. de Bruin, T. J. Rabelink, A. J. van Zonneveld, and E. P. van der Veer, "Emerging roles for RNA-binding proteins as effectors and regulators of cardiovascular disease," *Eur. Heart J.*, vol. 38, no. 18, pp. 1380–1388, May 2017, doi: 10.1093/eurheartj/ehw567.

[29] Y. Liao *et al.*, "The Cardiomyocyte RNA-Binding Proteome: Links to Intermediary Metabolism and Heart Disease," *Cell Rep.*, vol. 16, no. 5, pp. 1456–1469, Aug. 2016, doi: 10.1016/j.celrep.2016.06.084.

[30] A. N. Ladd, "New Insights Into the Role of RNA-Binding Proteins in the Regulation of Heart Development," in *International Review of Cell and Molecular Biology*, vol. 324, K. W. Jeon, Ed. Academic Press, 2016, pp. 125–185. doi: 10.1016/bs.ircmb.2015.12.009.

[31] C. Gao *et al.*, "RBFox1-mediated RNA splicing regulates cardiac hypertrophy and heart failure," *J. Clin. Invest.*, vol. 126, no. 1, pp. 195–206, Jan. 2016, doi: 10.1172/JCI84015.

[32] W. Guo *et al.*, "RBM20, a gene for hereditary cardiomyopathy, regulates titin splicing," *Nat. Med.*, vol. 18, no. 5, pp. 766–773, May 2012, doi: 10.1038/nm.2693.

[33] J. Yang *et al.*, "RBM24 is a major regulator of muscle-specific alternative splicing," *Dev. Cell*, vol. 31, no. 1, pp. 87–99, Oct. 2014, doi: 10.1016/j.devcel.2014.08.025.

[34] A. Di Matteo *et al.*, "Alternative splicing in endothelial cells: novel therapeutic opportunities in cancer angiogenesis," *J. Exp. Clin. Cancer Res.*, vol. 39, no. 1, p. 275, Dec. 2020, doi: 10.1186/s13046-020-01753-1.

[35] V. A. Cornelius, J. R. Fulton, and A. Margariti, "Alternative Splicing: A Key Mediator of Diabetic Vasculopathy," *Genes*, vol. 12, no. 9, p. 1332, Aug. 2021, doi: 10.3390/genes12091332.

[36] C. J. Robinson and S. E. Stringer, "The splice variants of vascular endothelial growth factor (VEGF) and their receptors," *J. Cell Sci.*, vol. 114, no. Pt 5, pp. 853–865, Mar. 2001.

[37] S.-H. Chang and T. Hla, "Gene regulation by RNA binding proteins and microRNAs in angiogenesis," *Trends Mol. Med.*, vol. 17, no. 11, pp. 650–658, Nov. 2011, doi: 10.1016/j.molmed.2011.06.008.

[38] S. E. Bell *et al.*, "The RNA binding protein Zfp36l1 is required for normal vascularisation and post-transcriptionally regulates VEGF expression," *Dev. Dyn. Off. Publ. Am. Assoc. Anat.*, vol. 235, no. 11, pp. 3144–3155, Nov. 2006, doi: 10.1002/dvdy.20949.

[39] S. Baek *et al.*, "The Alternative Splicing Regulator Nova2 Constrains Vascular Erk Signaling to Limit Specification of the Lymphatic Lineage," *Dev. Cell*, vol. 49, no. 2, pp. 279-292.e5, Apr. 2019, doi: 10.1016/j.devcel.2019.03.017.

[40] A. C. Gittenberger-De Groot, N. M. S. Van Den Akker, M. M. Bartelings, S. Webb, J. M. G. Van Vugt, and M. C. Haak, "Abnormal lymphatic development in trisomy 16 mouse embryos precedes nuchal edema," *Dev. Dyn. Off. Publ. Am. Assoc. Anat.*, vol. 230, no. 2, pp. 378–384, Jun. 2004, doi: 10.1002/dvdy.20054.

[41] D. Marino, V. Dabouras, A. W. Brändli, and M. Detmar, "A role for all-trans-retinoic acid in the early steps of lymphatic vasculature development," *J. Vasc. Res.*, vol. 48, no. 3, pp. 236–251, 2011, doi: 10.1159/000320620.

[42] I. Martinez-Corral *et al.*, "Nonvenous origin of dermal lymphatic vasculature," *Circ. Res.*, vol. 116, no. 10, pp. 1649–1654, May 2015, doi: 10.1161/CIRCRESAHA.116.306170.

[43] J. M. James, A. Nalbandian, and Y. Mukouyama, "TGFβ signaling is required for sprouting lymphangiogenesis during lymphatic network development in the skin," *Dev. Camb. Engl.*, vol. 140, no. 18, pp. 3903–3914, Sep. 2013, doi: 10.1242/dev.095026.

[44] J. T. Wigle and G. Oliver, "Prox1 function is required for the development of the murine lymphatic system," *Cell*, vol. 98, no. 6, pp. 769–778, Sep. 1999, doi: 10.1016/s0092-8674(00)81511-1.

[45] G. Oliver, B. Sosa-Pineda, S. Geisendorf, E. P. Spana, C. Q. Doe, and P. Gruss, "Prox 1, a prospero-related homeobox gene expressed during mouse development," *Mech. Dev.*, vol. 44, no. 1, pp. 3–16, Nov. 1993, doi: 10.1016/0925-4773(93)90012-m.

[46] S. Banerji *et al.*, "LYVE-1, a new homologue of the CD44 glycoprotein, is a lymph-specific receptor for hyaluronan," *J. Cell Biol.*, vol. 144, no. 4, pp. 789–801, Feb. 1999, doi: 10.1083/jcb.144.4.789.

[47] S. Breiteneder-Geleff *et al.*, "Angiosarcomas express mixed endothelial phenotypes of blood and lymphatic capillaries: podoplanin as a specific marker for lymphatic endothelium," *Am. J. Pathol.*, vol. 154, no. 2, pp. 385–394, Feb. 1999, doi: 10.1016/S0002-9440(10)65285-6.

[48] A. Kaipainen *et al.*, "Expression of the fms-like tyrosine kinase 4 gene becomes restricted to lymphatic endothelium during development," *Proc. Natl. Acad. Sci. U. S. A.*, vol. 92, no. 8, pp. 3566–3570, Apr. 1995, doi: 10.1073/pnas.92.8.3566.

[49] M. J. Karkkainen *et al.*, "A model for gene therapy of human hereditary lymphedema," *Proc. Natl. Acad. Sci. U. S. A.*, vol. 98, no. 22, pp. 12677–12682, Oct. 2001, doi: 10.1073/pnas.221449198.

[50] S. Podgrabinska, P. Braun, P. Velasco, B. Kloos, M. S. Pepper, and M. Skobe, "Molecular characterization of lymphatic endothelial cells," *Proc. Natl. Acad. Sci. U. S. A.*, vol. 99, no. 25, pp. 16069–16074, Dec. 2002, doi: 10.1073/pnas.242401399.

[51] E. Kriehuber *et al.*, "Isolation and characterization of dermal lymphatic and blood endothelial cells reveal stable and functionally specialized cell lineages," *J. Exp. Med.*, vol. 194, no. 6, pp. 797–808, Sep. 2001, doi: 10.1084/jem.194.6.797.

[52] M. Detmar and S. Hirakawa, "The formation of lymphatic vessels and its importance in the setting of malignancy," *J. Exp. Med.*, vol. 196, no. 6, pp. 713–718, Sep. 2002, doi: 10.1084/jem.20021346.

[53] R. H. Mellor *et al.,* "Mutations in FOXC2 in humans (lymphoedema distichiasis syndrome) cause lymphatic dysfunction on dependency," *J. Vasc. Res.,* vol. 48, no. 5, pp. 397–407, 2011, doi: 10.1159/000323484.

[54] V.-M. Leppänen *et al.,* "Characterization of ANGPT2 mutations associated with primary lymphedema," *Sci. Transl. Med.,* vol. 12, no. 560, p. eaax8013, Sep. 2020, doi: 10.1126/scitranslmed.aax8013.

[55] G. Brice *et al.,* "Milroy disease and the VEGFR-3 mutation phenotype," *J. Med. Genet.,* vol. 42, no. 2, pp. 98–102, Feb. 2005, doi: 10.1136/jmg.2004.024802.

[56] A. C. Nag, "Study of non-muscle cells of the adult mammalian heart: a fine structural analysis and distribution," *Cytobios,* vol. 28, no. 109, pp. 41–61, 1980.

[57] A. R. Pinto *et al.,* "Revisiting Cardiac Cellular Composition," *Circ. Res.,* vol. 118, no. 3, pp. 400–409, Feb. 2016, doi: 10.1161/CIRCRESAHA.115.307778.

[58] D. H. Moore and H. Ruska, "Electron microscope study of mammalian cardiac muscle cells," *J. Biophys. Biochem. Cytol.,* vol. 3, no. 2, pp. 261–268, Mar. 1957, doi: 10.1083/jcb.3.2.261.

[59] P. F. van der Ven and D. O. Fürst, "Assembly of titin, myomesin and M-protein into the sarcomeric M band in differentiating human skeletal muscle cells in vitro," *Cell Struct. Funct.,* vol. 22, no. 1, pp. 163–171, Feb. 1997, doi: 10.1247/csf.22.163.

[60] E. M. McNally and L. Mestroni, "Dilated Cardiomyopathy: Genetic Determinants and Mechanisms," *Circ. Res.,* vol. 121, no. 7, pp. 731–748, Sep. 2017, doi: 10.1161/CIRCRESAHA.116.309396.

[61] B.-A. Sela, "[Titin: some aspects of the largest protein in the body]," *Harefuah,* vol. 141, no. 7, pp. 631–5, 665, Jul. 2002.

[62] M. Pfuhl and A. Pastore, "Tertiary structure of an immunoglobulin-like domain from the giant muscle protein titin: a new member of the I set," *Struct. Lond. Engl. 1993,* vol. 3, no. 4, pp. 391–401, Apr. 1995, doi: 10.1016/s0969-2126(01)00170-8.

[63] D. O. Fürst, M. Osborn, R. Nave, and K. Weber, "The organization of titin filaments in the half-sarcomere revealed by monoclonal antibodies in immunoelectron microscopy: a map of ten nonrepetitive epitopes starting at the Z line extends close to the M line," *J. Cell Biol.,* vol. 106, no. 5, pp. 1563–1572, May 1988, doi: 10.1083/jcb.106.5.1563.

[64] H. Yajima *et al.,* "A 11.5-kb 5'-terminal cDNA sequence of chicken breast muscle connectin/titin reveals its Z line binding region," *Biochem. Biophys. Res. Commun.,* vol. 223, no. 1, pp. 160–164, Jun. 1996, doi: 10.1006/bbrc.1996.0862.

[65] C. C. Gregorio *et al.,* "The NH2 terminus of titin spans the Z-disc: its interaction with a novel 19-kD ligand (T-cap) is required for sarcomeric integrity," *J. Cell Biol.,* vol. 143, no. 4, pp. 1013–1027, Nov. 1998, doi: 10.1083/jcb.143.4.1013.

[66] W. M. Obermann, M. Gautel, F. Steiner, P. F. van der Ven, K. Weber, and D. O. Fürst, "The structure of the sarcomeric M band: localization of defined domains of myomesin, M-protein, and the 250-kD carboxy-terminal region of titin by immunoelectron microscopy," *J. Cell Biol.,* vol. 134, no. 6, pp. 1441–1453, Sep. 1996, doi: 10.1083/jcb.134.6.1441.

[67] H. L. Granzier and T. C. Irving, "Passive tension in cardiac muscle: contribution of collagen, titin, microtubules, and intermediate filaments," *Biophys. J.,* vol. 68, no. 3, pp. 1027–1044, Mar. 1995, doi: 10.1016/S0006-3495(95)80278-X.

[68] W. A. Linke *et al.,* "I-band titin in cardiac muscle is a three-element molecular spring and is critical for maintaining thin filament structure," *J. Cell Biol.,* vol. 146, no. 3, pp. 631–644, Aug. 1999, doi: 10.1083/jcb.146.3.631.

[69] A. Soteriou, M. Gamage, and J. Trinick, "A survey of interactions made by the giant protein titin," *J. Cell Sci.,* vol. 104 (Pt 1), pp. 119–123, Jan. 1993.

[70] T. Watanabe, A. Kimura, and H. Kuroyanagi, "Alternative Splicing Regulator RBM20 and Cardiomyopathy," *Front. Mol. Biosci.,* vol. 5, p. 105, 2018, doi: 10.3389/fmolb.2018.00105.

[71] W. Guo, S. J. Bharmal, K. Esbona, and M. L. Greaser, "Titin diversity--alternative splicing gone wild," *J. Biomed. Biotechnol.,* vol. 2010, p. 753675, 2010, doi: 10.1155/2010/753675.

[72] M. L. Bang *et al.*, "The complete gene sequence of titin, expression of an unusual approximately 700-kDa titin isoform, and its interaction with obscurin identify a novel Z-line to I-band linking system," *Circ. Res.*, vol. 89, no. 11, pp. 1065–1072, Nov. 2001, doi: 10.1161/hh2301.100981.

[73] M. Krüger, T. Kohl, and W. A. Linke, "Developmental changes in passive stiffness and myofilament Ca2+ sensitivity due to titin and troponin-I isoform switching are not critically triggered by birth," *Am. J. Physiol. Heart Circ. Physiol.*, vol. 291, no. 2, pp. H496-506, Aug. 2006, doi: 10.1152/ajpheart.00114.2006.

[74] C. A. Opitz, M. C. Leake, I. Makarenko, V. Benes, and W. A. Linke, "Developmentally regulated switching of titin size alters myofibrillar stiffness in the perinatal heart," *Circ. Res.*, vol. 94, no. 7, pp. 967–975, Apr. 2004, doi: 10.1161/01.RES.0000124301.48193.E1.

[75] C. Neagoe *et al.*, "Titin isoform switch in ischemic human heart disease," *Circulation*, vol. 106, no. 11, pp. 1333–1341, Sep. 2002, doi: 10.1161/01.cir.0000029803.93022.93.

[76] S. F. Nagueh *et al.*, "Altered titin expression, myocardial stiffness, and left ventricular function in patients with dilated cardiomyopathy," *Circulation*, vol. 110, no. 2, pp. 155–162, Jul. 2004, doi: 10.1161/01.CIR.0000135591.37759.AF.

[77] M. L. Greaser *et al.*, "Mutation that dramatically alters rat titin isoform expression and cardiomyocyte passive tension," *J. Mol. Cell. Cardiol.*, vol. 44, no. 6, pp. 983–991, Jun. 2008, doi: 10.1016/j.yjmcc.2008.02.272.

[78] B. J. Maron *et al.*, "Contemporary definitions and classification of the cardiomyopathies: an American Heart Association Scientific Statement from the Council on Clinical Cardiology, Heart Failure and Transplantation Committee; Quality of Care and Outcomes Research and Functional Genomics and Translational Biology Interdisciplinary Working Groups; and Council on Epidemiology and Prevention," *Circulation*, vol. 113, no. 14, pp. 1807–1816, Apr. 2006, doi: 10.1161/CIRCULATIONAHA.106.174287.

[79] A. A. Geisterfer-Lowrance *et al.*, "A molecular basis for familial hypertrophic cardiomyopathy: a beta cardiac myosin heavy chain gene missense mutation," *Cell*, vol. 62, no. 5, pp. 999–1006, Sep. 1990, doi: 10.1016/0092-8674(90)90274-i.

[80] H. Watkins *et al.*, "Mutations in the cardiac myosin binding protein-C gene on chromosome 11 cause familial hypertrophic cardiomyopathy," *Nat. Genet.*, vol. 11, no. 4, pp. 434–437, Dec. 1995, doi: 10.1038/ng1295-434.

[81] C. Holubarsch *et al.*, "Existence of the Frank-Starling mechanism in the failing human heart. Investigations on the organ, tissue, and sarcomere levels," *Circulation*, vol. 94, no. 4, pp. 683–689, Aug. 1996, doi: 10.1161/01.cir.94.4.683.

[82] V. Saks, P. Dzeja, U. Schlattner, M. Vendelin, A. Terzic, and T. Wallimann, "Cardiac system bioenergetics: metabolic basis of the Frank-Starling law," *J. Physiol.*, vol. 571, no. Pt 2, pp. 253–273, Mar. 2006, doi: 10.1113/jphysiol.2005.101444.

[83] B. Gerull *et al.*, "Mutations of TTN, encoding the giant muscle filament titin, cause familial dilated cardiomyopathy," *Nat. Genet.*, vol. 30, no. 2, pp. 201–204, Feb. 2002, doi: 10.1038/ng815.

[84] K. M. Brauch *et al.*, "Mutations in ribonucleic acid binding protein gene cause familial dilated cardiomyopathy," *J. Am. Coll. Cardiol.*, vol. 54, no. 10, pp. 930–941, Sep. 2009, doi: 10.1016/j.jacc.2009.05.038.

[85] I. A. Sergeeva *et al.*, "Identification of a regulatory domain controlling the Nppa-Nppb gene cluster during heart development and stress," *Dev. Camb. Engl.*, vol. 143, no. 12, pp. 2135–2146, Jun. 2016, doi: 10.1242/dev.132019.

[86] T. Horsthuis *et al.*, "Distinct regulation of developmental and heart disease-induced atrial natriuretic factor expression by two separate distal sequences," *Circ. Res.*, vol. 102, no. 7, pp. 849–859, Apr. 2008, doi: 10.1161/CIRCRESAHA.107.170571.

[87] A. H. Bruggink *et al.*, "Brain natriuretic peptide is produced both by cardiomyocytes and cells infiltrating the heart in patients with severe heart failure supported by a left ventricular assist device," *J. Heart Lung Transplant. Off. Publ. Int. Soc. Heart*

Transplant., vol. 25, no. 2, pp. 174–180, Feb. 2006, doi: 10.1016/j.healun.2005.09.007.

[88] M. B. Coelho, J. Attig, J. Ule, and C. W. J. Smith, "Matrin3: connecting gene expression with the nuclear matrix," *Wiley Interdiscip. Rev. RNA*, vol. 7, no. 3, pp. 303–315, May 2016, doi: 10.1002/wrna.1336.

[89] M. B. Coelho *et al.*, "Nuclear matrix protein Matrin3 regulates alternative splicing and forms overlapping regulatory networks with PTB," *EMBO J.*, vol. 34, no. 5, pp. 653–668, Mar. 2015, doi: 10.15252/embj.201489852.

[90] Y. Uemura *et al.*, "Matrin3 binds directly to intronic pyrimidine-rich sequences and controls alternative splicing," *Genes Cells Devoted Mol. Cell. Mech.*, vol. 22, no. 9, pp. 785–798, Sep. 2017, doi: 10.1111/gtc.12512.

[91] D. Ray *et al.*, "A compendium of RNA-binding motifs for decoding gene regulation," *Nature*, vol. 499, no. 7457, pp. 172–177, Jul. 2013, doi: 10.1038/nature12311.

[92] H. Maatz *et al.*, "RNA-binding protein RBM20 represses splicing to orchestrate cardiac pre-mRNA processing," *J. Clin. Invest.*, vol. 124, no. 8, pp. 3419–3430, Aug. 2014, doi: 10.1172/JCI74523.

[93] R. Beraldi *et al.*, "Rbm20-deficient cardiogenesis reveals early disruption of RNA processing and sarcomere remodeling establishing a developmental etiology for dilated cardiomyopathy," *Hum. Mol. Genet.*, vol. 23, no. 14, pp. 3779–3791, Jul. 2014, doi: 10.1093/hmg/ddu091.

[94] F. Quintero-Rivera *et al.*, "MATR3 disruption in human and mouse associated with bicuspid aortic valve, aortic coarctation and patent ductus arteriosus," *Hum. Mol. Genet.*, vol. 24, no. 8, pp. 2375–2389, Apr. 2015, doi: 10.1093/hmg/ddv004.

[95] W. Guo *et al.*, "Splicing Factor RBM20 Regulates Transcriptional Network of Titin Associated and Calcium Handling Genes in The Heart," *Int. J. Biol. Sci.*, vol. 14, no. 4, pp. 369–380, 2018, doi: 10.7150/ijbs.24117.

[96] S. K. Upadhyay and C. D. Mackereth, "Structural basis of UCUU RNA motif recognition by splicing factor RBM20," *Nucleic Acids Res.*, vol. 48, no. 8, pp. 4538–4550, May 2020, doi: 10.1093/nar/gkaa168.

[97] F. Briganti *et al.*, "iPSC Modeling of RBM20-Deficient DCM Identifies Upregulation of RBM20 as a Therapeutic Strategy," *Cell Rep.*, vol. 32, no. 10, p. 108117, Sep. 2020, doi: 10.1016/j.celrep.2020.108117.

[98] A. Bertero *et al.*, "Dynamics of genome reorganization during human cardiogenesis reveal an RBM20-dependent splicing factory," *Nat. Commun.*, vol. 10, no. 1, p. 1538, Apr. 2019, doi: 10.1038/s41467-019-09483-5.

[99] W. A. Linke and S. Bücker, "King of hearts: a splicing factor rules cardiac proteins," *Nat. Med.*, vol. 18, no. 5, pp. 660–661, May 2012, doi: 10.1038/nm.2762.

[100] M. A. F. Khan *et al.*, "RBM20 Regulates Circular RNA Production From the Titin Gene," *Circ. Res.*, vol. 119, no. 9, pp. 996–1003, Oct. 2016, doi: 10.1161/CIRCRESAHA.116.309568.

[101] D. Lennermann, J. Backs, and M. M. G. van den Hoogenhof, "New Insights in RBM20 Cardiomyopathy," *Curr. Heart Fail. Rep.*, vol. 17, no. 5, pp. 234–246, Oct. 2020, doi: 10.1007/s11897-020-00475-x.

[102] W. Guo, J. M. Pleitner, K. W. Saupe, and M. L. Greaser, "Pathophysiological defects and transcriptional profiling in the RBM20-/- rat model," *PloS One*, vol. 8, no. 12, p. e84281, 2013, doi: 10.1371/journal.pone.0084281.

[103] M. M. G. van den Hoogenhof *et al.*, "RBM20 Mutations Induce an Arrhythmogenic Dilated Cardiomyopathy Related to Disturbed Calcium Handling," *Circulation*, vol. 138, no. 13, pp. 1330–1342, Sep. 2018, doi: 10.1161/CIRCULATIONAHA.117.031947.

[104] D. Li *et al.*, "Identification of novel mutations in RBM20 in patients with dilated cardiomyopathy," *Clin. Transl. Sci.*, vol. 3, no. 3, pp. 90–97, Jun. 2010, doi: 10.1111/j.1752-8062.2010.00198.x.

[105] A. Gaertner, B. Klauke, A. Brodehl, and H. Milting, "RBM20 mutations in left ventricular non-compaction cardiomyopathy," *Pediatr. Investig.*, vol. 4, no. 1, pp. 61–63, Mar. 2020, doi: 10.1002/ped4.12184.

[106] K. Ihara *et al.*, "A missense mutation in the RSRSP stretch of Rbm20 causes dilated cardiomyopathy and atrial fibrillation in mice," *Sci. Rep.*, vol. 10, no. 1, p. 17894, Oct. 2020, doi: 10.1038/s41598-020-74800-8.

[107] P. Belgrader, R. Dey, and R. Berezney, "Molecular cloning of matrin 3. A 125-kilodalton protein of the nuclear matrix contains an extensive acidic domain," *J. Biol. Chem.*, vol. 266, no. 15, pp. 9893–9899, May 1991.

[108] A. Boehringer, K. Garcia-Mansfield, G. Singh, N. Bakkar, P. Pirrotte, and R. Bowser, "ALS Associated Mutations in Matrin 3 Alter Protein-Protein Interactions and Impede mRNA Nuclear Export," *Sci. Rep.*, vol. 7, no. 1, p. 14529, Nov. 2017, doi: 10.1038/s41598-017-14924-6.

[109] C. S. Kao *et al.*, "Selective neuronal degeneration in MATR3 S85C knock-in mouse model of early-stage ALS," *Nat. Commun.*, vol. 11, no. 1, p. 5304, Oct. 2020, doi: 10.1038/s41467-020-18949-w.

[110] P. Przygodzka, J. Boncela, and C. S. Cierniewski, "Matrin 3 as a key regulator of endothelial cell survival," *Exp. Cell Res.*, vol. 317, no. 6, pp. 802–811, Apr. 2011, doi: 10.1016/j.yexcr.2010.12.009.

[111] S. Hisada-Ishii, M. Ebihara, N. Kobayashi, and Y. Kitagawa, "Bipartite nuclear localization signal of matrin 3 is essential for vertebrate cells," *Biochem. Biophys. Res. Commun.*, vol. 354, no. 1, pp. 72–76, Mar. 2007, doi: 10.1016/j.bbrc.2006.12.191.

[112] M. J. Zeitz, K. S. Malyavantham, B. Seifert, and R. Berezney, "Matrin 3: chromosomal distribution and protein interactions," *J. Cell. Biochem.*, vol. 108, no. 1, pp. 125–133, Sep. 2009, doi: 10.1002/jcb.22234.

[113] A. M. Malik, R. A. Miguez, X. Li, Y.-S. Ho, E. L. Feldman, and S. J. Barmada, "Matrin 3-dependent neurotoxicity is modified by nucleic acid binding and nucleocytoplasmic localization," *eLife*, vol. 7, p. e35977, Jul. 2018, doi: 10.7554/eLife.35977.

[114] M. C. G. Iradi *et al.*, "Characterization of gene regulation and protein interaction networks for Matrin 3 encoding mutations linked to amyotrophic lateral sclerosis and myopathy," *Sci. Rep.*, vol. 8, no. 1, p. 4049, Mar. 2018, doi: 10.1038/s41598-018-21371-4.

[115] D. Rajgor, J. G. Hanley, and C. M. Shanahan, "Identification of novel nesprin-1 binding partners and cytoplasmic matrin-3 in processing bodies," *Mol. Biol. Cell*, vol. 27, no. 24, pp. 3894–3902, Dec. 2016, doi: 10.1091/mbc.E16-06-0346.

[116] N. Ramesh, S. Kour, E. N. Anderson, D. Rajasundaram, and U. B. Pandey, "RNA-recognition motif in Matrin-3 mediates neurodegeneration through interaction with hnRNPM," *Acta Neuropathol. Commun.*, vol. 8, no. 1, p. 138, Aug. 2020, doi: 10.1186/s40478-020-01021-5.

[117] M. Salton *et al.*, "Matrin 3 binds and stabilizes mRNA," *PloS One*, vol. 6, no. 8, p. e23882, 2011, doi: 10.1371/journal.pone.0023882.

[118] A. M. Malik and S. J. Barmada, "Matrin 3 in neuromuscular disease: physiology and pathophysiology," *JCI Insight*, vol. 6, no. 1, p. 143948, Jan. 2021, doi: 10.1172/jci.insight.143948.

[119] G. Giordano *et al.*, "Activation of NMDA receptors induces protein kinase A-mediated phosphorylation and degradation of matrin 3. Blocking these effects prevents NMDA-induced neuronal death," *J. Neurochem.*, vol. 94, no. 3, pp. 808–818, Aug. 2005, doi: 10.1111/j.1471-4159.2005.03235.x.

[120] F. F. Depreux *et al.*, "Disruption of the lamin A and matrin-3 interaction by myopathic LMNA mutations," *Hum. Mol. Genet.*, vol. 24, no. 15, pp. 4284–4295, Aug. 2015, doi: 10.1093/hmg/ddv160.

[121] D. Rajgor, C. Gooding, R. Hayward, M. B. Coelho, C. W. Smith, and C. M. Shanahan, "Lamin A/C controls nuclear matrin-3 levels and localization, but not alternative splicing of cassette exons," *bioRxiv*, p. 378240, Jan. 2018, doi: 10.1101/378240.

[122] J. O. Johnson *et al.*, "Mutations in the Matrin 3 gene cause familial amyotrophic lateral sclerosis," *Nat. Neurosci.*, vol. 17, no. 5, pp. 664–666, May 2014, doi: 10.1038/nn.3688.

[123] A. Yamaguchi and K. Takanashi, "FUS interacts with nuclear matrix-associated protein SAFB1 as well as Matrin3 to regulate splicing and ligand-mediated transcription," *Sci. Rep.*, vol. 6, p. 35195, Oct. 2016, doi: 10.1038/srep35195.

[124] M. Neumann *et al.*, "Ubiquitinated TDP-43 in frontotemporal lobar degeneration and amyotrophic lateral sclerosis," *Science*, vol. 314, no. 5796, pp. 130–133, Oct. 2006, doi: 10.1126/science.1134108.

[125] A. Patel *et al.*, "A Liquid-to-Solid Phase Transition of the ALS Protein FUS Accelerated by Disease Mutation," *Cell*, vol. 162, no. 5, pp. 1066–1077, Aug. 2015, doi: 10.1016/j.cell.2015.07.047.

[126] M. Zhao, J. R. Kim, R. van Bruggen, and J. Park, "RNA-Binding Proteins in Amyotrophic Lateral Sclerosis," *Mol. Cells*, vol. 41, no. 9, pp. 818–829, Sep. 2018, doi: 10.14348/molcells.2018.0243.

[127] H. Feit *et al.*, "Vocal cord and pharyngeal weakness with autosomal dominant distal myopathy: clinical description and gene localization to 5q31," *Am. J. Hum. Genet.*, vol. 63, no. 6, pp. 1732–1742, Dec. 1998, doi: 10.1086/302166.

[128] S. Millecamps *et al.*, "Genetic analysis of matrin 3 gene in French amyotrophic lateral sclerosis patients and frontotemporal lobar degeneration with amyotrophic lateral sclerosis patients," *Neurobiol. Aging*, vol. 35, no. 12, p. 2882.e13-2882.e15, Dec. 2014, doi: 10.1016/j.neurobiolaging.2014.07.016.

[129] J. A. Fifita *et al.*, "Mutation analysis of MATR3 in Australian familial amyotrophic lateral sclerosis," *Neurobiol. Aging*, vol. 36, no. 3, p. 1602.e1–2, Mar. 2015, doi: 10.1016/j.neurobiolaging.2014.11.010.

[130] K.-P. Lin *et al.*, "Mutational analysis of MATR3 in Taiwanese patients with amyotrophic lateral sclerosis," *Neurobiol. Aging*, vol. 36, no. 5, p. 2005.e1–4, May 2015, doi: 10.1016/j.neurobiolaging.2015.02.008.

[131] C. S. Leblond *et al.*, "Replication study of MATR3 in familial and sporadic amyotrophic lateral sclerosis," *Neurobiol. Aging*, vol. 37, p. 209.e17-209.e21, Jan. 2016, doi: 10.1016/j.neurobiolaging.2015.09.013.

[132] J. Senderek *et al.*, "Autosomal-dominant distal myopathy associated with a recurrent missense mutation in the gene encoding the nuclear matrix protein, matrin 3," *Am. J. Hum. Genet.*, vol. 84, no. 4, pp. 511–518, Apr. 2009, doi: 10.1016/j.ajhg.2009.03.006.

[133] C. Moloney *et al.*, "Analysis of spinal and muscle pathology in transgenic mice overexpressing wild-type and ALS-linked mutant MATR3," *Acta Neuropathol. Commun.*, vol. 6, no. 1, p. 137, Dec. 2018, doi: 10.1186/s40478-018-0631-0.

[134] X. Zhang *et al.*, "A mutant MATR3 mouse model to explain multisystem proteinopathy," *J. Pathol.*, vol. 249, no. 2, pp. 182–192, Oct. 2019, doi: 10.1002/path.5289.

[135] V. N. Parikh *et al.*, "Regional Variation in RBM20 Causes a Highly Penetrant Arrhythmogenic Cardiomyopathy," *Circ. Heart Fail.*, vol. 12, no. 3, p. e005371, Mar. 2019, doi: 10.1161/CIRCHEARTFAILURE.118.005371.

[136] O. B. Vad *et al.*, "Integration of Scandinavian genetic data with UK biobank data implicates the RBM20 gene with atrial fibrillation pathogenesis," *Eur. Heart J.*, vol. 42, no. Supplement_1, p. ehab724.3319, Oct. 2021, doi: 10.1093/eurheartj/ehab724.3319.

[137] P. A. Koni, S. K. Joshi, U. A. Temann, D. Olson, L. Burkly, and R. A. Flavell, "Conditional vascular cell adhesion molecule 1 deletion in mice: impaired lymphocyte migration to bone marrow," *J. Exp. Med.*, vol. 193, no. 6, pp. 741–754, Mar. 2001, doi: 10.1084/jem.193.6.741.

[138] E. J. Gordon, S. Rao, J. W. Pollard, S. L. Nutt, R. A. Lang, and N. L. Harvey, "Macrophages define dermal lymphatic vessel calibre during development by regulating lymphatic endothelial cell proliferation," *Dev. Camb. Engl.*, vol. 137, no. 22, pp. 3899–3910, Nov. 2010, doi: 10.1242/dev.050021.

[139] A. M. Ochsenbein *et al.*, "Regulation of lymphangiogenesis in the diaphragm by macrophages and VEGFR-3 signaling," *Angiogenesis*, vol. 19, no. 4, pp. 513–524, Oct. 2016, doi: 10.1007/s10456-016-9523-8.

[140] T. Yamazaki *et al.*, "Tissue Myeloid Progenitors Differentiate into Pericytes through TGF-β Signaling in Developing Skin Vasculature," *Cell Rep.*, vol. 18, no. 12, pp. 2991–3004, Mar. 2017, doi: 10.1016/j.celrep.2017.02.069.

[141] R. Breckenridge, S. Kotecha, N. Towers, M. Bennett, and T. Mohun, "Pan-myocardial expression of Cre recombinase throughout mouse development," *Genes. N. Y. N 2000*, vol. 45, no. 3, pp. 135–144, Mar. 2007, doi: 10.1002/dvg.20275.

[142] J. C. Brüning *et al.*, "A muscle-specific insulin receptor knockout exhibits features of the metabolic syndrome of NIDDM without altering glucose tolerance," *Mol. Cell*, vol. 2, no. 5, pp. 559–569, Nov. 1998, doi: 10.1016/s1097-2765(00)80155-0.

[143] Y. Yamashita *et al.*, "LDB3 splicing abnormalities are specific to skeletal muscles of patients with myotonic dystrophy type 1 and alter its PKC binding affinity," *Neurobiol. Dis.*, vol. 69, pp. 200–205, Sep. 2014, doi: 10.1016/j.nbd.2014.05.026.

[144] T. Yamamoto, A. Miura, K. Itoh, Y. Takeshima, and H. Nishio, "RNA sequencing reveals abnormal LDB3 splicing in sudden cardiac death," *Forensic Sci. Int.*, vol. 302, p. 109906, 2019, doi: https://doi.org/10.1016/j.forsciint.2019.109906.

[145] M. Zheng *et al.*, "Cardiac-specific ablation of Cypher leads to a severe form of dilated cardiomyopathy with premature death," *Hum. Mol. Genet.*, vol. 18, no. 4, pp. 701–713, Feb. 2009, doi: 10.1093/hmg/ddn400.

[146] A. M. Wobus, G. Wallukat, and J. Hescheler, "Pluripotent mouse embryonic stem cells are able to differentiate into cardiomyocytes expressing chronotropic responses to adrenergic and cholinergic agents and Ca2+ channel blockers," *Differ. Res. Biol. Divers.*, vol. 48, no. 3, pp. 173–182, Dec. 1991, doi: 10.1111/j.1432-0436.1991.tb00255.x.

[147] M. J. Seewald *et al.*, "Genomic profiling of developing cardiomyocytes from recombinant murine embryonic stem cells reveals regulation of transcription factor clusters," *Physiol. Genomics*, vol. 38, no. 1, pp. 7–15, Jun. 2009, doi: 10.1152/physiolgenomics.90287.2008.

[148] W. C. Claycomb *et al.*, "HL-1 cells: a cardiac muscle cell line that contracts and retains phenotypic characteristics of the adult cardiomyocyte," *Proc. Natl. Acad. Sci. U. S. A.*, vol. 95, no. 6, pp. 2979–2984, Mar. 1998, doi: 10.1073/pnas.95.6.2979.

[149] N. Chaudary, Z. Naydenova, I. Shuralyova, and I. R. Coe, "Hypoxia regulates the adenosine transporter, mENT1, in the murine cardiomyocyte cell line, HL-1," *Cardiovasc. Res.*, vol. 61, no. 4, pp. 780–788, Mar. 2004, doi: 10.1016/j.cardiores.2003.11.031.

[150] M. Nobles, S. Sebastian, and A. Tinker, "HL-1 cells express an inwardly rectifying K+ current activated via muscarinic receptors comparable to that in mouse atrial myocytes," *Pflugers Arch.*, vol. 460, no. 1, pp. 99–108, Jun. 2010, doi: 10.1007/s00424-010-0799-z.

[151] B. Zinshteyn and K. Nishikura, "Adenosine-to-inosine RNA editing," *Wiley Interdiscip. Rev. Syst. Biol. Med.*, vol. 1, no. 2, pp. 202–209, Oct. 2009, doi: 10.1002/wsbm.10.

[152] K. T. Furukawa, K. Yamashita, N. Sakurai, and S. Ohno, "The Epithelial Circumferential Actin Belt Regulates YAP/TAZ through Nucleocytoplasmic Shuttling of Merlin," *Cell Rep.*, vol. 20, no. 6, pp. 1435–1447, Aug. 2017, doi: 10.1016/j.celrep.2017.07.032.

[153] A. D. Rouillard *et al.*, "The harmonizome: a collection of processed datasets gathered to serve and mine knowledge about genes and proteins," *Database J. Biol. Databases Curation*, vol. 2016, p. baw100, 2016, doi: 10.1093/database/baw100.

[154] B. C. Heng *et al.*, "Role of YAP/TAZ in Cell Lineage Fate Determination and Related Signaling Pathways," *Front. Cell Dev. Biol.*, vol. 8, p. 735, 2020, doi: 10.3389/fcell.2020.00735.

[155] T. J. Müller *et al.*, "Phenotype of matrin-3-related distal myopathy in 16 German patients," *Ann. Neurol.*, vol. 76, no. 5, pp. 669–680, Nov. 2014, doi: 10.1002/ana.24255.

[156] F. Wittchen *et al.*, "Genomic expression profiling of human inflammatory cardiomyopathy (DCMi) suggests novel therapeutic targets," *J. Mol. Med. Berl. Ger.*, vol. 85, no. 3, pp. 257–271, Mar. 2007, doi: 10.1007/s00109-006-0122-9.

[157] J. P. Konhilas, A. H. Maass, S. W. Luckey, B. L. Stauffer, E. N. Olson, and L. A. Leinwand, "Sex modifies exercise and cardiac adaptation in mice," *Am. J. Physiol. Heart Circ. Physiol.*, vol. 287, no. 6, pp. H2768-2776, Dec. 2004, doi: 10.1152/ajpheart.00292.2004.

[158] M. Jelinek, C. Wallach, H. Ehmke, and A. P. Schwoerer, "Genetic background dominates the susceptibility to ventricular arrhythmias in a murine model of β-adrenergic stimulation," *Sci. Rep.*, vol. 8, no. 1, p. 2312, Feb. 2018, doi: 10.1038/s41598-018-20792-5.

[159] S. W. M. van den Borne *et al.*, "Mouse strain determines the outcome of wound healing after myocardial infarction," *Cardiovasc. Res.*, vol. 84, no. 2, pp. 273–282, Nov. 2009, doi: 10.1093/cvr/cvp207.

[160] T. Anzai, T. Yamagata, and H. Uosaki, "Comparative Transcriptome Landscape of Mouse and Human Hearts," *Front. Cell Dev. Biol.*, vol. 8, p. 268, 2020, doi: 10.3389/fcell.2020.00268.

[161] P. A. Doevendans, M. J. Daemen, E. D. de Muinck, and J. F. Smits, "Cardiovascular phenotyping in mice," *Cardiovasc. Res.*, vol. 39, no. 1, pp. 34–49, Jul. 1998, doi: 10.1016/s0008-6363(98)00073-x.

[162] R. L. Hamlin and R. A. Altschuld, "Extrapolation from mouse to man," *Circ. Cardiovasc. Imaging*, vol. 4, no. 1, pp. 2–4, Jan. 2011, doi: 10.1161/CIRCIMAGING.110.961979.

[163] L. Wong *et al.*, "Comparison of human and rodent cell models to study myocardial lipid-induced insulin resistance," *Prostaglandins Leukot. Essent. Fatty Acids*, vol. 167, p. 102267, Apr. 2021, doi: 10.1016/j.plefa.2021.102267.

[164] F. Hinze, C. Dieterich, M. H. Radke, H. Granzier, and M. Gotthardt, "Reducing RBM20 activity improves diastolic dysfunction and cardiac atrophy," *J. Mol. Med. Berl. Ger.*, vol. 94, no. 12, pp. 1349–1358, Dec. 2016, doi: 10.1007/s00109-016-1483-3.

[165] S. Gerstberger, M. Hafner, M. Ascano, and T. Tuschl, "Evolutionary Conservation and Expression of Human RNA-Binding Proteins and Their Role in Human Genetic Disease," *Adv. Exp. Med. Biol.*, vol. 825, pp. 1–55, 2014, doi: 10.1007/978-1-4939-1221-6_1.

[166] J. Ye *et al.*, "hnRNP U protein is required for normal pre-mRNA splicing and postnatal heart development and function," *Proc. Natl. Acad. Sci. U. S. A.*, vol. 112, no. 23, pp. E3020-3029, Jun. 2015, doi: 10.1073/pnas.1508461112.

[167] G. Diss, D. Ascencio, A. DeLuna, and C. R. Landry, "Molecular mechanisms of paralogous compensation and the robustness of cellular networks," *J. Exp. Zoolog. B Mol. Dev. Evol.*, vol. 322, no. 7, pp. 488–499, Nov. 2014, doi: 10.1002/jez.b.22555.

[168] M. A. El-Brolosy and D. Y. R. Stainier, "Genetic compensation: A phenomenon in search of mechanisms," *PLoS Genet.*, vol. 13, no. 7, p. e1006780, Jul. 2017, doi: 10.1371/journal.pgen.1006780.

[169] A. Luzuriaga-Neira, K. Subramanian, and D. Alvarez-Ponce, "Functional compensation of mouse duplicates by their paralogs expressed in the same tissues," *Genome Biol. Evol.*, p. evac126, Aug. 2022, doi: 10.1093/gbe/evac126.

[170] C. Zhu *et al.*, "Single-molecule, full-length transcript isoform sequencing reveals disease-associated RNA isoforms in cardiomyocytes," *Nat. Commun.*, vol. 12, no. 1, p. 4203, Jul. 2021, doi: 10.1038/s41467-021-24484-z.

[171] D. Skowronska-Krawczyk *et al.*, "Required enhancer–matrin-3 network interactions for a homeodomain transcription program," *Nature*, vol. 514, no. 7521, pp. 257–261, Oct. 2014, doi: 10.1038/nature13573.

[172] D. Pollini *et al.*, "Multilayer and MATR3-dependent regulation of mRNAs maintains pluripotency in human induced pluripotent stem cells," *iScience*, vol. 24, no. 3, p. 102197, Mar. 2021, doi: 10.1016/j.isci.2021.102197.

[173] P. J. Skene and S. Henikoff, "An efficient targeted nuclease strategy for high-resolution mapping of DNA binding sites," *eLife*, vol. 6, p. e21856, Jan. 2017, doi: 10.7554/eLife.21856.

[174] C. J. Weeland, M. M. van den Hoogenhof, A. Beqqali, and E. E. Creemers, "Insights into alternative splicing of sarcomeric genes in the heart," *J. Mol. Cell. Cardiol.*, vol. 81, pp. 107–113, Apr. 2015, doi: 10.1016/j.yjmcc.2015.02.008.

[175] J.-N. Boeckel *et al.*, "SLM2 Is A Novel Cardiac Splicing Factor Involved in Heart Failure due to Dilated Cardiomyopathy," *Genomics Proteomics Bioinformatics*, pp. S1672-0229(21)00146–7, Jul. 2021, doi: 10.1016/j.gpb.2021.01.006.

[176] M. H. Radke *et al.*, "Targeted deletion of titin N2B region leads to diastolic dysfunction and cardiac atrophy," *Proc. Natl. Acad. Sci. U. S. A.*, vol. 104, no. 9, pp. 3444–3449, Feb. 2007, doi: 10.1073/pnas.0608543104.

[177] H. L. Granzier *et al.*, "Truncation of titin's elastic PEVK region leads to cardiomyopathy with diastolic dysfunction," *Circ. Res.*, vol. 105, no. 6, pp. 557–564, Sep. 2009, doi: 10.1161/CIRCRESAHA.109.200964.

[178] C. Tharp, L. Mestroni, and M. Taylor, "Modifications of Titin Contribute to the Progression of Cardiomyopathy and Represent a Therapeutic Target for Treatment of Heart Failure," *J. Clin. Med.*, vol. 9, no. 9, p. E2770, Aug. 2020, doi: 10.3390/jcm9092770.

[179] Q. Zhou *et al.*, "Ablation of Cypher, a PDZ-LIM domain Z-line protein, causes a severe form of congenital myopathy," *J. Cell Biol.*, vol. 155, no. 4, pp. 605–612, Nov. 2001, doi: 10.1083/jcb.200107092.

[180] "Cardiac-specific ablation of Cypher leads to a severe form of dilated cardiomyopathy with premature death - PubMed." https://pubmed.ncbi.nlm.nih.gov/19028670/ (accessed May 03, 2022).

[181] T. Arimura *et al.*, "Impaired binding of ZASP/Cypher with phosphoglucomutase 1 is associated with dilated cardiomyopathy," *Cardiovasc. Res.*, vol. 83, no. 1, pp. 80–88, Jul. 2009, doi: 10.1093/cvr/cvp119.

[182] E. D. Luczak *et al.*, "Mitochondrial CaMKII causes adverse metabolic reprogramming and dilated cardiomyopathy," *Nat. Commun.*, vol. 11, no. 1, Art. no. 1, Sep. 2020, doi: 10.1038/s41467-020-18165-6.

[183] T. Zhang *et al.*, "The δC Isoform of CaMKII Is Activated in Cardiac Hypertrophy and Induces Dilated Cardiomyopathy and Heart Failure," *Circ. Res.*, vol. 92, no. 8, pp. 912–919, May 2003, doi: 10.1161/01.RES.0000069686.31472.C5.

[184] C. A. Valencia, W. Ju, and R. Liu, "Matrin 3 is a Ca2+/calmodulin-binding protein cleaved by caspases," *Biochem. Biophys. Res. Commun.*, vol. 361, no. 2, pp. 281–286, Sep. 2007, doi: 10.1016/j.bbrc.2007.06.156.

[185] M. Herwig *et al.*, "Modulation of Titin-Based Stiffness in Hypertrophic Cardiomyopathy via Protein Kinase D," *Front. Physiol.*, vol. 11, 2020, [Online]. Available: https://www.frontiersin.org/article/10.3389/fphys.2020.00240

[186] N. Hamdani *et al.*, "Crucial role for Ca2(+)/calmodulin-dependent protein kinase-II in regulating diastolic stress of normal and failing hearts via titin phosphorylation," *Circ. Res.*, vol. 112, no. 4, pp. 664–674, Feb. 2013, doi: 10.1161/CIRCRESAHA.111.300105.

[187] "Gigantic business: titin properties and function through thick and thin - PubMed." https://pubmed.ncbi.nlm.nih.gov/24625729/ (accessed May 03, 2022).

[188] E. M. Smigielski, K. Sirotkin, M. Ward, and S. T. Sherry, "dbSNP: a database of single nucleotide polymorphisms," *Nucleic Acids Res.*, vol. 28, no. 1, pp. 352–355, Jan. 2000.

[189] E. Reuveni, V. E. Ramensky, and C. Gross, "Mouse SNP Miner: an annotated database of mouse functional single nucleotide polymorphisms," *BMC Genomics*, vol. 8, p. 24, Jan. 2007, doi: 10.1186/1471-2164-8-24.

[190] G. Quinones-Valdez *et al.*, "Regulation of RNA editing by RNA-binding proteins in human cells," *Commun. Biol.*, vol. 2, p. 19, 2019, doi: 10.1038/s42003-018-0271-8.

[191] K. Ahn, S. Pan, K. Beningo, and D. Hupe, "A permanent human cell line (EA.hy926) preserves the characteristics of endothelin converting enzyme from primary human umbilical vein endothelial cells," *Life Sci.*, vol. 56, no. 26, pp. 2331–2341, 1995, doi: 10.1016/0024-3205(95)00227-w.

[192] D. Wang, Z. Chen, A. Wai Kan Yeung, and A. G. Atanasov, "Differences between common endothelial cell models (primary human aortic endothelial cells and EA.hy926 cells) revealed through transcriptomics, bioinformatics, and functional analysis," *Curr. Res. Biotechnol.*, vol. 3, pp. 135–145, Jan. 2021, doi: 10.1016/j.crbiot.2021.05.001.

[193] K. Suzuki-Inoue *et al.*, "Essential in vivo roles of the C-type lectin receptor CLEC-2: embryonic/neonatal lethality of CLEC-2-deficient mice by blood/lymphatic misconnections and impaired thrombus formation of CLEC-2-deficient platelets," *J. Biol. Chem.*, vol. 285, no. 32, pp. 24494–24507, Aug. 2010, doi: 10.1074/jbc.M110.130575.

[194] R. K. Jain, L. L. Munn, and D. Fukumura, "Lymphangiography of the mouse ear," *Cold Spring Harb. Protoc.*, vol. 2012, no. 11, pp. 1179–1180, Nov. 2012, doi: 10.1101/pdb.prot072116.

[195] T. N. Sato, Y. Qin, C. A. Kozak, and K. L. Audus, "Tie-1 and tie-2 define another class of putative receptor tyrosine kinase genes expressed in early embryonic vascular system," *Proc. Natl. Acad. Sci. U. S. A.*, vol. 90, no. 20, pp. 9355–9358, Oct. 1993, doi: 10.1073/pnas.90.20.9355.

[196] N. Takakura *et al.*, "Critical role of the TIE2 endothelial cell receptor in the development of definitive hematopoiesis," *Immunity*, vol. 9, no. 5, pp. 677–686, Nov. 1998, doi: 10.1016/s1074-7613(00)80665-2.

[197] I. Hamaguchi *et al.*, "Loss of Tie2 receptor compromises embryonic stem cell-derived endothelial but not hematopoietic cell survival," *Blood*, vol. 107, no. 3, pp. 1207–1213, Feb. 2006, doi: 10.1182/blood-2005-05-1823.

[198] T. Morisada *et al.*, "Angiopoietin-1 promotes LYVE-1-positive lymphatic vessel formation," *Blood*, vol. 105, no. 12, pp. 4649–4656, Jun. 2005, doi: 10.1182/blood-2004-08-3382.

[199] R. S. Srinivasan *et al.*, "Lineage tracing demonstrates the venous origin of the mammalian lymphatic vasculature," *Genes Dev.*, vol. 21, no. 19, pp. 2422–2432, Oct. 2007, doi: 10.1101/gad.1588407.

[200] C. Pichol-Thievend *et al.*, "A blood capillary plexus-derived population of progenitor cells contributes to genesis of the dermal lymphatic vasculature during embryonic development," *Dev. Camb. Engl.*, vol. 145, no. 10, p. dev160184, May 2018, doi: 10.1242/dev.160184.

[201] M. T. Dellinger, S. M. Meadows, K. Wynne, O. Cleaver, and R. A. Brekken, "Vascular endothelial growth factor receptor-2 promotes the development of the lymphatic vasculature," *PloS One*, vol. 8, no. 9, p. e74686, 2013, doi: 10.1371/journal.pone.0074686.

[202] B. E. Clausen, C. Burkhardt, W. Reith, R. Renkawitz, and I. Förster, "Conditional gene targeting in macrophages and granulocytes using LysMcre mice," *Transgenic Res.*, vol. 8, no. 4, pp. 265–277, Aug. 1999, doi: 10.1023/a:1008942828960.

[203] S. Bangru *et al.*, "Alternative splicing rewires Hippo signaling pathway in hepatocytes to promote liver regeneration," *Nat. Struct. Mol. Biol.*, vol. 25, no. 10, pp. 928–939, Oct. 2018, doi: 10.1038/s41594-018-0129-2.

[204] A. Pocaterra, P. Romani, and S. Dupont, "YAP/TAZ functions and their regulation at a glance," *J. Cell Sci.*, vol. 133, no. 2, p. jcs230425, Jan. 2020, doi: 10.1242/jcs.230425.

[205] M. Bentsen *et al.*, "ATAC-seq footprinting unravels kinetics of transcription factor binding during zygotic genome activation," *Nat. Commun.*, vol. 11, no. 1, p. 4267, Aug. 2020, doi: 10.1038/s41467-020-18035-1.

[206] I. Yevshin, R. Sharipov, T. Valeev, A. Kel, and F. Kolpakov, "GTRD: a database of transcription factor binding sites identified by ChIP-seq experiments," *Nucleic Acids Res.*, vol. 45, no. Database issue, pp. D61–D67, Jan. 2017, doi: 10.1093/nar/gkw951.

[207] H. Cai *et al.*, "Angiotensin II Influences Pre-mRNA Splicing Regulation by Enhancing RBM20 Transcription Through Activation of the MAPK/ELK1 Signaling Pathway," *Int. J. Mol. Sci.*, vol. 20, no. 20, p. E5059, Oct. 2019, doi: 10.3390/ijms20205059.

[208] C. Zhu, Z. Yin, J. Ren, R. J. McCormick, S. P. Ford, and W. Guo, "RBM20 is an essential factor for thyroid hormone-regulated titin isoform transition," *J. Mol. Cell Biol.*, vol. 7, no. 1, pp. 88–90, Feb. 2015, doi: 10.1093/jmcb/mjv002.

[209] M. M. Keshwani *et al.*, "Conserved proline-directed phosphorylation regulates SR protein conformation and splicing function," *Biochem. J.*, vol. 466, no. 2, pp. 311–322, Mar. 2015, doi: 10.1042/BJ20141373.

[210] M. Gigli *et al.*, "A Review of the Giant Protein Titin in Clinical Molecular Diagnostics of Cardiomyopathies," *Front. Cardiovasc. Med.*, vol. 3, 2016, [Online]. Available: https://www.frontiersin.org/article/10.3389/fcvm.2016.00021

[211] E. Zaklyazminskaya *et al.*, "Low mutation rate in the TTN gene in paediatric patients with dilated cardiomyopathy – a pilot study," *Sci. Rep.*, vol. 9, no. 1, p. 16409, Nov. 2019, doi: 10.1038/s41598-019-52911-1.

[212] K. M. Brauch *et al.*, "Mutations in RNA Binding Protein Gene Cause Familial Dilated Cardiomyopathy," *J. Am. Coll. Cardiol.*, vol. 54, no. 10, pp. 930–941, Sep. 2009, doi: 10.1016/j.jacc.2009.05.038.

[213] E. Kayvanpour *et al.*, "Genotype-phenotype associations in dilated cardiomyopathy: meta-analysis on more than 8000 individuals," *Clin. Res. Cardiol.*, vol. 106, no. 2, pp. 127–139, Feb. 2017, doi: 10.1007/s00392-016-1033-6.

[214] R. E. Ferrell, M. A. Kimak, E. C. Lawrence, and D. N. Finegold, "Candidate gene analysis in primary lymphedema," *Lymphat. Res. Biol.*, vol. 6, no. 2, pp. 69–76, 2008, doi: 10.1089/lrb.2007.1022.

[215] S. Michelini *et al.*, "Clinical and genetic study of 46 Italian patients with primary lymphedema," *Lymphology*, vol. 45, no. 1, pp. 3–12, Mar. 2012.

[216] S. Paolacci, Y. Rakhmanov, P. Maltese, A. Zulian, S. Michelini, and M. Bertelli, "Genetic testing for lymphatic malformations with or without primary lymphedema," *EuroBiotech J.*, vol. 2, pp. 5–9, Sep. 2018, doi: 10.2478/ebtj-2018-0024.

[217] M. Ricci *et al.*, "Two rare PROX1 variants in patients with lymphedema," *Mol. Genet. Genomic Med.*, vol. 8, no. 10, p. e1424, Oct. 2020, doi: 10.1002/mgg3.1424.

[218] A. Ghalamkarpour *et al.*, "Sporadic in utero generalized edema caused by mutations in the lymphangiogenic genes VEGFR3 and FOXC2," *J. Pediatr.*, vol. 155, no. 1, pp. 90–93, Jul. 2009, doi: 10.1016/j.jpeds.2009.02.023.

[219] F. Schwenk, U. Baron, and K. Rajewsky, "A cre-transgenic mouse strain for the ubiquitous deletion of loxP-flanked gene segments including deletion in germ cells," *Nucleic Acids Res.*, vol. 23, no. 24, pp. 5080–5081, Dec. 1995, doi: 10.1093/nar/23.24.5080.

[220] C. I. Rodríguez *et al.*, "High-efficiency deleter mice show that FLPe is an alternative to Cre-loxP," *Nat. Genet.*, vol. 25, no. 2, pp. 139–140, Jun. 2000, doi: 10.1038/75973.

[221] T. H. M. Pham *et al.*, "Lymphatic endothelial cell sphingosine kinase activity is required for lymphocyte egress and lymphatic patterning," *J. Exp. Med.*, vol. 207, no. 1, pp. 17–27, Jan. 2010, doi: 10.1084/jem.20091619.

[222] P. Soriano, "Generalized lacZ expression with the ROSA26 Cre reporter strain," *Nat. Genet.*, vol. 21, no. 1, pp. 70–71, Jan. 1999, doi: 10.1038/5007.

[223] J. Besser *et al.*, "MiRNA-1/133a clusters regulate adrenergic control of cardiac repolarization," *PloS One*, vol. 9, no. 11, p. e113449, 2014, doi: 10.1371/journal.pone.0113449.

[224] T. D. O'Connell, M. C. Rodrigo, and P. C. Simpson, "Isolation and culture of adult mouse cardiac myocytes," *Methods Mol. Biol. Clifton NJ*, vol. 357, pp. 271–296, 2007, doi: 10.1385/1-59745-214-9:271.

[225] "Babraham Bioinformatics - FastQC A Quality Control tool for High Throughput Sequence Data." https://www.bioinformatics.babraham.ac.uk/projects/fastqc/ (accessed Aug. 06, 2021).

[226] A. M. Bolger, M. Lohse, and B. Usadel, "Trimmomatic: a flexible trimmer for Illumina sequence data," *Bioinforma. Oxf. Engl.*, vol. 30, no. 15, pp. 2114–2120, Aug. 2014, doi: 10.1093/bioinformatics/btu170.

[227] A. Dobin *et al.*, "STAR: ultrafast universal RNA-seq aligner," *Bioinforma. Oxf. Engl.*, vol. 29, no. 1, pp. 15–21, Jan. 2013, doi: 10.1093/bioinformatics/bts635.

[228] Y. Liao, G. K. Smyth, and W. Shi, "featureCounts: an efficient general purpose program for assigning sequence reads to genomic features," *Bioinforma. Oxf. Engl.*, vol. 30, no. 7, pp. 923–930, Apr. 2014, doi: 10.1093/bioinformatics/btt656.

[229] M. I. Love, W. Huber, and S. Anders, "Moderated estimation of fold change and dispersion for RNA-seq data with DESeq2," *Genome Biol.*, vol. 15, no. 12, p. 550, 2014, doi: 10.1186/s13059-014-0550-8.

[230] UniProt Consortium, "UniProt: a worldwide hub of protein knowledge," *Nucleic Acids Res.*, vol. 47, no. D1, pp. D506–D515, Jan. 2019, doi: 10.1093/nar/gky1049.

[231] S. W. Hartley and J. C. Mullikin, "Detection and visualization of differential splicing in RNA-Seq data with JunctionSeq," *Nucleic Acids Res.*, vol. 44, no. 15, p. e127, Sep. 2016, doi: 10.1093/nar/gkw501.

[232] M. Ashburner *et al.*, "Gene ontology: tool for the unification of biology. The Gene Ontology Consortium," *Nat. Genet.*, vol. 25, no. 1, pp. 25–29, May 2000, doi: 10.1038/75556.

[233] Gene Ontology Consortium, "The Gene Ontology resource: enriching a GOld mine," *Nucleic Acids Res.*, vol. 49, no. D1, pp. D325–D334, Jan. 2021, doi: 10.1093/nar/gkaa1113.

[234] "R: a language and environment for statistical computing." https://www.gbif.org/tool/81287/r-a-language-and-environment-for-statistical-computing (accessed Aug. 06, 2021).

[235] M. Piechotta, E. Wyler, U. Ohler, M. Landthaler, and C. Dieterich, "JACUSA: site-specific identification of RNA editing events from replicate sequencing data," *BMC Bioinformatics*, vol. 18, no. 1, p. 7, Jan. 2017, doi: 10.1186/s12859-016-1432-8.

[236] "Venny 2.1.0." https://bioinfogp.cnb.csic.es/tools/venny/ (accessed Aug. 06, 2021).

[237] C. M. Warren, P. R. Krzesinski, and M. L. Greaser, "Vertical agarose gel electrophoresis and electroblotting of high-molecular-weight proteins," *Electrophoresis*, vol. 24, no. 11, pp. 1695–1702, Jun. 2003, doi: 10.1002/elps.200305392.

[238] T. Yamazaki *et al.*, "Whole-Mount Adult Ear Skin Imaging Reveals Defective Neuro-Vascular Branching Morphogenesis in Obese and Type 2 Diabetic Mouse Models," *Sci. Rep.*, vol. 8, no. 1, p. 430, Jan. 2018, doi: 10.1038/s41598-017-18581-7.

[239] J. T. Robinson *et al.*, "Integrative genomics viewer," *Nat. Biotechnol.*, vol. 29, no. 1, pp. 24–26, Jan. 2011, doi: 10.1038/nbt.1754.

[240] H. Schultheis *et al.*, "WIlsON: Web-based Interactive Omics VisualizatioN," *Bioinforma. Oxf. Engl.*, vol. 35, no. 6, pp. 1055–1057, Mar. 2019, doi: 10.1093/bioinformatics/bty711.

[241] "SMART - Servier Medical ART." https://smart.servier.com/ (accessed Aug. 06, 2021).

Amendment

I, Silke Kreher, used the term "we" as a stylistic device in my doctoral thesis. However, I would like to make it clear that I was supported in individual experiments and analyses by service groups and collaboration partners, all experts in their fields. These contributions are already mentioned in the material methods section of my doctoral thesis and are again listed below:

My direct supervisor Dr. Andre Schneider (MPI-HLR, Bad Nauheim, Germany) shared his expertise in generating mouse lines. ESC cell culture and transgenic service were performed by Sonja Krüger and Susanne Kreutzer (MPI-HLR, Bad Nauheim, Germany). The animal caretakers of the MPI-HLR, Bad Nauheim, Germany, did most of the routine work with the mice. Cardiac bodies were kindly provided by Sonja Krüger. Dr. Shuichi Watanabe (MPI-HLR, Bad Nauheim, Germany) shared a breeding pair of this YAP5SA-V5 mouse line. Human myocardial biopsies were kindly provided by Dr. Manfred Richter (Kerckhoff-Klinik, Bad Nauheim, Germany). MRI imaging was performed by Dr. Astrid Wietelmann, Scientific Service Group for MRI and µCT of the MPI Bad Nauheim. TEM sample preparation and imaging were performed by Janett Piesker, Scientific Service Group Microscopy of the MPI-Bad Nauheim. Juvenile and adult cardiomyocytes were isolated by my esteemed colleague Marion Wiesnet (MPI-HLR, Bad Nauheim, Germany).

Transcriptome sequencing of multiple experiments was performed in the Deep Sequencing Platform led by Dr. Stefan Günther (MPI-HLR, Bad Nauheim, Germany). Dr. Günther also run the bioinformatic analysis for general transcriptomics. MAJIQ and Voila bioinformatic data analysis was developed in the course of a close cooperation between me and Dominik Stroh and Dr. Kathi Zarnack (BMLS, Frankfurt, Germany). JACUSA-based bioinformatic data analysis was processed by Prof. Dr. Christoph Dieterich (Klaus Tschira Institute for Integrative Computational Cardiology Department of Internal Medicine III, University Hospital Heidelberg, Germany). Titin gels were carried out in Berlin in collaboration with the experts Dr. Michael Radke and Prof. Dr. Michael Gotthardt (Max Delbrück Center for Molecular Medicine in the Helmholtz Association, Berlin, Germany).

In this context, I would like to thank everyone again who was part of this great project.

Bad Nauheim, 23.01.2023

Silke Kreher